PhotoniX

REVIEW Open Access

Extreme-depth water-related optical imaging: conquering ultra-low illumination environments from epipelagic zone to Mariana Trench

Zhe Sun[1,2], Tong Tian[3,4], Haofeng Hu[5], Yan He[6], Mingjia Shangguan[7,8], Tao Yu[9], Qingsong Yang[10,11], Mingliang Chen[6], Xinwei Wang[12], Yifan Chen[1,2], Kanzhong Yao[2], Ye Zheng[2], Ye Qian[10,11], Mingyu Dou[9], Jinghan Xu[7], Qiang Li[13], Guojun Wu[9,14] and Xuelong Li[2*]

*Correspondence:
xuelong_li@ieee.org

[2] Institute of Artificial Intelligence (TeleAI), China Telecom, Shanghai 200232, People's Republic of China
Full list of author information is available at the end of the article

Abstract

Exploring the ocean's vast, water-related environment, covering over 70% of Earth's surface, remains a formidable challenge due to photon starvation, high-pressure extremes, and complex light-scattering effects below the photic zone. Optical imaging technologies have emerged as transformative tools for full ocean depth exploration, overcoming limitations of traditional acoustic methods through high-resolution, spectrally rich, and temporally precise observations. This review systematically surveys the physical principles, engineering constraints, and state-of-the-art developments in optical imaging from surface waters to the Mariana Trench. We analyze the role of blue-green pulsed lasers in improving imaging quality. We highlight key factors affecting light propagation in seawater. Advanced imaging modalities such as polarized imaging, range-gated imaging, single-photon imaging, streak camera techniques, and ghost imaging (GI) are examined for their capabilities to enhance visibility, resolution, and resilience in turbid, light-limited conditions. Furthermore, we introduce the progress achieved by deep-sea submersibles and their high-performance camera payloads is highlighted, alongside the burgeoning integration of artificial-intelligence-driven image enhancement and restoration frameworks. Collectively, these interdisciplinary innovations chart a new path for unlocking deep-sea frontiers, enabling ecological monitoring, resource mapping, and autonomous guidance in earth's most inaccessible water-related realms.

Keywords: Optical imaging, Water-related imaging, Imaging technology, Image processing

Introduction

Water-related environments span a diverse range of natural systems, including clouds, rain, fog, snow, rivers, lakes, and oceans. Among these, the ocean stands as Earth's largest and most consequential water-related domain, covering approximately 71% of the planet's surface and containing 97% of its water [1, 2]. Vertical stratification divides the

Springer

ocean into the photic zone (0 to 200 m), where sunlight enables photosynthesis, the mesopelagic or "twilight" zone (200 to 1,000 m) characterized by diminishing light, and the abyssopelagic and hadal zones (> 6,000 m) [3], including trenches like the Mariana Trench at depths near 11,000 m [4, 5]. Ocean biodiversity underpins complex trophic networks, supporting fisheries, nutrient cycling, and essential ecosystem services. Moreover, the deep-sea harbors significant untapped resources, hydrocarbon energy reserves, polymetallic nodules rich in rare minerals, and marine natural products with promising bioactive and pharmaceutical properties. Marine exploration has historically catalyzed major scientific discoveries, from elucidating plate tectonics to identifying extremophiles in hydrothermal vent ecosystems, while also underpinning critical economic sectors such as fisheries, maritime trade, and energy infrastructure. However, despite its global significance, over 95% of the ocean's volume remains unexplored, constituting a "scientific terra incognita" due to extreme pressures, ultra-low illumination darkness, and light-attenuation caused by absorption and scattering [6]. Substantial knowledge gaps persist, particularly regarding deep-sea biodiversity, benthic ecosystem dynamics, and the impacts of climate change and anthropogenic activities such as deep-sea mining. Addressing these challenges necessitates transformative technologies capable of probing ultra-low illumination environments while ensuring sustainable stewardship of marine ecosystems [7, 8].

Optical imaging has emerged as a paradigm-shifting approach for deep-sea exploration, overcoming limitations inherent to traditional acoustic methods like sonar. While sonar excels in long-range bathymetry, its spatial resolution constraints and inability to resolve fine visual or spectral details hinder biological and geological analyses [9, 10]. In contrast, optical systems enable high-resolution visualization, real-time spectral characterization, and dynamic process monitoring across marine environments. In addition, unlike terrestrial imaging, photons propagating through seawater encounter a combination of coupled degradations. First, wavelength-selective attenuation rapidly diminishes the red spectrum, with more than 90% of red light absorbed within the first 5 m, leaving only a narrow blue-green transmission window ($\approx$ 450 to 550 nm) and causing pronounced color-channel imbalance. Second, suspended particulates induce strong backscattering, which severely reduces scene contrast and often saturates imaging sensors; this effect intensifies nonlinearly with both turbidity and imaging distance. Third, the rapid attenuation of natural light with depth gives rise to highly nonuniform illumination, manifested as surface caustics, volumetric shadows, and refractive distortions, thereby violating the Lambertian assumptions underlying most conventional vision algorithms. As shown in Fig. 1, modern methodologies span shallow to full ocean depth (FOD) applications: airborne and shipborne LiDAR exploit blue-green lasers for coastal bathymetry; polarization imaging suppresses scattering artifacts; and structured-light systems paired with computational algorithms enhance 3D reconstruction in turbid waters [11, 12]. Furthermore, submersible-mounted optical systems, such as those deployed on China's Fendouzhe (capable of reaching 11,000 m), are bridging the observational gap between surface and abyssal ecosystems, thereby advancing resource mapping, habitat assessment, and hydrodynamic research.

Nevertheless, water-related optical imaging confronts three fundamental constraints: wavelength-dependent absorption, scattering, and high-pressure extremes. Water strongly

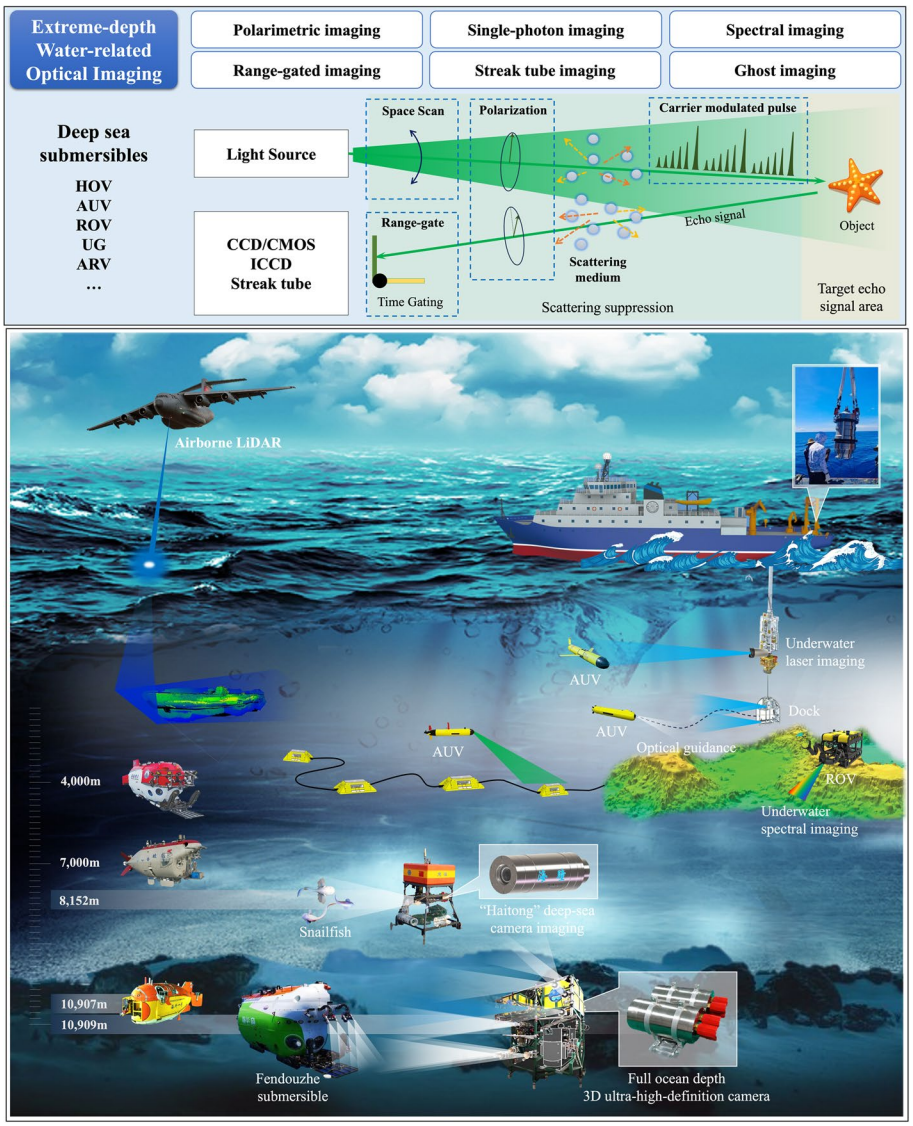

Fig. 1 Extreme-depth water-related optical imaging

absorbs red and infrared wavelengths, limiting effective penetration to blue-green spectra, which are preferentially utilized in systems like LiDAR and cameras [13, 14]. In the epipelagic zone (0 to 200 m), abundant sunlight enables passive RGB imaging but introduces strong color-channel imbalance and surface caustics that confound white-balance algorithms. Mesopelagic missions (200 to 1,000 m) must counteract the rapid exponential decay of natural light, compelling active illumination that in turn suffers from severe backscatter and power-limited laser safety margins. High-pressure environments, especially at depths exceeding 6,000 m, necessitate robust engineering innovations. Abyssal and hadal operations (>6,000 m) confront near-total darkness, 110 MPa hydrostatic pressure that deforms optical windows and induces birefringence, and temperature-induced drift in sensor calibration. One critical solution involves pressure-resistant enclosures, which protect deep-sea imaging systems from extreme compressive forces. Scattering, caused

by suspended particulates and turbulence, degrades image contrast and operational range [15]. To address this, advanced techniques have been developed to suppress scattering across multiple physical dimensions. Polarization imaging exploits differential polarization states to filter backscattered light [16]. Range-gated imaging temporally isolates photons reflected from targets using pulsed lasers and synchronized detectors. Single-photon imaging enhances sensitivity in ultra-low illumination conditions by detecting individual photons. Streak camera imaging achieves ultrafast temporal resolution to disentangle scattered and direct light paths. Ghost imaging (GI) reconstructs targets by utilizing second-order statistical correlations of optical fields and computational algorithms, enabling noise-resilient intensity correlation measurements [17–19]. By integrating spatial, temporal, spectral, and polarization domains, these multidimensional strategies significantly extend the operational capabilities of optical imaging systems under extreme-depth water-related conditions. From an application viewpoint, long-range airborne lidar bathymetry battles wave-induced refraction and solar background within the Fraunhofer H-β absorption line, whereas AUV docking demands centimeter-level pose accuracy under dynamic turbidity and refractive-index fluctuations. Benthic habitat mapping further requires hyperspectral fidelity across 400–900 nm while suppressing fluorescence contamination from marine snow. Collectively, these depth- and mission-specific hurdles necessitate modality-tailored solutions rather than generic image-processing pipelines.

This paper systematically reviews the foundational principles, inherent challenges, and state-of-the-art advancements in water-related optical imaging from epipelagic zone to Mariana Trench. First, we elucidate the physical foundations of light propagation in water-related environment, emphasizing wavelength-dependent absorption, forward/backward scattering mechanisms, and pressure-resistant designs. Next, we explore imaging methodologies spanning the epipelagic to hadal zones, including laser-based imaging systems, deep-sea submersibles and artificial intelligence (AI) driven computational imaging techniques. Finally, we highlight emerging AI-based solutions for image enhancement and restoration, and discuss key applications in resource exploration, ecological monitoring, and autonomous underwater navigation. This review provides a comprehensive review of water-related imaging methodologies for ultra-low-illumination environments and outlines promising research directions. By integrating optical physics, systems engineering, and computational imaging, it delineates a technology roadmap for robust sensing in ultra-low illumination conditions and for enabling access to the ocean's deepest frontiers.

Principle of the water-related optical imaging

Basic principle

Optical imaging in water-related environments relies on the propagation and interaction of light with water and its constituents. The medium is characterized by its inherent optical properties (IOPs). The beam attenuation coefficient $c(\lambda)$ represents the total loss of flux due to both absorption $a(\lambda)$ and scattering $b(\lambda)$, when Raman and fluorescence are negligible.

$$c(\lambda) = a(\lambda) + b(\lambda) \tag{1}$$

It is operationally defined using a collimated beam and a detector with infinitesimal angular acceptance as the exponential loss constant for on-axis flux, i.e., the distance over which the beam falls to 1/e of its initial value. Residual on-axis radiance thus decays nearly exponentially with range. Radiance reflected from an object undergoes the same extinction on the outbound and return paths, so the photon flux from reflective surfaces can be far lower than the volumetric signal returned by scattering, depending on range, the angular distribution of scattering relative to absorption, and the target's reflectance. The volume-scattering function (VSF) describes the angular redistribution of photons, and the single-scattering albedo $\omega_0(\lambda) = b/c$ quantifies the fraction of extinction due to scattering [9, 10]. Along a line of sight at range z, the direct (ballistic) radiance is attenuated by the Beer-Lambert transmittance, while the camera also records backscatter. Image contrast is further reduced by backscattered light integrated over the illuminated volume, which appears as a noncoherent background that adds to, and can overwhelm, scene radiance, especially at long integration times. In addition, forward scattering spreads light from each object point into a neighborhood, producing blur described by a characteristic point-spread function (PSF), which degrades spatial detail at increasing optical depth. Together, the recorded intensity combines attenuated object radiance, backscatter, and scatter-induced blur. This departs from the near-linear, weak-scatter regime typical of atmospheric imaging [20]. In addition, wavelength selectivity is strong in the water-related environments. The absorption increases sharply outside the blue-green window, and molecular/particulate scattering decreases with wavelength approximately as a Rayleigh or Mie-like power law (Fig. 2). Moreover, at interfaces, Snell refraction and Fresnel reflection modify ray paths and throughput. The refractive-index mismatch at the air-glass-water stack introduces spherical/chromatic aberrations unless corrected with index-matched domes or adaptive optics.

In conventional water-related optical imaging, contrast loss is the primary limitation, and the ballistic irradiance decays exponentially with range under the Beer-Lambert law. In the absence of scattering, the illuminance at 7 attenuation lengths (ALs) is reduced by roughly 10^{-5} relative to that at 1 AL, which creates a severe photon deficit. Low-light detectors such as streak cameras and ICCDs can therefore be valuable, yet usable information ultimately depends on the system signal-to-noise ratio (SNR). Against this backdrop, two complementary paradigms are employed to manage propagation losses and backscatter, active and passive imaging. The active imaging that uses controlled illumination, such as lasers, LEDs, or structured light, to probe a scene and record the returned signal with a time, polarization, phase, or intensity reference. Because the source is known and synchronized with the sensor, the system can gate in time, modulate patterns, or measure time-of-flight to extract depth, suppress backscatter, or estimate material properties [21]. The passive imaging that relies solely on ambient illumination to form images, without emitting its own probe light. The sensor records scene radiance and any derived quantities (e.g., color, polarization, spectrum), with image formation governed by the environment's lighting and the medium's transport properties (e.g., conventional, polarimetric, or spectral cameras) [22].

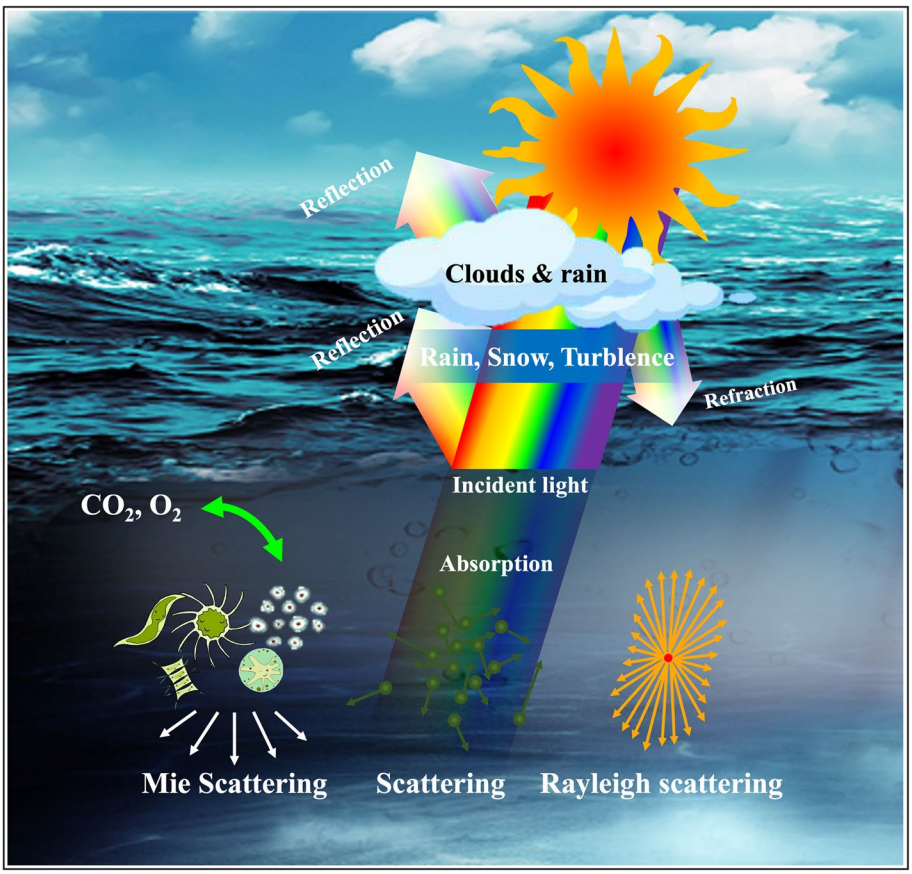

Fig. 2 Absorption and scattering in ocean

Challenges of water-related optical imaging

Optical propagation challenges

(1) Brief introduction

As light propagates underwater it is attenuated and redirected by wavelength-dependent absorption and scattering from water molecules and suspended constituents such as sand, plankton, and dissolved organics, yielding range-dependent spectral and radiometric changes. Selective absorption suppresses long wavelengths first, so blue-green bands dominate with depth. In clear ocean water blue penetrates farthest, whereas in turbid or biologically productive waters green can prevail. The recorded signal combines ballistic returns from the target with forward-scattered light that broadens the point-spread function and backscattered path-radiance that veils contrast. Flow-driven particle fields and microstructure further perturb ray trajectories, altering intensity, spectrum, and polarization. These coupled effects remain a central challenge for modeling and recovering optical information in water-related environments. We attempt to summarize the challenges faced in

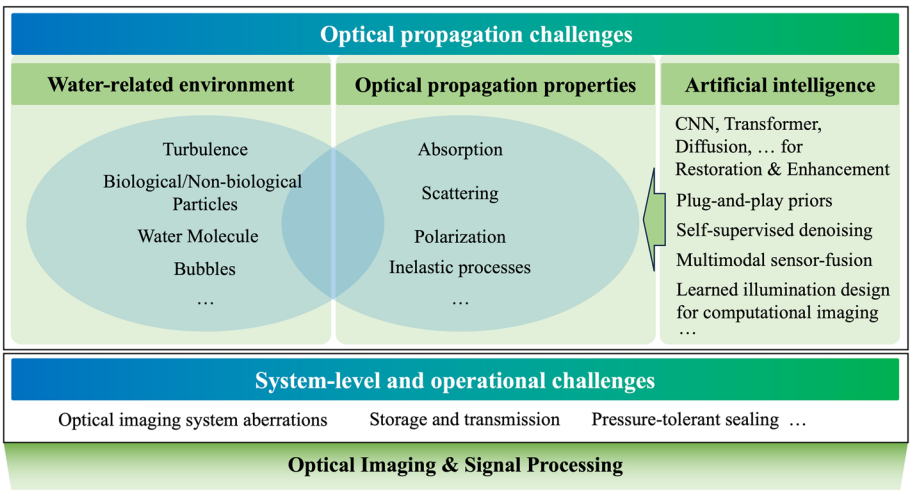

Fig. 3 Challenges of water-related optical imaging

underwater optical imaging and propose the current main research directions, as shown in Fig. 3.

(2) Absorption

Water selectively absorbs light depending on wavelength, governed by the Beer-Lambert Law [23]:

$$I(z) = I_0 e^{-a(\lambda)z} \tag{2}$$

where $I(z)$ is the irradiance at range z, I_0 is the initial irradiance, and $a(\lambda)$ is the total absorption coefficient. This coefficient combines contributions from pure water (a_w), chlorophyll (a_{chl}), dissolved organic matter (a_{CDOM}), and suspended particles (a_{NAP}):

$$a(\lambda) = a_w(\lambda) + C_{chl} \cdot a^*_{chl}(\lambda) + C_{CDOM} \cdot a^*_{CDOM}(\lambda) + C_{NAP} \cdot a^*_{NAP}(\lambda) \tag{3}$$

where, C_{chl}, C_{CDOM}, and C_{NAP} are concentrations, and a^* denotes specific absorption coefficients. $a_w(\lambda)$ denotes pure water absorption, $a_{chl}(\lambda)$ represents chlorophyll-a and accessory pigments, $a_{CDOM}(\lambda)$ a quantifies colored dissolved organic matter, $a_{NAP}(\lambda)$ accounts for non-algal particles, and $a_{MAA}(\lambda)$ captures UV-absorbing mycosporine-like amino acids in coastal organisms. Pure water exhibits a well-characterized absorption minimum at 420 nm ($a_w = 0.0064\ m^{-1}$) and maximum at 740 nm ($a_w = 2.8\ m^{-1}$) due to O–H bond vibrational overtones. Chlorophyll-a displays twin absorption peaks at 443 nm ($\sigma = 12$ nm) and 675 nm ($\sigma = 8$ nm). Therefore, blue-green wavelengths (470 to 580 nm) exhibit minimal attenuation, making them optimal for water-related optical imaging [24].

(3) Scattering

The propagation of light in oceanic environments is governed by complex interactions between electromagnetic radiation and the constituents of seawater. As light traverses through water, it undergoes various processes including absorption and scattering, which fundamentally limit the performance of water-related optical sensing and imaging systems. Thus, since the early days of water-related optical imaging, the challenges posed by light scattering in seawater have been a central focus of research [25].

a. Scattering Coefficient

Forward scattering refers to the deflection of light at small angles as it propagates through water, causing blurring in the image. This occurs because light that should have traveled directly from the object to the camera sensor gets scattered and arrives slightly off-target, diminishing the sharpness of the captured scene. It blurs the image and photons arrive at slightly shifted angles. Backscattering, on the other hand, occurs when light is scattered by particles in the water and redirected toward the camera. Backscatter adds noise and lowers contrast, especially in turbid water. As a result, most water-related imaging techniques are designed to mitigate the negative impacts of backscattering. The intensity of backscattered light is influenced by several factors, including the scattering coefficient, the absorption coefficient, and the distance between the object and the camera. Quantitatively, backscatter can be modeled by integrating $b(\lambda)$ along the path. The scattering coefficient $b(\lambda)$ represents the fraction of incident light that is scattered in all directions per unit distance [26]:

$$b(\lambda) = b_w(\lambda) + b_p(\lambda) \tag{4}$$

where, $b_w(\lambda)$ is the scattering by pure water, predominantly Rayleigh scattering. $b_p(\lambda)$ is the scattering by particles, predominantly Mie scattering.

The VSF, denoted by (θ,λ), describes the angular distribution of scattered light at wavelength λ and scattering angle θ:

$$\beta(\theta, \lambda) = \frac{d^2 I(\theta, \lambda)}{E_0(\lambda) dV} \tag{5}$$

where, $d^2I(\theta,\lambda)$ is the scattered intensity in direction θ. $E_0(\lambda)$ is the incident irradiance. dV is the volume element.

The scattering coefficient is related to the VSF through integration over all solid angles:

$$b(\lambda) = 2\pi \int_0^{\pi} \beta(\theta, \lambda) \sin\theta d\theta \tag{6}$$

The scattering coefficient $b(\lambda)$ and its integral relation to the $\beta(\theta,\lambda)$ provide the quantitative foundation for understanding water-related image degradation.

b. Rayleigh scattering

Rayleigh scattering occurs when the scattering particles are much smaller than the wavelength of light ($d \ll \lambda$). In oceanic environments, this primarily applies to water molecules and very small colloidal particles. In pure seawater, scattering is primarily governed by Rayleigh scattering, where the scattering intensity is inversely proportional to the fourth power of the wavelength. The molecular scattering coefficient for pure seawater can be expressed as [27]:

$$b_w(\lambda) = b_w(\lambda_0) \cdot \left(\frac{\lambda_0}{\lambda}\right)^n \tag{7}$$

where, $b_w(\lambda)$ is the molecular (Rayleigh) scattering coefficient of pure seawater at wavelength λ, typically in units of m^{-1}. λ is the target wavelength at which you want to evaluate the scattering coefficient. λ_0 is the reference wavelength, at which the scattering coefficient $b_w(\lambda_0)$ is known or empirically measured. n is the spectral exponent, which reflects the wavelength dependence of Rayleigh scattering. For pure seawater, empirical values typically use $n \approx 4.32$, slightly higher than the theoretical Rayleigh exponent of 4, to better match measurements.

As a result, the scattering coefficient decreases with increasing wavelength, making longer wavelengths less prone to scattering, as shown in Fig. 4. The Rayleigh-like power law is $b(\lambda) = b_0(\lambda_0/\lambda)^{\alpha}$, where $b_0 = 0.003\ m^{-1}$, $\lambda_0 = 550$ nm, $\alpha = 4.32$. In the blue-green spectral range, specifically from 450 to 570 nm, both the absorption and scattering coefficients of seawater are relatively low, which makes this range the optimal transmission window for light in oceanic environments. This spectral region's favorable characteristics are one of the key reasons why the 532 nm wavelength laser is widely adopted in water-related optical applications, offering a balance between minimal scattering and sufficient light penetration for effective imaging.

c. Mie scattering

Mie scattering applies to particles with sizes comparable to or larger than the wavelength of light. In oceanic environments, this includes suspended sediments, phytoplankton, and other particulate matter. The Mie theory provides an exact solution to Maxwell's equations for scattering by spherical particles. The scattered field is expressed as an infinite series [28].

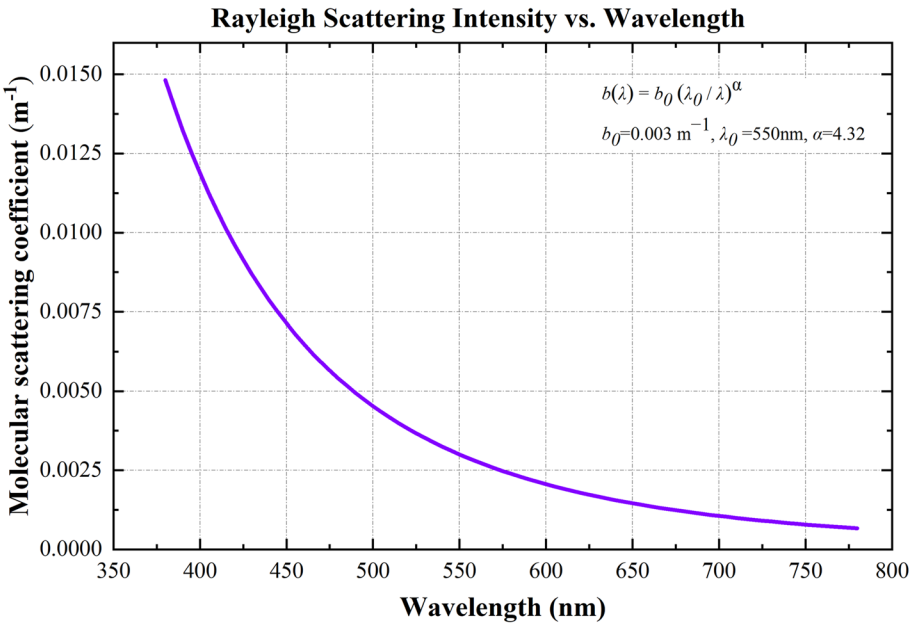

Fig. 4 The molecular scattering coefficient for pure seawater decreases sharply with increasing wavelength from 380 to 780 nm, following the Rayleigh-like power law

$$E_s = E_0 \frac{e^{ikr}}{-ikr} \sum\nolimits_1^{\infty} \frac{2n+1}{n(n+1)} [a_n \pi_n(\cos\theta) + b_n \tau_n(\cos\theta)] \tag{8}$$

where, E_o is the amplitude of the incident field. k is the wavenumber. r is the distance from the particle. a_{n} and b_{n} are the Mie coefficients. π_{n} and τ_{n} are functions related to Legendre polynomials.

The Mie coefficients are given by:

$$a_n = \frac{m\Psi_n(mx)[x\Psi_n(x)] - \Psi_n(x)[mx\Psi_n(mx)]}{m\xi_n(mx)[x\xi_n(x)] - \xi_n(x)[mx\xi_n(mx)]} \tag{9}$$

$$b_n = \frac{\Psi_n(mx)[x\Psi_n(x)] - m\Psi_n(x)[mx\Psi_n(mx)]}{\xi_n(mx)[x\xi_n(x)] - m\xi_n(x)[mx\xi_n(mx)]} \tag{10}$$

where, m the complex refractive index ratio. $x = 2\pi r/\lambda$ is the size parameter, r is the particle radius). ψ_{n} and ξ_{n} are Riccati-Bessel functions. The efficiency factors for scattering Q_s and extinction Q_e are calculated as:

$$Q_s = \frac{2}{x^2} \sum\nolimits_{n=1}^{\infty} (2n+1) \left(|a_n|^2 + |b_n|^2 \right) \tag{11}$$

$$Q_e = \frac{2}{x^2}\sum_{n=1}^{\infty}(2n+1)\Re(a_n + b_n) \tag{12}$$

Equation (10) and (11) shows the wavelength dependence of the scattering efficiency Q_s for a single, non-absorbing. Mie theory delivers an exact, yet computationally efficient, framework for predicting the scattering and absorption of light by spheres of arbitrary size and refractive index. In ocean optics, it underpins forward models that link measured bulk optical properties to the microphysics of suspended particulate assemblages. By pairing observed particle-size distributions and complex indices of refraction with the Mie equations, researchers can reproduce measured scattering phase functions and radiative-transfer coefficients. This, in turn, improves the retrieval of suspended-sediment or phytoplankton concentrations from remote-sensing reflectance.

A rigorous mathematical description of underwater optics via the inherent optical properties. Together with the volume-scattering function, underpins the performance limits and design choices of water-related imaging systems. The relative contributions of absorption and scattering depend on the composition and concentration of suspended particles and dissolved constituents, vary strongly with wavelength, and exhibit systematic geographic patterns. In the open ocean, transmission peaks in the blue-green window, with typical ALs of ~ 20 m, whereas in coastal waters elevated particulate and dissolved organic matter shorten ALs to ~ 3 to 5 m and shift the transmission maximum toward yellow [29]. Enabled by advances in optical hardware, computation, and signal processing, modern systems increasingly exploit these properties to operate effectively in more challenging regimes [30].

(4) Polarization

Polarization, one of light's fundamental attributes, encodes the orientation statistics of the transverse field and provides discriminative cues beyond intensity and color, enabling target detection under low SNR, cluttered backgrounds, strong scattering, and dim illumination. A monochromatic field propagating along the z-axis can be written as two orthogonal components [31]

$$E_x(t) = A_x e^{i(\omega t - kz + \phi_x)} \tag{13}$$

$$E_y(t) = A_y e^{i(\omega t - kz + \phi_y)} \tag{14}$$

Here, E_x and E_y are the complex electric-field components along the sensor's x and y axes. A_x and A_y are their real, non-negative amplitudes. $\omega = 2\pi f$ is the angular frequency for optical frequency f. $k = 2\pi n(\lambda)/\lambda_{vac}$ is the wavenumber in a medium of refractive index $n(\lambda)$ at vacuum wavelength λ_{vac}. ϕ_x and ϕ_y are constant phases.

The Stokes vector $S = [I,Q,U,V]^T$ captures the measurable polarization state. I is total intensity, $\langle |E_x|^2 + |E_y|^2 \rangle$. Q contrasts horizontal vs. vertical linear states, $\langle |E_x|^2 - |E_y|^2 \rangle$. U contrasts $+45°$ vs. $-45°$ linear states, $\langle 2\mathrm{Re}(E_x E_y^*) \rangle$. V measures right- vs. left-circular content, $\langle 2\mathrm{Im}(E_x E_y^*) \rangle$. Angle brackets $\langle \cdot \rangle$ denote a time aver-

age over many optical cycles. From S, the degree of linear polarization and degree of polarization are

$$DoP = \frac{\sqrt{Q^2 + U^2 + V^2}}{I} \tag{15}$$

with DoP $\in [0,1]$ indicating the polarized fraction of the field. Within the medium, multiple scattering drives depolarization, often captured by an empirical polarization memory model.

$$DoP(z,\theta) = DoP_0 exp\left[-\frac{z}{\ell_{pol}(\lambda,\theta)}\right] \tag{16}$$

where z is optical path length, θ denotes viewing/scattering geometry, DoP_0 is the source or target polarization at $z=0$, and $\ell_{pol}(\lambda,\theta)$ is an effective polarization-memory length set by the medium's single-scattering albedo and phase function. Typically, ℓ_{pol} is longer in forward-looking configurations than in backscatter, so polarization decays more slowly along near-forward paths. Air-glass-water interfaces and pressure windows further mix polarization via diattenuation and birefringence (angle and stress-dependent), introducing instrument and geometry biases that vary with depth and incidence angle [32].

These depolarization processes have concrete imaging consequences. Reduced DoP weakens edge and material contrast, while range and angle-dependent Stokes mixing biases quantitative estimates. Spatiotemporal variability in particle fields makes polarization signatures nonstationary, hindering transfer of laboratory calibrations to the field. Reliable polarimetric imaging in water therefore requires tight control of illumination and viewing geometry, full Mueller-matrix calibration of the optical train to remove instrumental polarization, and physics-aware inference that explicitly models depolarization and interface effects. When these measures are in place, often in conjunction with time gating or spectral selection to favor ballistic and singly scattered photons, polarimetry remains a powerful complement to intensity and color-based underwater vision.

In practice, the polarization state of a wave can be robust to phase-only distortions, so vector-structured beams retain polarization inhomogeneity despite optical aberrations and modest misalignments, which is advantageous for structured-light sensing [33]. Underwater, however, the medium alters polarization through multiple scattering, interface effects, and microbubble populations, producing range and geometry-dependent depolarization that varies even for identical materials, complicating material inference and classifier design [34]. Polarization signatures also depend strongly on observation geometry at interfaces such as bubble boundaries, and forward versus backward propagation channels diverge with distance, leading to decreased degree of polarization and reduced contrast at longer paths [35]. The polarimetric imaging can enhance edge saliency and target discrimination in clean

water, but requires careful control of illumination and viewing geometry, rigorous instrument polarization calibration, and models that account for medium-induced polarization changes to remain reliable in turbid, range-extended scenarios.

(5) Particles and turbulence

Underwater turbulence, driven by temperature-salinity microstructure, internal waves, and shear, introduces refractive-index fluctuations. These fluctuations act as a random, anisotropic phase screen along the optical path. For optical imaging, beam wander and angle-of-arrival jitter reduce coupling efficiency. They also induce motion-like blur. Scintillation broadens the irradiance distribution and lowers SNR. Phase-front corrugation degrades the optical transfer function and creates a space and time-variant point-spread function. Path-length fluctuations broaden photon time-of-flight and erode axial resolution in gated, SPAD, and streak-tube systems. These effects decorrelate structured illumination, diminish polarization purity, and impair phase/coherence-dependent modalities, with severity set by turbulence strength, inner/outer scales, stratification, and anisotropy [36, 37].

Furthermore, underwater turbulence modeling and measurement remain limited. Most forward models adopt isotropic, stationary spectra and Rytov-variance surrogates that only partially capture oceanic reality. They under-represent salinity-driven anisotropy, depth-dependent inner/outer scales, and non-stationarity across range. As a result, predicted scintillation, crosstalk among OAM states, and beam-array correlations often misalign with field performance, hindering robust algorithm design [38]. For imaging, this translates into calibration drift, PSF mismatch, and domain shift for learned restorers, particularly when in-air intrinsics or static underwater intrinsics are applied without refractive/turbulence correction.

(6) Inelastic processes

Inelastic processes impose several challenges for underwater optical imaging. Raman scattering adds a broad, Stokes-shifted background that rides on the elastic return and lowers contrast and SNR across wide spectral bands. This background varies with path length, illumination spectrum, and water chemistry, which breaks the assumptions of elastic-only image formation and biases color correction and reflectance retrieval. Fluorescence introduces narrow but intense emissions, most prominently near the chlorophyll-a band, that contaminate red and near-red channels and create spectral cross-talk for multispectral and hyperspectral sensors. Fluorescent lifetimes sit in the nanosecond range, so delayed photons leak into late gates and broaden photon arrival histograms, which degrades axial resolution for range-gated, SPAD, and streak-tube systems and complicates time-of-flight calibration. Both Raman and fluorescence are partially depolarized, which depresses the degree of polarization and corrupts polarimetric cues used for de-scattering and material inference. Their magnitudes are scene dependent and nonstationary in space and time, which undermines radiometric stability and hinders transfer of laboratory calibrations to the field. Together these effects produce additive backgrounds, temporal tails, and polarization dilution that, if unmodeled, lead to systematic errors in restoration, classification, and 3D reconstruction [39–41].

(7) Artificial intelligence (AI) enhanced signal processing

AI methods for water-related optical imaging face severe, space and time-varying degradations. The medium imposes wavelength-dependent absorption, forward scatter, and backscatter. Then, the images exhibit color cast, blur, and low visibility. These factors shift the image distribution away from terrestrial data and vary with site, season, depth, water type, and platform, making learned models brittle when deployed outside the conditions seen during training [42].

First, data and supervision compound these physics-driven difficulties. Public underwater corpora are heterogeneous in sensors, optics, lighting, water types, and annotation protocols. Many data are partial or no longer accessible, and evaluation practices vary issues that frustrate reproducible training and fair comparison of enhancement or restoration models. For imaging, an added challenge is the scarcity of paired "clean" ground truth, which pushes practitioners toward unpaired, self-supervised, or synthetic supervision; this, in turn, raises concerns about domain fidelity and generalization when models trained on one site or simulator are deployed elsewhere [43, 44].

Second, objective mismatch further limits progress. Improvements in perceptual quality delivered by conventional underwater image enhancement are not reliably predictive of downstream utility, because the losses and metrics used to train enhancement networks are only loosely related to task- or physics-faithful fidelity. Thus, it is really necessary to incorporate measurement models, priors on light transport, or end-use awareness rather than relying solely on generic perceptual scores [45].

Third, generalization and domain shift remain central. Methods transferred from generic vision often underperform in underwater settings because they implicitly assume stable illumination, neutral color statistics, and haze-free edges, assumptions violated underwater. Models must therefore learn features and normalizations that are robust to medium-induced distortions and platform variability and should be stress-tested across diverse sites rather than a single dataset [46, 47].

Finally, deployment imposes stringent efficiency and reliability constraints. Long-range missions on AUV/ROV platforms operate under tight energy budgets and limited on-board computer [48]. Maintaining real-time throughput with physically grounded, uncertainty-aware processing is non-trivial. The challenge therefore lies in the co-design of compact models, quantization, and algorithm hardware tailored for marine platforms.

System-level and operational challenges

(1) Optical imaging system aberrations

Underwater optical systems inherit lens-design residuals and acquire additional errors at the air-glass-water interfaces. Refraction shifts the effective entrance pupil, alters focal length, and induces field- and depth-dependent distortions and chromatic dispersion, degrading inference when in-air intrinsics are applied underwater. Hydrostatic pressure and temperature induce elastic deformations and wedge in

windows, mounts, and barrels. In addition, stress birefringence in thick viewports and angle-dependent Fresnel coefficients introduce polarization diattenuation and retardance. These factors produce a space-variant, wavelength-dependent wavefront error that differs fundamentally from in-air calibration [49].

Monochromatic aberrations (spherical, coma, astigmatism, field curvature, distortion) reduce the modulation transfer function and yield PSF that broaden and rotate across the sensor. Chromatic aberrations are amplified because glass and water disperse differently. The longitudinal chromatic shift defocuses bands, and lateral chromatic error misregisters color channels and biases stereo, mosaicking, and hyperspectral unmixing. Polarization aberrations contaminate Stokes measurements and degrade division-of-focal-plane polarimeters. Stray light and ghost reflections at high-index interfaces add veiling flare, compounding contrast loss from backscatter. Biofouling, window contamination, and micro-bubbles further perturb the PSF and radiometry.

Because underwater aberrations vary with field angle, depth, wavelength, pressure, and temperature, they are nonstationary. This invalidates fixed PSF assumptions and degrades blind deconvolution. It also complicates transfer of laboratory calibrations to the field. Robust evaluation therefore requires in-water metrics, field-resolved MTF/PSF maps, spectral radiometry, time-of-flight impulse responses, and Mueller-matrix stability, acquired over operating depths and temperatures. Meeting these requirements is difficult on submersible payloads and during long missions [50].

Addressing underwater imaging aberrations requires a system-level approach that co-optimizes optics, calibration, and computation under realistic mission and environmental constraints. At the hardware layer, designs should manage the air-glass-water interface, minimize depth-induced deformation, and suppress stray light and polarization artifacts. Calibration must move beyond in-air intrinsics to ray-traced intrinsics that encode interface geometry and indices, augmented by field-resolved PSF/MTF and Mueller-matrix measurements across depth, temperature, and wavelength. Computational correction should then apply deblurring and denoising, with adaptive optics or computational wavefront sensing used where feasible to reduce residual phase error. Finally, physics-guided AI-unrolled deconvolution, domain-adaptive or self-supervised training from in situ constraints, can close residual gaps [42].

Imaging through the air-glass-water stack introduces refraction at each interface. Snell refraction changes effective focal length, shifts the principal point, and induces field- and depth-dependent distortions and chromatic dispersion, degrading inference when in-air intrinsics are applied underwater [35]. Robust operation therefore requires refractive calibration that accounts for interface geometry and refractive indices, or hardware designs that preserve central projection. In situ cali-

bration with underwater targets and wavelength-aware radiometric checks further stabilizes downstream algorithms [36].

(2) Storage and transmission

High-resolution HD and 4 K imaging substantially raise scientific yield in underwater inspection, mapping, and ecology, but they also multiply data rates, storage needs, and compute loads. Frame sizes and frame rates escalate linearly into multi-Gb/s streams for uncompressed video, stressing the size-weight-power budgets of submersible payloads and the reliability of long-duration deployments. Algorithms that are now standard, dehazing, stabilization, mosaicking, stereo/SLAM, and AI inference, must operate at higher pixel counts and tighter latencies, which increases onboard power draw and thermal load and complicates real-time operation.

Local storage is the simplest acquisition path but has practical drawbacks underwater. Storage capacity, file system limits, and write-speed ceilings cap recordable duration and frame quality, and the risk of single-point failure argues for redundancy. Where feasible, live export to an external recorder is preferred to decouple acquisition from storage and to enable immediate monitoring and quality control. For tethered platforms, live transmission typically rides fiber using established interfaces. Gigabit Ethernet supports IP streaming and control, while HDMI and HD-SDI transports carry high-resolution video, up to HD and 4 K at frame rates on the order of 60 fps, over deterministic links. Even so, bandwidth and latency budgets force trade-offs among compression, resolution, and frame rate. Uncompressed links simplify processing but demand higher link margin, whereas compressed delivery reduces bitrate at the cost of codec latency and potential artifacts.

(3) Pressure-tolerant sealing

Underwater environments impose stringent operational constraints, optical imaging device access is limited by depth, currents, visibility, and safety windows. China's deep-sea exploration technology achieved a milestone breakthrough in 2020 with the manned submersible Fendouzhe successfully reaching the depths of the Mariana Trench Challenger Deep [51]. Its indigenously developed titanium-alloy pressure hull received international certification, signifying China's attainment of world-leading capabilities in FOD pressure resistance technology. This manned cabin, manufactured via electron beam welding, features a 2.1 m diameter spherical structure. Remarkably, the weld strength achieved exceeds 95% of the base material strength, ensuring exceptional sealing and structural integrity even under the extreme pressures at FOD, thereby demonstrating the robustness of fundamental industrial processes. However, the sustained advancement of deep-sea equipment continues to face multifaceted technical challenges. Cameras intended for FOD operation (depths beyond 11,000 m, ~ 110 MPa hydrostatic pressure) require carefully engineered sealing solutions to remain leak-tight under extreme conditions. At these hadal pressures, traditional sealing methods face several challenges. Elastomeric O-rings, the most common seals, experience hydrostatic compression and material shrinkage that alter their sealing interference. High ambient pressure can reduce an O-ring's volume and diametral compression, potentially leading to seal leakage if the initial squeeze was insufficient. Moreover, long-term stress-relaxation and creep of polymer seals are further accelerated by high pressure and the 2 to 4 °C

ambient temperatures typical of deep water [52]. Continuous immersion in saltwater, and occasional exposure to hydraulic oils, requires sealing compounds that resist swelling, hydrolysis, and corrosion. At the optical port, adhesives and encapsulants around the lens window must also remain transparent and dimensionally stable to avoid distorting the transmitted wavefront [53]. Reliable imaging in the hadal realm therefore requires a holistic sealing strategy that couples mechanical robustness with optical integrity.

Recent advances in deep-ocean optical housings have crystallized around three synergistic strategies. First, high-performance thermoplastics such as PTFE and PEEK retain dimensional stability, extremely low permeation and chemical inertness at static pressures approaching 110 to 120 MPa, while carbon- or glass-fiber reinforcements halve long-term creep strain and suppress cold-flow without degrading machinability [54, 55]. Second, flooding the housing with an optically clear, dielectric oil and coupling it to ambient seawater via a bellows, bladder or piston equalizes internal and external pressures, thereby eliminating radial loads on seal lips and viewports [56]. Third, Kovar-to-glass feed-throughs joined by radial metal C-ring seals routinely achieve helium leak rates below 1×10^{-9} mbar·L/s and offer coefficients of thermal expansion of about 4 to 6 ppm/K, closely matching borosilicate or sapphire and thus mitigating stress-induced birefringence and focus drift over ± 50 °C thermal excursions. Finite-element models of 25 mm-thick sapphire windows loaded to 110 MPa predict peak von Mises stresses at least 25% below the yield strength of reinforced-PEEK seats and transmitted-wavefront error under $\lambda/10$ across 400 to 700 nm [57, 58]. Hyperbaric-chamber dwell tests of identical assemblies for 72 h at the same pressure confirm leak-free operation and optical throughput within 1% of atmospheric benchmarks. These pressure-tolerant sealing systems now underpin abyssal imaging sensors, including cameras rated to 11,000 m and emerging deep-sea lidar modules, enabling month-long deployments for benthic biodiversity surveys, geomorphological change detection and in-situ calibration of satellite ocean-color algorithms.

(4) Imaging payload platform

Underwater optical imaging places stringent demands on the deployment platform because platform dynamics directly govern image sharpness, exposure stability, and targeting. Diver-operated cameras are effective in shallow water but are unsuitable for continuous or deep (> 30 m) surveys. Fixed landers provide the highest stability, ideal for long, unblurred time series of stills and video, at the cost of spatial coverage. ROVs offer good station-keeping and allow detailed imaging with moderate mobility, while AUVs trade precise station-keeping for extended range, endurance, and fully autonomous operation. Towed systems enable wide-area, cost-effective surveys with large payloads but introduce motion, altitude, and heading variability that can blur imagery and complicate focus, especially over rough terrain. Across all platforms, residual motion, vibration, and hydrodynamic disturbances remain primary risks for blur and misregistration [59].

These engineering constraints degrade the performance of underwater reconstruction systems, and in-air optical designs and algorithms rarely satisfy operational requirements in water. Meeting practical needs therefore demands domain-specific

advances in optics (e.g., pressure-tolerant, blue-green, low-scatter illumination, refractive-interface correction) and algorithms (e.g., physics-based restoration, robust calibration, uncertainty modeling), with particular emphasis on ultra-low-illumination regimes.

Water-related optical imaging from epipelagic zone to Mariana Trench

Light source

In 1963, Duntley identified an optical attenuation window in the blue-green wavelength region, demonstrating the feasibility of water-related detection and communication using blue-green light [60]. Subsequent studies by Smith and Baker revealed that pure and clear seawater exhibits minimal attenuation of blue light, particularly within the deep-blue spectral range (450 to 485 nm), where transmission loss is only about 1% of that in other wavelength bands [61]. This characteristic significantly enhances laser transmission efficiency and provides a practical basis for water-related laser-based detection and communication. However, laser attenuation in seawater still varies considerably depending on water quality. According to the water type classification described by Jerlov [62] and subsequent optical measurements of Jerlov water types [63], the optimal transmission wavelength differs across various types of seawater. In coastal and shallow sea areas, the optimal optical transmission window is around 510 to 550 nm, whereas in open ocean and deep-sea waters, it shifts toward shorter wavelengths, with peak transmission occurring in the blue range of 450 to 490 nm [62, 63]. The existence of this blue-green window opens new possibilities for marine applications. When combined with the high brightness, strong directionality, narrow linewidth and high-peak-power of pulsed lasers, blue-green light enables cross-medium ocean remote sensing and supports high-capacity, high-data-rate underwater optical communication [64].

The most representative methods and sources for generating blue and green lasers are illustrated in Fig. 5. In the context of oceanic lidar systems, the development of high-performance pulsed lasers has prioritized high peak power and spectral

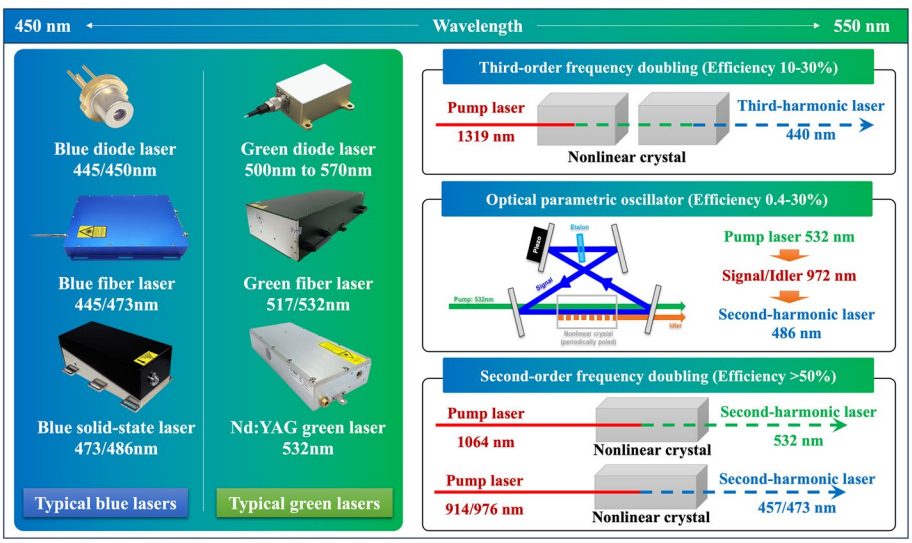

Fig. 5 Typical blue/green laser generation methods and sources

stability [65]. Among these, the predominant and technologically mature solution employs neodymium-doped yttrium aluminum garnet (Nd:YAG) lasers as the gain medium. Specifically, a semiconductor laser diode-pumped Nd:YAG crystal emits at the fundamental wavelength of 1064 nm in the near-infrared regime. This output is subsequently converted to 532 nm green pulses via second-harmonic generation (SHG), leveraging nonlinear optical crystals such as potassium titanyl phosphate (KTP) or lithium triborate (LBO) [66–70]. This approach dominates current applications due to its proven reliability, conversion efficiencies exceeding 50%, and compatibility with high-repetition-rate operation, critical for airborne and shipborne lidar deployments. In contrast, there are multiple technical routes for generating high-peak-power blue pulsed lasers. One common approach involves using a quasi-three-level Q-switched laser doped with Nd^{3+} ions, pumped by a semiconductor diode to produce a fundamental laser pulse at ~ 0.9 μm, which is then frequency-doubled to obtain blue laser pulses. The advantage of this method lies in its relatively high energy conversion efficiency due to the requirement of only a single frequency-doubling process. However, the major challenge is the efficient generation of the ~ 0.9 μm fundamental pulse [71]. Another mainstream method involves using pulsed laser-pumped optical parametric oscillators (OPO), and third-harmonic generation to obtain blue laser output [72–74]. These approaches allow for cascaded amplification to boost pulse energy, but their energy conversion efficiency is relatively low, ranging from 0.4% to approximately 30%. While THG offers tunability and broader spectral coverage, its complexity and reduced efficiency present trade-offs compared to direct frequency-doubling methods. In practice, SHG dominates for green (532 nm) in airborne/shipborne systems, whereas blue generation trades off THG/OPO flexibility against added complexity and reduced conversion efficiency, chosen according to the platform's power, stability, and spectral requirements.

Currently, the effective suppression of solar background noise is key to achieving stable, all-day performance of water-related laser systems. Within the blue-light transmission window of seawater, a notable Fraunhofer absorption line (the H-β line) exists at a central wavelength of 486.13 nm [75]. It is evident that aligning the laser source's central wavelength with the solar spectral dark line markedly suppresses solar background radiation at the receiver. Moreover, both the laser linewidth and the photodetector filter bandwidth should be kept narrower than the H-β line's spectral width of about 0.1 nm, as demonstrated in single-frequency OPO systems at 486.1 nm [76, 77]. Together, these measures greatly enhance the photodetection SNR. For deep-sea applications, even shorter wavelengths in the deep-blue region are required. Deep-blue laser output at 473 nm with high repetition frequency can be achieved through direct generation using GaN-based laser diodes or by frequency doubling vertical-cavity surface-emitting lasers (VCSELs), though these methods are limited in peak power [78, 79]. Alternatively, fiber-laser-based frequency doubling can also produce high-repetition-rate 473 nm output, but the low damage threshold of optical fibers restricts their ability to handle high-peak-power pulses and increases susceptibility to strong nonlinear effects, leading to laser degradation [80]. Therefore, the most promising solution is to use solid-state lasers to generate high-peak-power, high-repetition-rate 473 nm deep-blue laser pulses [81, 82].

With the continuous expansion of laser applications in ocean science, there is growing demand for all-solid-state blue-green lasers capable of high repetition rate with high

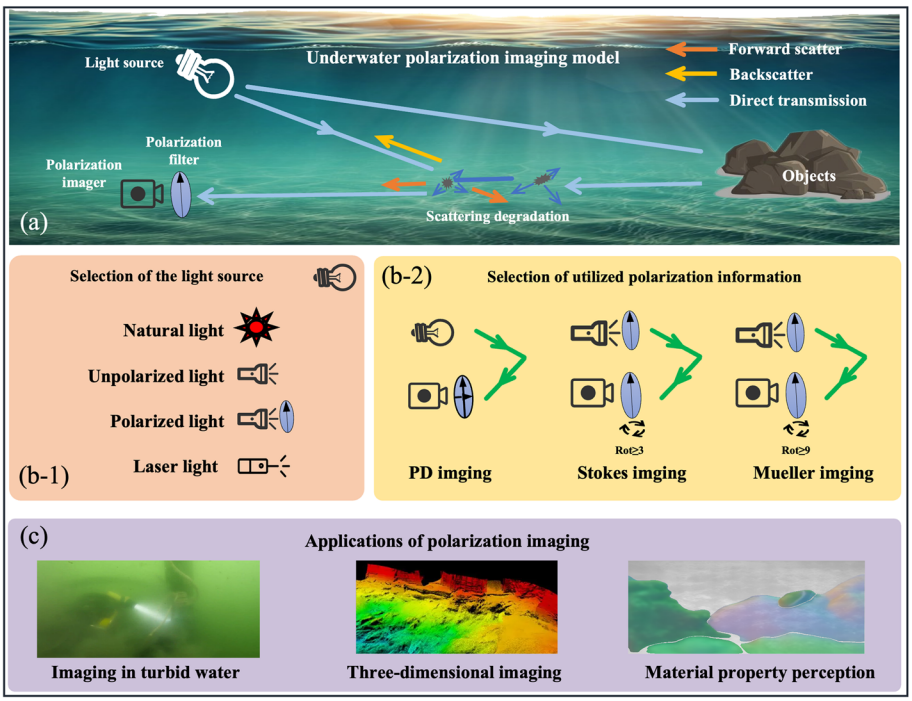

Fig. 6 **a** Water-related polarimetric imaging (PD) model. (b-1) Selection of the light source. (b-2) Selection of utilized polarization information. **c** Applications of polarimetric imaging

pulse energy. The increasing application of hyperspectral technologies in marine exploration further drives the need for single-frequency, frequency-stabilized blue-green lasers with high pulse energy output. Current nonlinear harmonic generation techniques, particularly parametric oscillation/amplification schemes seeded by single-frequency sources, can produce narrow-linewidth, high energy blue laser pulses with peak powers over the megawatt level, which are suitable for marine lidar applications. However, these systems are often limited by the complexity of frequency conversion processes, low efficiency, and susceptibility to wavelength drift. One of the most critical challenges is that high-peak-power ultraviolet laser irradiation can cause optical damage to components and nonlinear crystals, which can seriously affect the stability and reliability of the system. Additionally, at high peak power densities, the spontaneous emission effect of the laser gain medium becomes prominent, further impacting performance [83, 84]. Therefore, identifying high-quality gain media capable of directly emitting in the blue spectral region or achieving blue light output through a single-stage harmonic conversion process, along with the development of efficient laser modules, is expected to be a key direction for the future development of high-energy, high-repetition-rate blue pulsed lasers.

Polarimetric imaging

Principle

Polarimetric imaging technology leverages the polarization properties of light to enhance image quality in water-related environments, particularly in highly scattering conditions [85–88]. Its core principle relies on the partial polarization of scattered

light and the distinct polarization characteristics between targets and water-related medium [85]. By capturing and processing the polarization information of a scene, this technique suppresses scattered light and extracts the light reflected from the target, thereby improving image contrast and clarity [89–91]. The typical system setup for water-related polarimetric imaging, as illustrated in Fig. 6 (a), consists of a light source, polarization filter, and imaging device. The light source can be natural light, unpolarized light, or polarized light, which illuminates the water-related scene. The polarization filter selectively captures light based on its polarization state, allowing differentiation between back-scattered light and directly transmitted light from the target. The imaging device, such as a polarization-sensitive camera, then records the filtered light to produce images that can be further processed to reveal detailed information about the scene, such as target structure, depth, or material properties [92].

Polarimetric imaging methods

Typical water-related polarimetric imaging systems fall into three main categories, as illustrated in Fig. 6 (b). Polarization difference imaging employs two orthogonally polarized sub-images to estimate transmittance via the degree of linear polarization [91–93]. Stokes polarimetric imaging, particularly full-Stokes approaches, leverages the stability of polarization angles or circular polarization "memory effect" to suppress backscatter [94, 95]. Mueller matrix imaging provides a complete characterization of polarization behavior through matrix decomposition [96–98]. These methods rely on distinct optical architectures, offering versatile solutions for varying water-related applications. Additionally, integrating polarization data into computer vision and learning-based frameworks can further enhance image quality, expanding use cases in target detection, environmental monitoring, and water-related archaeology, as illustrated in Fig. 6 (c).

Schechner et al. [85] pioneered a descattering model for turbid water using polarized illumination in Fig. 7 (a-1), demonstrating effective contrast and color recovery for submerged objects like an iron box in Fig. 7 (a-2) [91]. However, their model assumes object radiance is unpolarized, which breaks down for low-depolarizing materials, leading to inaccurate transmittance estimation. Huang et al. [99] highlighted this issue, noting negative transmittance values (Fig. 7 (b-1)), and addressed it by fitting the target's polarization difference image within a feasible region, successfully restoring details in both high- and low-depolarizing scenes (Fig. 7 (b-5)). Liu et al. [100] further advanced the field by proposing a red-light-based polarization imaging method optimized for turbid water, enabling visibility of previously undetectable targets while balancing imaging range and clarity (Fig. 7 (c)).

Recent advancements in deep learning (DL) have significantly enhanced polarimetric imaging, focusing on polarization information processing [101–103]. Hu et al. introduced a polarimetric dense network (PDN) for water-related polarimetric image restoration, as shown in Fig. 8 (a). The PDN, comprising shallow feature extraction, a residual dense block, and dense feature fusion, extracts and fuses features from three polarization images, yielding detailed results compared to intensity-only methods. Yang et al. [103] developed an end-to-end unsupervised generative network using adversarial loss to remove backscattered light. By modifying the water-related imaging model with physical priors, such as matching the Degree of Polarization of backscatter to

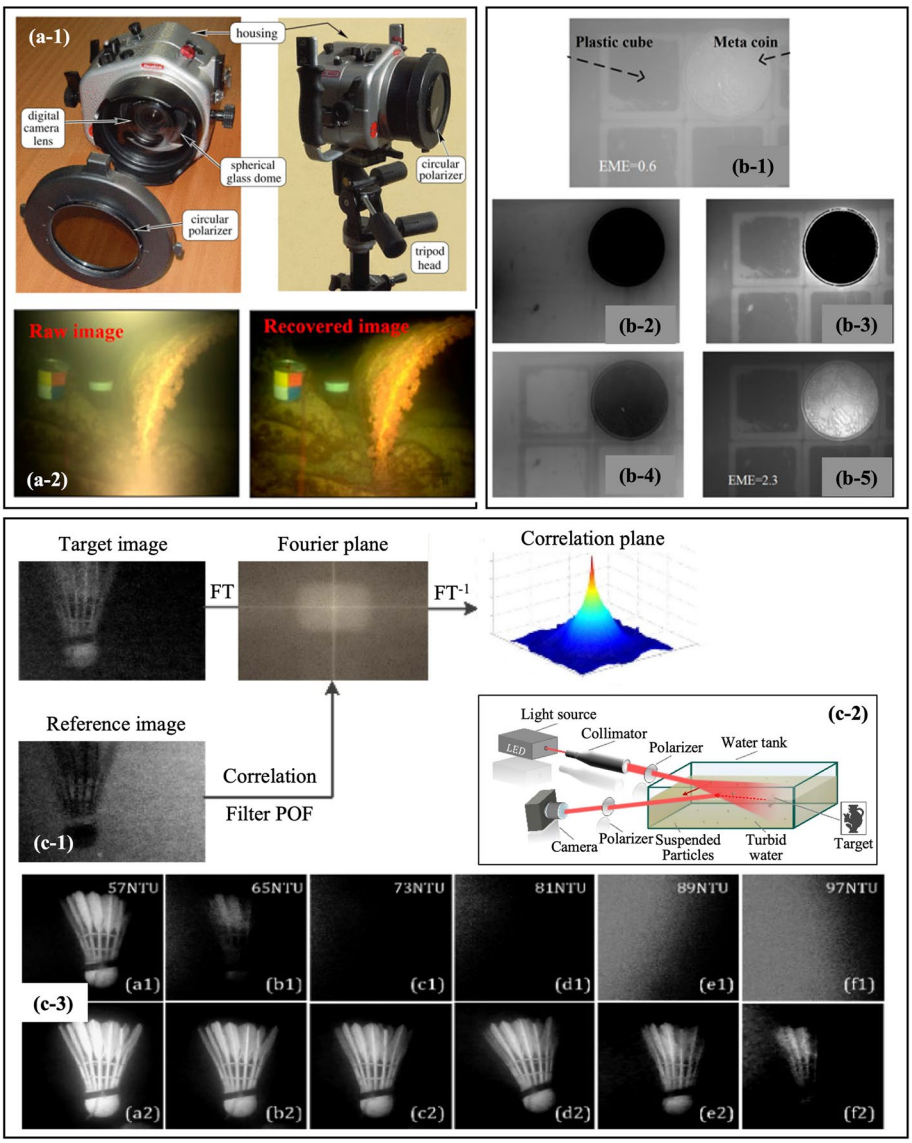

Fig. 7 (a-1) Imaging system. (a-2) Imaging result based on Schechner's model [91]. (b-1) Raw image. The deduced (b-2) transmittance and the recovered (b-3) radiance of the objects when the light emanating from objects in the scene is unpolarized. The retrieved (b-4) transmittance and (b-5) radiance of the objects by Huang's method [99]. (c-1) Synoptic diagram; FT denotes Fourier transform. (c-2) Experimental arrangement for imaging in highly turbid water. (c-3) Detection results with blue light illumination, and from the proposed method in water with gradually varied turbidity [100]

background light, this method adapts to non-uniform optical fields. Similarly, Zhu et al. [104] proposed a non-GAN unsupervised method combining polarization physics and DL (Fig. 8 (b-1)). Using U-Net, they processed polarimetric hazy images and computed loss between generated and captured images. Figure 8 (b-2) shows this method effectively removes homogeneous scattering in background areas while preserving object details, eliminating the need for paired or haze-free datasets.

Data-driven techniques are increasingly merged with physical models to direct network training, tackling the constraints of traditional techniques [32, 105]. They enable the extraction of more extensive features, adapt to complex scattering media,

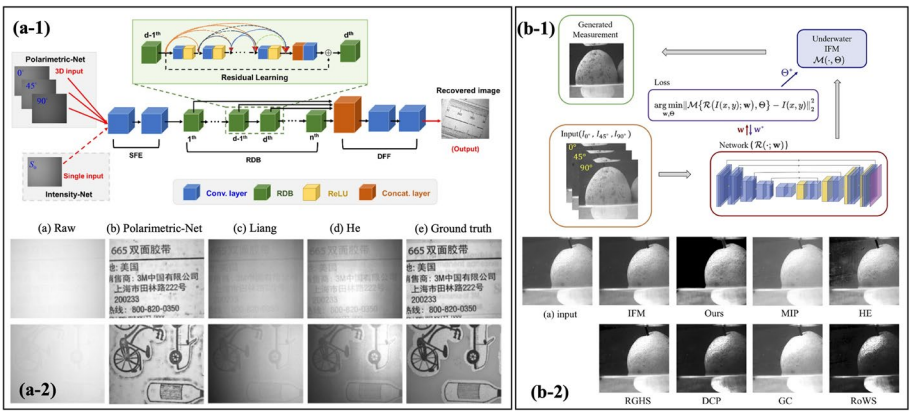

Fig. 8 (a-1) The architecture of PDN and (a-2) recovered image [103]. (b-1) The architecture of untrained network and (b-2) visual comparison among different de-scattering methods [104]

Table 1 Representative water-related polarimetric imaging systems [108–114]

System	Institution	Depth range	Device	Type
Polarimetric De-scattering Camera	Tianjin Univ. & Xiamen Univ	~0.6 m tank, high turbidity	12 MP DSLR + rotating pol. filter	Passive
Auto Stokes Imaging	Northwestern Polytechnical Univ	~Lab tank tests (various turbidities)	CCD with rotating polarizer	Passive
One-Shot Polarization Camera System	Ocean Univ. of China & CAS	~1 m tank, moderate turbidity (milk or sediment)	Division-of-focal-plane polarimeter	Passive
Passive Polarization Image Dataset	Dalian Maritime Univ	Shallow coastal waters, ~1–2 m visibility	GoPro-based rig + linear polarizers	Passive
Polarization-Enhanced Range-Gated Camera	SUSTech & SIAT, CAS	~0.5–0.6 m (lab)	Gated camera	Active
Laser Pol. Backscatter Suppression System	Institute of Oceanology, CAS	Up to 10 m (lab)	CMOS polarimetric camera	Active
Circular-Polarization LiDAR Prototype	Xi'an Inst. of Optics & Precision Mech., CAS	~2 m (lab)	CMOS camera + polarizers	Active

and enhance training efficiency via self-supervised, closed-loop optimization [106, 107]. However, obtaining suitable datasets for training remains a key challenge. While synthetic and generative approaches offer potential solutions, they continue to present significant obstacles for future progress.

Table 1 summarizes recent active and passive polarimetric imaging architectures for water-related vision. Current water-related polarimetric imaging bifurcates into active and passive paradigms with distinct operating envelopes and trade-offs. Active systems couple controlled linear or circular laser illumination with time-gating or time-of-flight detection to reject multiply scattered photons, thereby extending range in turbid media and achieving centimeter-scale resolution over several ALs despite predominantly prototype-level maturity. Their advantages in penetration and depth accuracy are balanced by higher system complexity, power and eye-safety constraints, and stringent calibration needs, with ongoing work on circular polarization, polarization-enhanced backscatter suppression, and improved radiometric/Stokes calibration. Passive systems rely on natural downwelling irradiance and acquire Stokes information either sequentially (rotating analyzer) or instantaneously via division-of-focal-plane sensors; they are compact

and low power, consistently improving contrast and feature visibility in mildly to moderately turbid, shallow waters (visibility ≈ 1 to 2 m), yet are limited to daylight operation, reduced penetration, and potential temporal misregistration in sequential capture. Across both paradigms, contemporary research increasingly integrates polarimetry with deep-learning restoration and advanced optics to elevate image fidelity while reducing size, weight, and power, with the field trending toward compact snapshot polarimeters plus physics-aware algorithms for passive use cases and polarization-augmented gated LiDAR for active deployments in turbid waters.

Range-gated imaging

Principle

Range-gated imaging isolates a chosen depth slice by synchronizing short laser pulses with an ultrafast electronic shutter at the detector. The transmitter emits a brief burst of light into the water column; the receiver opens its gate after a programmable delay that corresponds to the two-way travel time to the desired range, then closes within a few hundred picoseconds to a few nanoseconds. Photons returning from shallower ranges arrive earlier and are rejected, while photons from the target slice, primarily ballistic and singly scattered, are admitted (Fig. 9). Because only a thin axial layer contributes during the open interval, near-field path radiance and multiply scattered foreground light are strongly suppressed, yielding higher contrast and improved signal-to-noise ratio under turbidity. The temporal width of the gate determines the thickness of the imaged slice. Shorter gates produce finer depth separation but admit fewer photons, whereas longer gates increase photon counts at the cost of more residual in-gate backscatter [115].

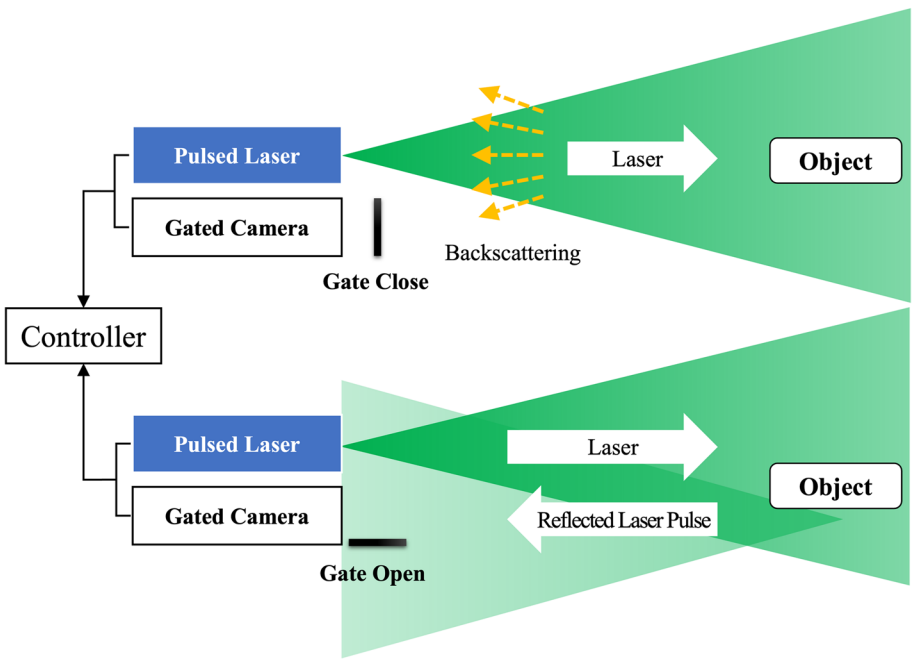

Fig. 9 Principle of range-gated imaging

Practical systems pair blue-green sources, where seawater attenuation is lower, with fast shutters such as gated image intensifiers, Pockels cells, or single-photon avalanche detector arrays operated in gated mode. Key timing parameters include the laser pulse width, the gate rise and fall times that set slice sharpness, and timing jitter between the source and sensor that broadens the effective slice. Spectral and polarization filters are commonly integrated to reject out-of-band glow, bioluminescence, and cross-polarized backscatter, further improving SNR. Performance reflects several coupled trade-offs. Narrow gates and precise synchronization maximize axial resolution and minimize in-gate haze but reduce photon budgets and increase sensitivity to timing drift. Wider gates improve throughput but admit more multiply scattered light. Residual errors arise from in-gate multiple scattering in very turbid water, platform motion during the open interval, speckle from coherent illumination, and calibration drift of the instrument response [116].

First proposed by Gillespie et al. [117] in the 1960 s, range-gated imaging remained impractical for decades due to optoelectronic limitations. In the 1990 s, Canada's DRDC achieved notable progress with the LUCIE series systems [118–120]. RGI enables time–space mapping by establishing precise delays between laser pulses and sensor gating, allowing selective capture of spatial "slices" at specific ranges. Two 3D imaging approaches have since evolved. On the one hand, time-slice scanning acquires sequential gated images via fine delay stepping for volumetric reconstruction, but suffers from high data loads and limited real-time performance [121]. On the other hand, energy-versus-range correlation imaging reconstructs depth from only two gated frames, enabling video-rate acquisition [122, 123]. A typical range-gated imaging system includes a pulsed laser, a gated sensor, and a timing control unit (TCU). The TCU synchronizes laser emission with sensor gating, adjusting delay, pulse width, and repetition rate. As depicted in Fig. 10, the laser pulse propagates through the medium, reflects off the target, and the gate opens just as the return photons arrive. A CCD or CMOS focal-plane array then records the gated signal, yielding a high-contrast image confined to the target range.

When the temporal offset between the laser-emission pulse and the gating pulse is τ, the standoff range R of the gated slice is [124]:

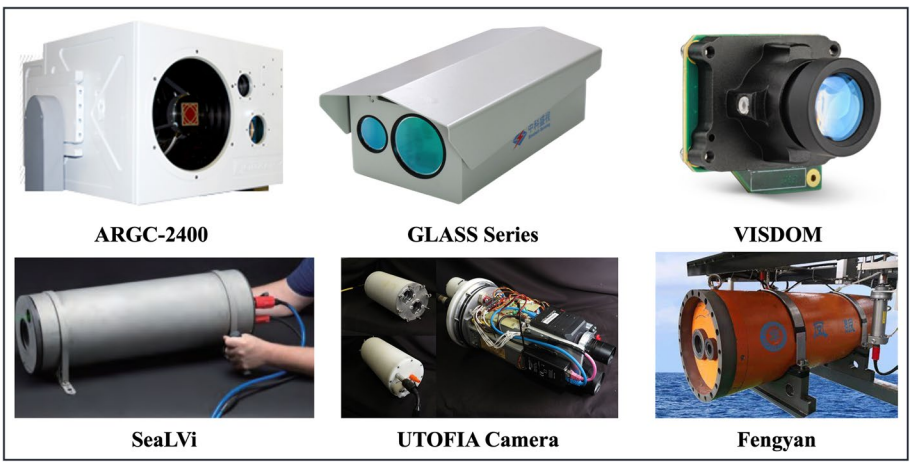

Fig. 10 Representative gated imaging system

$$R = \frac{\tau c}{2n} \tag{17}$$

When the gate width is t_g and the laser pulse width is t_L, the depth of field d of the gated slice is:

$$d = \frac{(t_g + t_L)c}{2n} \tag{18}$$

where, c is the speed of light in vacuum, and n is the refractive index of the transmission medium. Theoretically, laser range-gated imaging is achieved by convolution of the laser pulse function $P(t)$ and the gated pulse function $G(t)$. The target echo signal energy $I(r)$ at distance r is:

$$I(r) = \eta_r \eta_L \frac{\rho}{\pi MN} \frac{A_r}{r^2} exp(-2\sigma r) \int_{\tau}^{\tau + t_g} P\left(t - \frac{2rn}{c}\right) G(t - \tau) dt \tag{19}$$

Here, η_r and η_L are the transmittances of the imaging and illumination optics, respectively, $M \times N$ is the pixel count of the ICCD/ICMOS sensor, ρ is the target reflectance, A_r is the clear-aperture area of the receiving lens, and σ denotes the attenuation coefficient of the medium. Equation (19), commonly referred to as the lidar range equation for gated imaging, explicitly couples the characteristics of the laser pulse, medium propagation, target reflectance, optical throughput, and detector response in a single multiplicative framework.

Range-gated imaging system

After decades of development, 2D laser range-gated imaging has reached commercial maturity. Notable systems include the ARGC series from Obzerv (Canada) [125], the GLASS series by Sinotech Sensing (China) [126], and the SeaLVi platform developed by the Franco-German Saint-Louis Institute [127]. A key innovation is the UTOFIA project [128], which produced a compact water-related range-gated camera integrating a pulsed laser and a fast-gated CMOS sensor into a single unit. UTOFIA delivers both 2D video and 3D depth maps with operational ranges up to ~ 5 ALs, achieving 2–3 × range enhancement in turbid waters compared to conventional cameras, and centimeter-level depth accuracy within 5 m. Crucially, it is the first water-related range-gated system to adopt CMOS rather than ICCD technology, reducing cost and complexity while enabling higher frame rates.

In parallel, Wang et al. [128] developed a series of gated imaging prototypes, "Lvtong", "Fengyan" and "Longjing". Representative gated imaging system is shown in Fig. 10. These systems employ high-power 532 nm pulsed lasers and gated image intensifiers to enable long-range 3D imaging in coastal waters. Laboratory and field tests demonstrated their ability to detect targets beyond visibility limits and generate reliable 3D point clouds in turbid conditions. Primarily deployed for marine surveillance, these systems also exhibit robust performance under fog, rain, and snow [129]. Range-gated imaging's capability to deliver high-resolution reflectance and dense 3D data is accelerating its adoption in pilot applications such as security monitoring, ecological observation, and autonomous navigation, with several nearing practical deployment [130]. Representative systems are

Table 2 Representative range-gated imaging systems [129–134]

Manufacturer /Institute	System	Distance	Resolution	Primary application	Status
Obzerv Technologies	ARGC-2400	6.4 km in air	40 cm @ 6 km	Coastal/border long-range surveillance 808 nm laser, > 10 km imaging	Commercial
Sinotech Sensing	GLASS Series	Under the condition of 20 km range, the distance measurement to a target of 2.3 m × 2.3 m is ≥ 12 km	/	All-weather security monitoring NIR laser, gated ICCD	Commercial
BrightWay Vision	VISDOM	≤ 300 m in air	0.8–9 cm	Automotive night vision and ADAS 805 nm NIR laser diodes, gated CMOS	Commercial
Fr.-Ger. Inst. Saint-Louis	SeaLVi	/	cm level	Detection and ecological survey 532 nm laser, dual-gate 3D imaging	Research Prototype Sea trials
UTOFIA Consortium	UTOFIA Camera	Typical scanning distance: 1–9 m; Sea trials can observe up to 4.5–5 ALs; > 20 m visibility in clear water	/	Underwater inspection and mapping 532 nm laser, gated CMOS	Research Prototype
CAS Inst. of Semiconductors	Dragon Eye & others	/	mm—cm level	High-resolution 3D imaging 532 nm laser, gated ICCD	Research Prototype Sea trials

summarized in Table 2. Across scattering environments, range-gated imaging now spans mature atmospheric systems and rapidly advancing water-related variants, with clear modality, wavelength, and sensor trade-offs. In air, commercial NIR solutions achieve surveillance-grade standoff performance. Underwater, green gating leverages the blue-green transmission window to extend operation to several ALs, research prototypes such as SeaLVi, UTOFIA, and CAS "Dragon Eye" and related platforms deliver high-contrast reflectance and dense depth at short-to-medium ranges. ICCD detectors provide high gain for weak returns at the cost of size/power and blooming risk, whereas modern gated CMOS favors compactness, frame rate, and integration [131]. Ongoing work, polarization control to suppress backscatter, multi-gate fusion for SNR and depth linearity, and tighter laser-sensor synchronization, continues to raise performance ceilings.

Range-gated imaging has become a versatile tool for extending optical vision in scattering media. Operational atmospheric systems already deliver surveillance-grade imagery that passive sensors cannot match, while water-related variants, powered by improved lasers, modern sensors, and sophisticated algorithms, now provide high-contrast, high-resolution scenes at standoff ranges of several ALs. This capability is

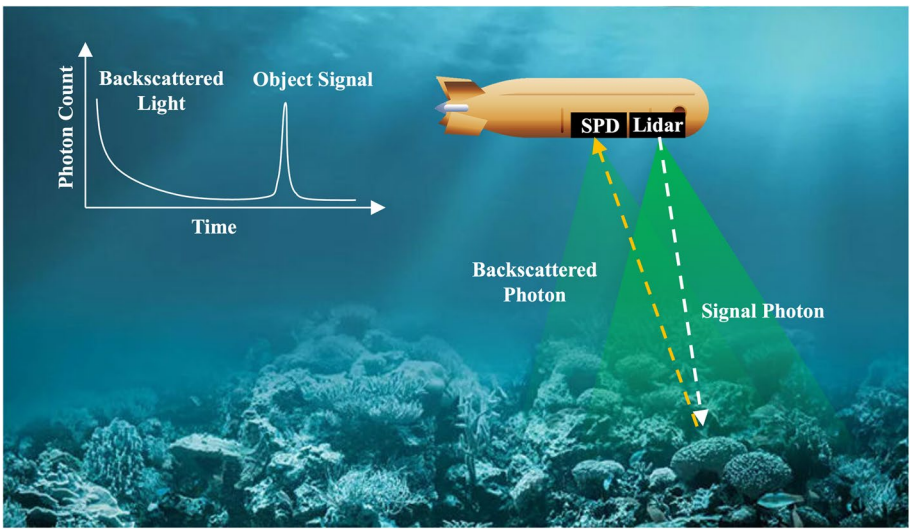

Fig. 11 Principal of single-photon imaging lidar

transforming oceanographic surveys, industrial inspections, and naval defense, enabling tasks such as object detection and 3D mapping in conditions where conventional cameras fail. Although challenges remain, ongoing work on polarization control and multi-gate data fusion continues to raise performance ceilings, positioning range-gated imaging as an indispensable technology for future water-related vision applications.

Single-photon imaging

Principle

Water-related single-photon imaging operates by detecting and time-tagging individual photons returned from a pulsed light source, thereby reconstructing range-resolved reflectivity profiles with subcentimeter accuracy even in highly scattering media. In this approach, the system emits ultra-short laser pulses and detects individual backscattered photons with single-photon avalanche diodes (SPAD) rather than integrating intensity over a gated exposure. Each emitted photon that survives absorption and multiple scattering is registered by a SPAD array or superconducting nanowire detector [135]. Time-correlated single-photon counting (TCSPC) based lidar offers picosecond-scale timing resolution for range measurement, translating to millimeter-scale depth precision in principle. Notably, this method was pioneered in early work on point-by-point single-photon ranging and demonstrated sub-centimeter accuracy using picosecond timing electronics. Unlike traditional laser line scanning (LLS) systems that rely on continuous-wave illumination and camera integration, a TCSPC lidar detects and time-tags each photon return. This per-photon time-stamping approach inherently gates against long-lasting backscatter and is highly photon-efficient, enabling operation at much lower laser power levels for a given range compared to analog or intensifier-based techniques. By utilizing single-photon detection, the need for high laser pulse energy and large apertures is significantly reduced [18, 136–139], enabling system miniaturization and making water-related deployment feasible [140–142].

Single-photon imaging lidar

Figure 11 illustrates a single-photon imaging lidar system. A single-photon imaging LiDAR emits ultrashort laser pulses into the scene and measures the time of arrival of individual backscattered photons relative to a synchronized clock, using Geiger-mode detectors such as SPAD arrays or superconducting nanowire single-photon detectors. For each pixel or scan position, the system accumulates a time-of-arrival histogram whose earliest, highest-confidence peak corresponds to the ballistic or minimally scattered return from the target surface. The peak time yields range via time-of-flight, while the peak area estimates reflectivity. Because detection is event-driven at the single-photon level, the method discriminates against delayed, multiply scattered background and operates with low pulse energies. It delivers range-resolved reflectivity with picosecond timing, yielding millimeter to centimeter-scale depth precision underwater, and extends imaging distance to roughly 10 ALs.

Consequently, single-photon imaging lidar has been proposed and successfully demonstrated for water-related imaging [143, 144]. The picosecond temporal resolution of modern SPAD arrays allows photon-efficient acquisition, often below one photon per pixel on average, so that high-contrast 3D imagery can be recovered at depths exceeding 100 m where conventional intensity imaging fails. Crucially, photon-by-photon statistics enable adaptive gating and quasi-Bayesian deconvolution, suppressing backscatter and enhancing the SNR in turbid water, thus extending the operational envelope of active optical sensing in oceanographic exploration, submerged archaeology, and autonomous vehicle navigation. However, water-related single-photon imaging lidar still faces technical challenges, including achieving efficient scanning to acquire underwater target information and mitigating interference from strong water column backscatter. To achieve fast imaging, detector arrays [143] or multibeam technology [145] are commonly employed. These require independent time-to-digital converters (TDCs) for each pixel, demanding high-performance computing for real-time processing [143]. To address this, multiplexing technologies like time-division multiplexing (TDM) [144–146], frequency-division multiplexing [147] and spectro-temporal encoding technology [148] have been proposed for simultaneous multi-pixel detection with a single-pixel detector. TDM scheme based on optical fiber arrays offers a notable advantage by enabling multi-pixel detection with a simple fiber array addition to a traditional lidar, greatly simplifying the architecture.

The lidar prototype (Fig. 12) comprises four subsystems, including a 532 nm pulsed laser, a transceiver, a TDM module and a data-acquisition unit. A fiber-coupled 532 nm source is selected because this wavelength lies in the blue-green optical window of water and benefits from mature, commercially available technology. The laser delivers picosecond/nanosecond pulses at MHz with user-selectable energies up to microjoule. On return, a large-aperture achromatic fiber collimator collects the signal through a band-pass filter. The lidar prototype was evaluated in a swimming-pool test tank at Xiamen University.

Recent breakthroughs in single-photon imaging lidar for water-related environments provide the cornerstone for centimeter-scale target detection by uniting photon-efficient optical ranging with complementary acoustic sensing in a tightly coupled, multi-modal framework. Table 3 summarizes the key parameters and performance metrics of representative water-related single-photon lidar systems in recent years.

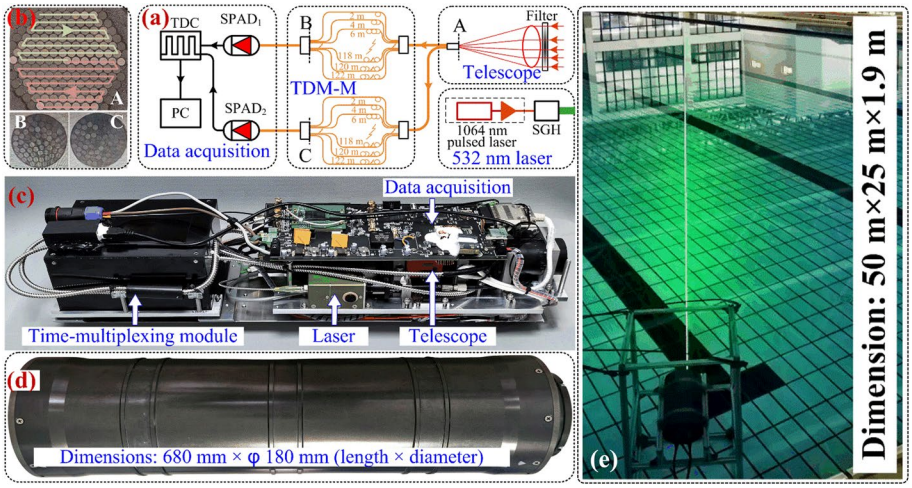

Fig. 12 **a** Schematic diagram of the water-related single-photon imaging lidar. **b** Enlarged cross-sectional images of the fiber interfaces at positions A, B, and C as marked in (**a**). **c** Internal view of the lidar. **d** External appearance of the lidar. **e** Photo of the lidar experiment in the pool

Fielded and near-fielded systems span airborne bathymetry in clear water and industrial subsea mapping, while laboratory and sea-trial prototypes demonstrate photon-efficient ranging over several ALs (up to ~ 8 to 10 AL) with decimeter-to-sub-millimeter vertical precision. Detector choices map to use cases: time-correlated SPADs enable sub-millimeter depth discrimination, SPAD arrays support real-time millimeter-scale 3D, Geiger-mode APDs offer rugged, wide-area coverage, and emerging SNSPD prototypes resolve centimeter-scale targets at short range. Blue-green operation and histogram-level inference suppress backscatter and recover depth at low photon counts, and tightly coupled optical–acoustic fusion improves coverage and robustness for AUV deployment. Remaining challenges include ambient-light resilience, backscatter/multipath rejection in highly turbid water, array calibration, and the latency–throughput balance for dense point clouds. Overall, the evidence indicates a transition from specialized prototypes to application-ready, photon-efficient, acoustically aided lidar capable of centimeter-scale detection and high-throughput 3D mapping across diverse marine conditions. This optical-acoustic fusion sharply elevates the situational awareness and autonomy of next-generation sub-sea platforms, most notably autonomous underwater vehicle (AUV) and thereby ushers in a new era of high-throughput, high-resolution marine surveying. The resulting gains in depth penetration, spatial coverage, and measurement fidelity are poised to accelerate fundamental oceanographic discovery, refine bathymetric and habitat mapping, and enable more responsible exploitation of marine resources, collectively heralding a transformative chapter in deep-sea exploration and sustainable blue-economy development.

Streak tube imaging

Principle

Streak tube imaging, a variant of LLS technology, synchronizes a collimated linear laser array with a receiver that has a narrow instantaneous field of view. It is characterized by picosecond-level temporal slicing, making it a powerful approach for high-precision

Table 3 Representative water-related single-photon lidar systems [140, 143, 149–153]

System	Institution	Depth range	Resolution	Detector
EAARL-B	NASA & USGS	~0–40 m in clear water	~0.3 m laser footprint ~2 m shot spacing ~0.2 m depth accuracy	SPAD
Underwater Single-Photon Bathymetric Lidar	Xiamen Univ	~0–54 m (10 AL) (lab)	Decimeter-scale vertical accuracy High point density	SPAD
Heriot-Watt Underwater Lidar Prototype	Heriot-Watt Univ. & Univ. of Edinburgh	up to 8 AL (lab)	Sub-millimeter depth resolution (TCSPC)	SPAD
Heriot-Watt Underwater Lidar Sensor	Heriot-Watt Univ. & Univ. of Edinburgh	~4 m in turbid water (lab)	Millimeter-level detail in real-time 3D images	SPAD array
3D at Depth Single-Photon Lidar	3D at Depth, Inc	~2–45 m underwater	~6 mm depth accuracy ~30° × 30° field of view	Geiger-mode APDs
Dual-Band SNSPD Lidar Prototype	KTH & Nanjing Univ	~0.5 m (lab)	Resolved cm-sized submerged objects	SPAD
System	Institution	Depth Range	Resolution	Detector
EAARL-B	NASA & USGS	~0–40 m in clear water	~0.3 m laser footprint ~2 m shot spacing ~0.2 m depth accuracy	SPAD
Shipborne Single-Photon Bathymetric Lidar	Xiamen Univ	~0–10 m (shallow coastal)	Decimeter-scale vertical accuracy High point density	SPAD
Heriot-Watt Underwater Lidar Prototype	Heriot-Watt Univ. & Univ. of Edinburgh	up to 8 AL (lab)	Sub-millimeter depth resolution (TCSPC)	SPAD
Heriot-Watt Underwater Lidar Sensor	Heriot-Watt Univ. & Univ. of Edinburgh	~4 m in turbid water (lab)	Millimeter-level detail in real-time 3D images	SPAD array
3D at Depth Single-Photon Lidar	3D at Depth, Inc	~2–45 m underwater	~6 mm depth accuracy ~30° × 30° field of view	Geiger-mode APDs
Dual-Band SNSPD Lidar Prototype	KTH & Nanjing Univ	~0.5 m (lab)	Resolved cm-sized submerged objects	SPAD

imaging in water-related environments. Such systems employ high-speed streak tubes and implement a spatial decoupling strategy that transforms imaging into efficient 1D scanning. By combining the ultrafast temporal resolution of the streak tube with the spatial line-scan capability of the laser, this technique enables accurate target reconstruction in scattering media. Its key strength lies in the streak tube's ability to convert photon arrival times directly into spatial positions, forming a natural distance-intensity mapping. The line laser contributes spatial information through sequential scanning, collectively boosting SNR in particle-laden water. Streak tube imaging systems also feature wide fields of view, high spatial resolution, and excellent sensitivity. However, the inherent one-dimensional nature of the streak tube restricts illumination options to linear scanning, posing challenges in practical deployment. These include light attenuation in complex water-related media, real-time processing constraints, and limits in photoelectric conversion efficiency [154, 155].

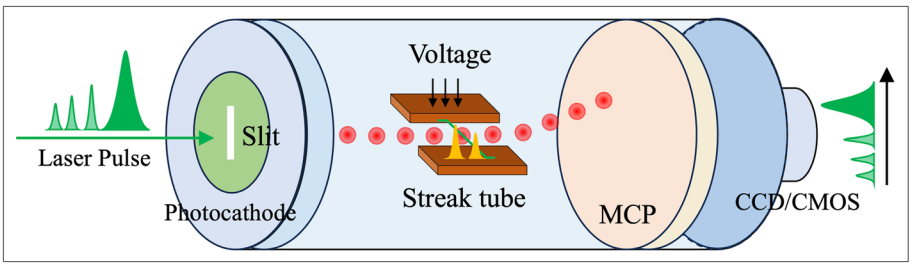

Fig. 13 Principle of streak camera

The streak tube itself comprises a photocathode, acceleration electrodes, deflection plates, a microchannel plate (MCP), and a phosphor screen, as illustrated in Fig. 13. Unlike conventional cameras that capture 2D spatial images, it maps light intensity as a function of time and wavelength. Incoming light passes through a slit to form a one-dimensional spatial profile, which hits the photocathode and emits electrons via the photoelectric effect. These electrons are accelerated and deflected by time-varying electric fields, spatially encoding their arrival time. The electrons then strike a phosphor screen, producing a streak image where time is mapped along the horizontal axis, and spatial or spectral information along the vertical. This image is finally captured by a CCD or CMOS sensor, achieving femtosecond-to-picosecond temporal resolution [156].

Streak tube imaging lidar (STIL)

Streak cameras have become a transformative tool in water-related STIL applications, offering robust solutions to challenges posed by scattering, absorption, and turbidity in water-related environments. Their capacity to simultaneously capture temporal and spatial information enables precise 3D imaging under low-visibility conditions. In 1988, S. Williamson first proposed a streak-tube-based laser radar, demonstrating that synchronizing a pulsed laser with a streak camera could yield accurate time-of-flight measurements while recording a one-dimensional intensity profile of the target [157]. Building upon this, F. K. Knight et al. [158, 159] introduced an angle-angle-range STIL system in 1989, where echo photons were mapped by the photocathode and, through fiber-optic reordering, produced a 16×16 pixel field with 4 cm depth resolution. With support from the U.S. Office of Naval Research, Areté Associates initiated the development of a high-resolution littoral-sensing STIL prototype in 1994. This system integrated streak tube imaging with flash lidar capabilities, advancing mine-countermeasure sensing. By 2003, it had been mounted on a towed water-related platform for 3D seabed imaging in the Gulf of Mexico. Using motorized scanning, it mapped spatial variations in seafloor morphology, including sand ripples, achieving a working range of ~ 3.4 m and 1 mm resolution, establishing its viability for detailed water-related target imaging [160, 161]. In parallel, Areté launched the Multiple-Slit STIL program to evaluate autonomous missile-borne target recognition. Phase-I trials yielded offline 3D range-intensity reconstructions of static targets [162]. Subsequent work by McLean et al. [163] validated centimeter-scale water-related 3D imaging, detailing system design and ocean-monitoring performance. Airborne MS-STIL experiments later confirmed the feasibility of autonomous seeker-based detection and

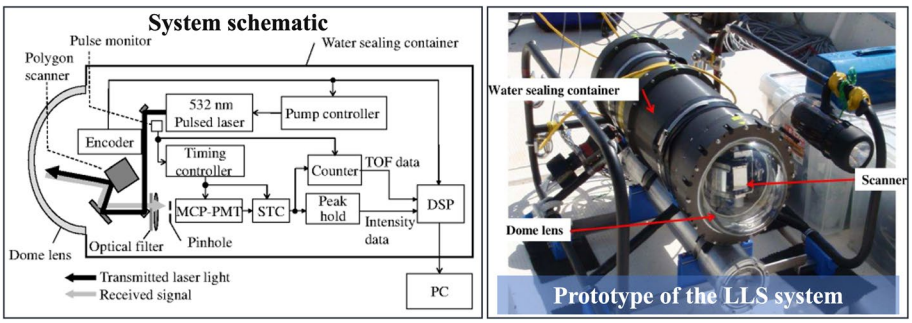

Fig. 14 Mitsubishi corporation's water-related 3D imaging system

classification [164]. A 2008 internal study further demonstrated the capability of STIL to capture the 3D morphology of short-scale sea-surface waves. Meanwhile, Mitsubishi Corporation developed a compact water-related topographic LLS system, utilizing a microchannel plate photomultiplier tube (MCP-PMT) for detection [165], as illustrated in Fig. 14.

Zhao et al. [166] at Xi'an Institute of Optics and Precision Mechanics (XIOPM) presented the first analytical design of a multi-slit STIL system, establishing trade-offs between time resolution and deflection sensitivity, and optimizing the electron-optical layout. In 2007, Harbin Institute of Technology enhanced spatial resolution by narrowing laser divergence, capturing 3D images of building façades at 700 m [167]. Within a linear systems framework, Lei et al. [168] analyzed STIL signal-to-noise characteristics, identifying detector-limited noise as the dominant constraint. Gao et al. [169] applied high-resolution single-slit STIL of ocean-surface capillary waves, serving anti-submarine applications. Ye et al. [170] developed a theoretical signal-distribution model for streak-array detectors, identified sources of ranging error, and proposed slot-width optimization combined with an iterative weighted-centroid algorithm to improve 3D imaging quality.

To further enhance depth precision, Chen et al. [171] addressed accuracy degradation under high-dynamic-range echoes by integrating streak-array detection with time-correlated single-photon counting. Luo et al. [172] applied Wiener deconvolution to reduce edge error and double spatial resolution from 9 mm to 4.5 mm. Li et al. [173] implemented a modulated sub-nanosecond laser in conjunction with a streak tube, achieving 9 mm depth resolution at 20 m underwater. Guo et al. [174] introduced a dual-mode multispectral-polarization STIL system, capturing depth, intensity, and polarization in a single or dual exposure, significantly improving contrast over single-wavelength systems.

To accelerate target recognition, Li et al. [175] combined ResNet classification with a beam-splitting fiber design that mitigates the trade-off between depth resolution and depth of field. Deep in-painting techniques with MS-STIL restored occluded regions, refining depth resolution from 0.4 to 0.1 m. Yan et al. [176] devised a hybrid k-nearest-neighbor and Gaussian-weighted voting framework to extract suburban buildings from airborne STIL datasets, effectively suppressing noise. Follow-up implementations confirmed that single-echo, single-source data suffices for rapid ground target extraction

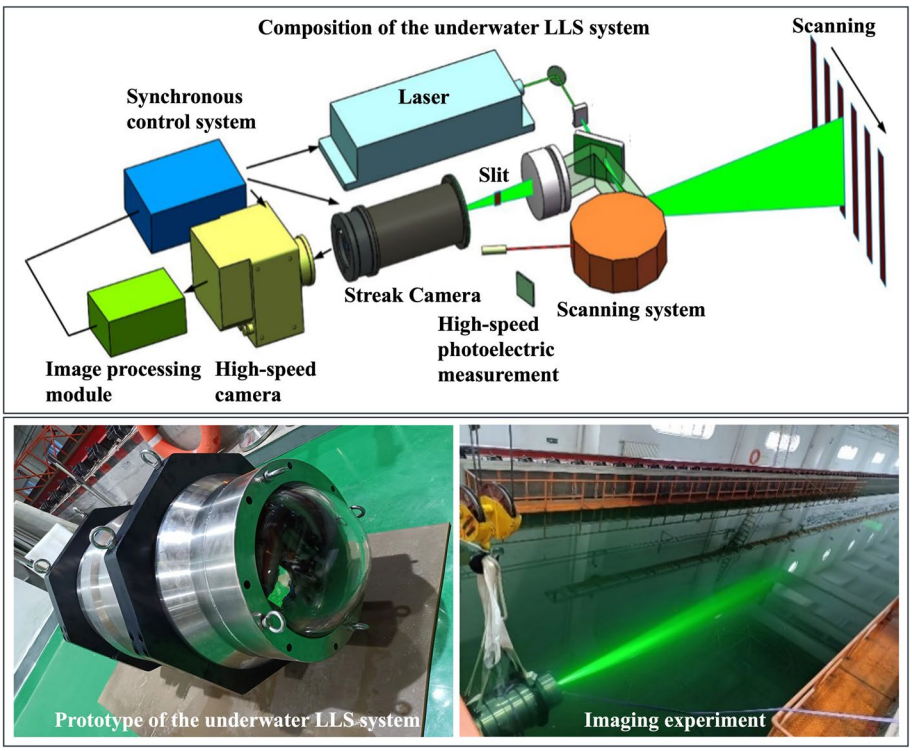

Fig. 15 The LLS system and imaging experiment

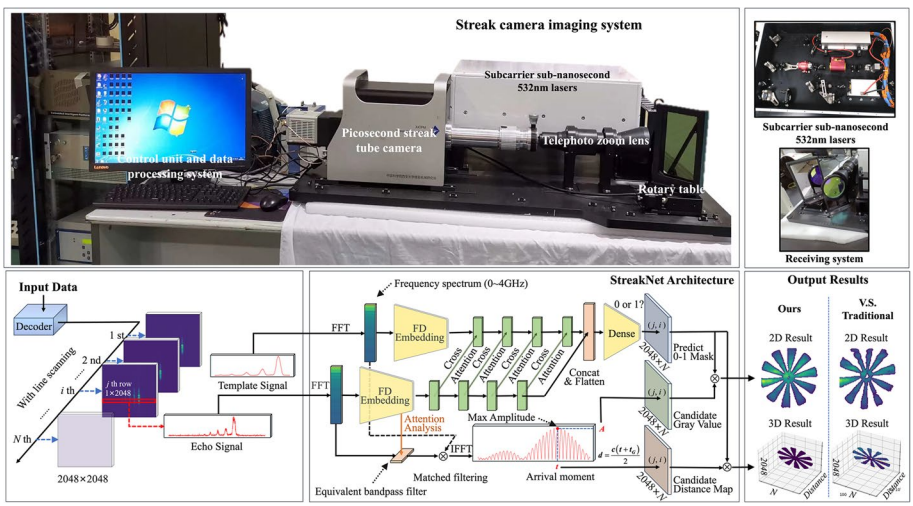

Fig. 16 Overview of the StreakNet-Arch based UCLR system

[177]. Fang et al. [178] introduced a STIL system achieving sub-centimeter resolution in both clear and turbid conditions, supported by an ADMM-based denoising and deblurring framework [179] that simultaneously suppresses noise, corrects blur, and enhances echo localization even under low SNR. Feng et al. [180–182] recently addressed frame-rate limitations in water-related LiDAR by combining LLS illumination with streak-camera reception. In 2024, their team developed China's first long-range,

Table 4 Representative water-related STIL systems [178, 184–187]

System	Institution	Depth range	Resolution	Device
High Frame-Rate STIL	Harbin Institute of Technology (HIT)	31 m	~3 mm lateral at 22 m (range res. ~1 cm)	Single-slit streak tube
Multi-Slit STIL	Beijing Institute of Technology (BIT)	~10 m	22 mm at 10 m	Multi-slit streak tube
Large-FOV STIL	XIOPM	20 m in clear water; 10 m in turbid water	<9 mm at 20 m range; range accuracy ~1 cm	Streak tube with 60 ps temporal resolution, 12 lp/mm spatial resolution
Few-Photon STIL	XIOPM	Weak-signal imaging in scattering media	~0.5 mm depth resolution	Streak tube enabling few-photon detection
PILLS/RAMMS Bathymetric STIL	Areté Associates & Fugro	~42 m (~3 × Secchi depth)	~1 m horizontal spot size	high-dynamic-range streak camera

deep-sea-capable LLS 3D imaging system in Fig. 15, achieving 27 frames per second or 6.48×10^6 points per second, while maintaining ≤ 5 cm resolution across a 34° field of view. The system operates at pressures equivalent to 6,000 m depth and reaches 5.2 ALs in seawater. Compared to existing systems, it achieves over 73 × the point density of Sweden's LSV-W at similar range, and surpasses Canada's 2G Robotics system in both depth rating and attenuation-limited range, establishing new benchmarks in deep-sea optical 3D imaging.

Li et al. [183] introduced StreakNet-Arch, an anti-scattering, end-to-end binary classification network for underwater carrier LiDAR-Radar (UCLR) systems in Fig. 16. The architecture embeds streak-tube imagery into a self-attention backbone with a novel double-branch cross-attention block, delivering real-time acquisition and superior scatter rejection. On an NVIDIA RTX 3060 GPU, StreakNet-Arch achieves a constant average imaging time (AIT) of 54 to 84 ms across up to 64 frames, whereas traditional methods' AIT grows linearly from 58 ms to 1,257 ms, confirming its real-time advantage. Finally, to validate deep-sea performance, we conducted a South China Sea trial, reaching an error of 46 mm for 3D target at 1,000 m depth and 20 m range.

Table 4 summarizes recent water-related STIL systems spanning laboratory prototypes to fielded bathymetric mappers. STIL combines the picosecond temporal precision of streak tubes with modern pulsed lasers to deliver centimeter-accurate depth and millimeter to centimeter lateral resolution over tens of meters underwater. In a streak tube, photons are converted at a photocathode, accelerated and deflected by tailored electric fields, and recorded on a position-sensitive anode, enabling sub-nanosecond timing and sub-millimeter spatial sampling. Advances in photocathode quantum efficiency, microchannel-plate gain/linearity, electron-optical design, and compact DPSS/fiber lasers have reduced temporal jitter, extended range, and lowered size-weight-power. Architectural choices trade throughput for detail: single-slit, high-frame-rate designs prioritize spatial fidelity and timing stability, whereas multi-slit geometries increase throughput at the cost of coarser lateral resolution. Large-FOV implementations achieve <9 mm lateral error at 20 m with ~1 cm range accuracy, and few-photon variants report ~0.5 mm depth

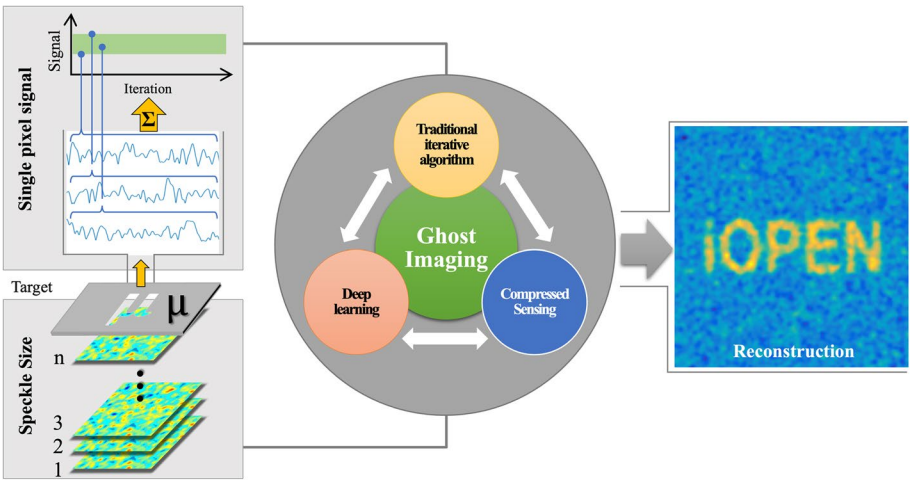

Fig. 17 Principle of computational GI

precision under weak returns. At the system level, high-dynamic-range airborne programs emphasize wide-area coverage and standoff operation, mapping to ~ 42 m depth with ~ 1 m spot size from crewed and UAV platforms. Persistent challenges include radiometric/timing calibration across slits, motion compensation under platform dynamics, suppression of backscatter and multipath in turbid water, and low-latency inversion for dense 3D products. With continued miniaturization, tighter integration with electro-optic and inertial sensors, and real-time learning-based reconstruction, STIL is poised to become a core element of next-generation multimodal marine sensing. Notably, all systems listed in Table 4 demonstrate effective operation in water-related environments and achieve better spatial resolution.

Ghost imaging

Principle

GI is an active imaging technique that leverages high-order statistical correlations within light fields. By concurrently recording one-dimensional intensity signals after light interacts with an object and capturing two-dimensional light field distributions, GI reconstructs images based on the correlations between these datasets. GI reconstructs scenes from second-order intensity correlations rather than direct irradiance maps, allowing high-fidelity images to be recovered even when fewer than one photon per pixel is detected, an essential advantage in the photon-starved hadal zone. Moreover, because the random speckle patterns used in GI are spatially incoherent with the diffuse backscatter field, uncorrelated veiling glare is statistically averaged out, yielding superior contrast in highly turbid water where conventional cameras saturate. This method transcends the traditional one-to-one mapping between objects and detectors inherent in conventional imaging systems, thereby offering superior resilience in ultra-low illumination and scattering environments [188–194], as shown in Fig. 17.

Early demonstrations of GI employed entangled photon pairs, yielding high SNR images and sparking significant interest in computational imaging. However, practical applications of quantum GI are hindered by challenges in generating entangled photons

at specific wavelengths and inherent photon flux limitations. To address these issues, researchers introduced GI schemes based on classical light sources. While this approach entails a reduction in SNR, it eliminates the reliance on entanglement. Subsequent efforts demonstrated GI using pseudo-thermal light sources. With the advancement of liquid crystal technology, micro-electro-mechanical systems, and high-speed digital control, spatial light modulators (SLMs) and digital micromirror devices (DMDs) have been widely adopted to generate pre-modulated optical fields, enabling single-arm correlation imaging, commonly referred to as computational GI (CGI). This technique evolved from the conventional two-arm configuration, which required a reference path to measure random light fields, into a simplified single-arm system based on known modulation patterns. Nevertheless, due to the intrinsic incoherence of pseudo-thermal light, the theoretical visibility of CGI is limited to 33% of that achieved by quantum GI. Furthermore, CGI typically requires a large number of single-pixel measurements, as each measurement provides only limited information about the object. By the way, there are some studies have tried to combine single-photon imaging technology with GI technology to further integrate the advantages of the two in underwater imaging [195]. Consequently, enhancing sampling efficiency and image contrast has become a central challenge in the field. These demands have driven the development of techniques such as compressed sensing and nonlinear correlation extraction, aiming to improve image quality while reducing the number of required measurements [188, 196, 197].

GI methods

a. Classical GI

   Classical GI algorithms reconstruct images by second-order intensity correlations between a known pattern sequence and bucket measurements. The baseline linear correlator forms the image from the covariance between the reference pattern and the bucket signal; Its variants, including Differential GI (DGI) [198] and normalized GI (NGI) [199], stabilize against illumination drift and suppress background by differencing or normalization of reference and bucket totals, improving SNR and robustness for pseudo-thermal and computational GI setups. These operations are the canonical classical baselines on which later methods build, and they remain attractive for their simplicity and physical interpretability. Yet they typically require many measurements because each bucket sample carries limited information, and their visibility/SNR are bounded under partially coherent illumination, which constrains performance in scattering media.

b. Compressive-sensing (CS) GI

   Motivated by the measurement burden of classical correlators, CS formulations of GI reconstruct the object under sparsity priors via convex optimization [200]. Total-variation regularization solved with augmented-Lagrangian schemes is a widely used choice for edge-preserving recovery at sub-Nyquist sampling [201]. Pioneering single-pixel/CGI work by Duarte et al. [202] and extensions to pseudo-thermal GI by Katz et al. [203] demonstrated that an image with N pixels can be recovered from far fewer than N measurements, thereby reducing sampling demands, improving noise

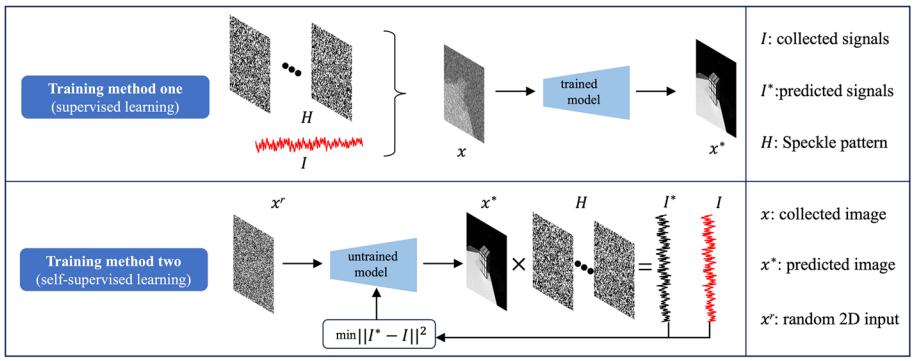

Fig. 18 Classification of CGI methods in DL

tolerance, and enhancing system flexibility. However, performance remains contingent on a faithful sparsity model and accurate forward operators; when the scene is not sufficiently sparse in the chosen transform or when noise/statistics deviate from assumptions (e.g., Poisson counts, speckle non-idealities), reconstruction quality degrades and the computational cost of large-scale optimization becomes nontrivial. These limitations helped catalyze DL for GI, while the explicit forward model and priors from CS continue to inform physics-guided learning that embeds measurement physics to improve robustness and interpretability [191, 204, 205].

c. DLGI

With the continuous advancement of DL, its powerful capabilities in feature extraction and nonlinear modeling have enabled significant improvements in image reconstruction quality. As a result, DL has been introduced into the field of CGI to achieve high-quality imaging. Depending on the training paradigm, DL-based CGI methods can be categorized into data-driven supervised approaches and physics-driven self-supervised approaches. The frameworks of DL-based CGI method under these two-training paradigm are illustrated in Fig. 18.

In recent years, data-driven supervised DL techniques have advanced rapidly, demonstrating outstanding performance in computer vision and related domains. These methods rely on large volumes of labeled training data to optimize a loss function, enabling models to learn complex mappings between inputs and outputs for accurate predictions on previously unseen data. Motivated by these successes, researchers have begun incorporating DL into GI [206–208]. Lyu et al. [209] first introduced DL into computational GI (GIDL). They employed traditional computational GI techniques to reconstruct a series of noisy, low-quality images under low sampling conditions, which were then paired with corresponding high-quality ground truth images to form a training dataset. Once trained, the deep neural network successfully mapped noisy reconstructions to high-fidelity outputs. Subsequently, He et al. [210] proposed a convolutional neural network (CNN) architecture tailored for computational GI. Both simulations and experimental results verified its effectiveness in significantly enhancing reconstruction quality at low sampling rates. Shimobaba et al. [211] also conducted additional experimental studies, further confirming the potential of DL in this field. Despite these advancements, data-driven supervised learning approaches typically require large amounts of labeled data, which is often need

high costs and time-consuming data preparation. Moreover, such models frequently exhibit limited generalization to novel or unseen scenarios, leading to suboptimal reconstruction performance.

Self-supervised learning enables models to autonomously learn deep and robust feature representations from large volumes of unlabeled data, thereby maintaining high reconstruction quality under varying imaging conditions and in previously unseen scenarios[212]. Owing to these advantages, self-supervised learning has been widely applied to CGI, effectively reducing the cost of training data acquisition while significantly enhancing the generalization capability of imaging systems in complex environments. Liu et al. [213] introduced a self-supervised DL framework into the field of CGI by integrating the physical model of GI with an untrained neural network. This method achieved high-quality image reconstruction without requiring any pre-training. The model takes the measured one-dimensional intensity sequence as input and predicts the corresponding reconstructed image. By using the experimentally collected intensity sequence as the supervisory signal, the network is optimized to ensure that the predicted intensity fluctuations match those of the actual object, thereby improving the fidelity of the reconstructed image. Extensive experiments [214–216] conducted in long-range outdoor scenarios validated the effectiveness and generalization ability of the self-supervised approach, further broadening the application scope of computational GI. However, existing DL-based GI methods still face underfitting issues when reconstructing images of complex objects. This is primarily due to limitations in model architecture and parameter capacity, which hinder the effective mapping between single-pixel measurements and intricate object features, ultimately reducing image visibility. Moreover, self-supervised algorithms solve a scene-specific inverse problem by alternating a physics-consistency step and a prior step. The per-frame cost grows with the number of iterations, the number of channels, and the number of pixels. In practice, tens to hundreds of iterations are common. Latency on edge hardware ranges from about 1/10 s to more than 1 s. That is acceptable for mapping or inspection at one to 5 Hz. It is not acceptable for closed-loop navigation, tracking, or manipulation at ten to thirty hertz. Feasibility improves with amortized inference or meta-learned initializers that reduce warm-start time. Unrolled optimization with learned proximal operators or learned denoisers fixes a small depth while keeping the physics. Multi-resolution pyramids and region-of-interest scheduling reduce work. Temporal warm starts and early stopping based on residual tests cut iterations. Mixed precision, quantization, fused operators, and kernel specialization raise throughput on vehicle processors. A hybrid pipeline is practical, with a light model online for control and a slower self-supervised module updating maps at a lower rate. Task-aware objectives and uncertainty-aware budgets further trim cost. Fast surrogates for the physics model, such as Fourier-based solvers or low-rank approximations, also help. These measures preserve the key benefit of self-supervision, label-free scene adaptation, while closing the compute gap that blocks real-time use.

In order to further improve the reconstruction ability of complex objects, the arrival of foundation-scale vision models, such as SDXL [217] and GPT-4 vision [218], has removed many of the parameter-count and architectural ceilings that once con-

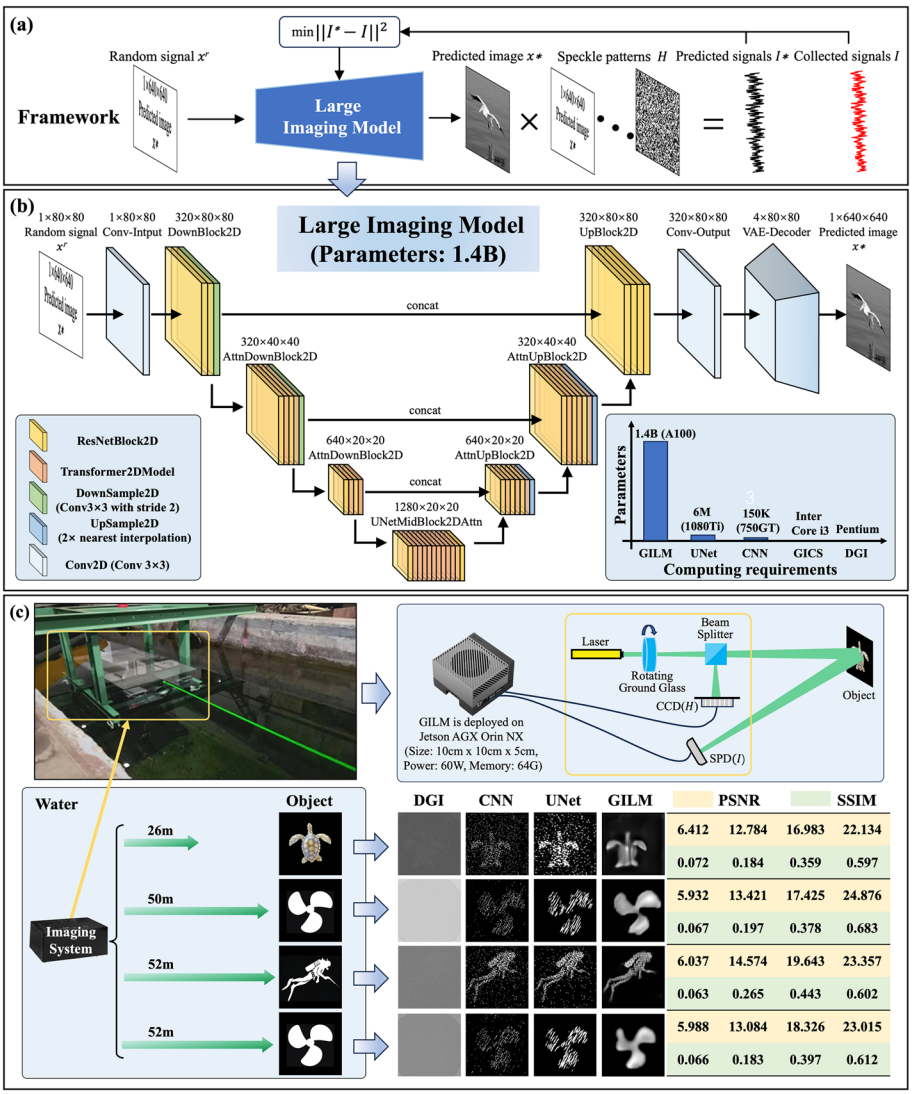

Fig. 19 Large model enhanced computational GI

strained conventional DL, allowing networks to reason over long-range dependencies throughout an entire feature sequence. This capability is especially valuable for GI, where the signal is both noisy and highly undersampled. Building on these insights, Chen et al. [219] introduce what is, to the best of our knowledge, the first large-scale imaging model tailored to GI, comprising 1.4 billion parameters and dubbed large model GI (GILM) in Fig. 19. Figure 19 (a) and (b) illustrates the principle of the GILM. GILM embeds a differentiable physical forward model of GI directly into its reconstruction pipeline, so that learning is guided not only by data supervision but also by the governing imaging physics. Deep skip connections span the full depth of the network to alleviate vanishing-/exploding-gradient issues, preserving high-frequency details while enabling the very large expressive capacity needed to model the subtle correlations hidden in single-pixel measurements. A multi-head self-attention block further captures global spatial dependencies, permitting the network to infer

object features even when local measurements are severely corrupted. Chen et al. benchmark GILM on a demanding water-related scenario in which reflective objects are positioned 52 m from the transmitter–receiver unit in Fig. 19 (c). Preliminary assessments suggest that, prior to quantization and compression, the model's computational requirements necessitate high-performance GPUs such as the NVIDIA A100 or Ascend 910B. Nevertheless, following quantization and compression, the model has been successfully deployed on a portable computing platform, the Jetson AGX Orin NX. Compared with state-of-the-art GI approaches, including compressive sensing, UNet-based reconstructions, and transformer baselines, GILM delivers substantial gains. It raises the peak SNR (PSNR) by up to 5.8 dB and halves the required sampling ratio. At the same time, it faithfully recovers fine structural details that competing techniques lose. The model's ability to track the temporal fluctuations of bucket signals under strong scattering proves essential to this performance gain.

To assess real-world deployability, Chen et al. ported the trained network to an edge computing device (NVIDIA Jetson AGX Orin). Thanks to mixed-precision quantization and kernel fusion, GILM achieves a 43 ms per-frame inference time, sufficient for live video at ~ 23 fps, without sacrificing accuracy, thereby validating its suitability for field deployments such as AUV/ROV. These results demonstrate that scaling DL models, when coupled tightly with the underlying physics of GI, offers a powerful path toward robust, noise-tolerant imaging in highly scattering environments.

d. AI-driven GI and AI-driven image restoration & enhancement

AI provides a common framework for both underwater image restoration/enhancement and AI-driven GI by casting them as physics-constrained inverse problems. In each case, the forward model of light transport through scattering media acts as a structural prior that guides learning. Restoration pipelines increasingly embed this physics via model-unfolding, plug-and-play denoisers, or self-supervised losses that enforce consistency between predicted clean images and the formation model of the observed data. AI-driven GI adopts the same paradigm but at the sensing stage. The structured illumination or speckle modulation, bucket detection, and correlation or compressive decoding, is made differentiable and integrated into the training loop, allowing networks to co-optimize reconstruction with illumination design or sampling policy. Across both areas, the trend is toward physics constrained AI that blends inductive priors with learned representations, leverages temporal coherence, quantifies uncertainty, and targets edge deployment through pruning, quantization, and unrolled architectures.

Key differences stem from where the intelligence is applied in the imaging chain and from the measurement geometry. AI restoration is post-capture and operates on full-frame measurements from conventional cameras. It aims to undo degradations while preserving real-time throughput and compatibility with existing payloads. Its dominant risks are model mismatch to water type and illumination, and generalization across scenes. AI-driven GI is an imaging modality. It actively controls illumination patterns and must reconstruct scenes from low-dimensional bucket signals. This yields strong resilience to scattering and high photon efficiency but introduces sampling latency, tight calibration of modulators and detectors, and

hardware-coupled failure modes. Restoration typically favors operational simplicity and higher frame rates, whereas AI-GI trades complexity for robustness and depth reach.

In summary, GI has progressed from entangled-photon demonstrations to practical classical and CGI using pseudo-thermal/SLM/DMD modulation that eliminates the reference arm via known patterns. While scalable, classical GI incurs a lower theoretical visibility (≈33%) and heavy sampling demand, motivating compressed-sensing reconstructions that reduce measurements but degrade when object sparsity is weak. DL now underpins two complementary tracks: data-driven supervised models that markedly improve low-sample reconstructions yet require costly labels and generalize poorly, and physics-driven self-supervised frameworks that embed the GI forward model to fit measured bucket sequences, delivering label-free robustness in challenging, long-range scenes. Foundation-scale, physics-integrated architectures further raise PSNR, halve sampling ratios, and reach real-time edge inference, enabling field deployment. Emerging trends include fusion with single-photon detection and acoustic sensing for underwater operation. Key open issues span backscatter/multipath suppression, underfitting for complex targets, and rigorous radiometric/temporal calibration to ensure photon-efficient, reliable imaging in turbid environments. In future, Field-ready GI payloads remain limited by motion-induced speckle decorrelation during AUV/ROV drift or surge, which degrades correlation fidelity. They also experience SLM calibration drift under ~ 110 MPa hydrostatic pressure and 2 to 4 °C thermal gradients, necessitating periodic in situ self-referencing on extended missions.

Spectral imaging

Principle

Conventional cameras that record only red, green, and blue (RGB) channels frequently generate bluish, low-contrast imagery [220, 221]. This degradation arises from two coupled phenomena [222–224]. First, there is rapid, depth-dependent absorption of longer wavelengths, particularly red light. Second, multiple scattering by suspended particulates further attenuates direct light and obscures scene details. Water-related spectral imaging circumvents these limitations by sampling the full optical spectrum at every pixel, thereby enabling pixel-wise reconstruction of the scene's spectral reflectance [225, 226]. Spectral imaging measures spatially resolved spectra to form a 3D data cube, enabling material discrimination from the wavelength dependence of reflectance and emission. In passive systems, the scene's spectral radiance is imaged and spectrally separated by a dispersive or filtering element, so that each pixel is associated with a narrow spectral response. Active variants illuminate with controlled spectra or narrowband laser lines and record the returned spectrum. Radiometric calibration maps raw digital counts to spectral radiance via flat-fielding and instrument response, while spectral calibration ties detector pixels to wavelength and corrects instrument line shape, smile/keystone, and stray light. Calibrated radiance is converted to apparent reflectance by normalizing the incident irradiance and correcting water-column path radiance and transmittance to counter wavelength-dependent absorption and scattering.

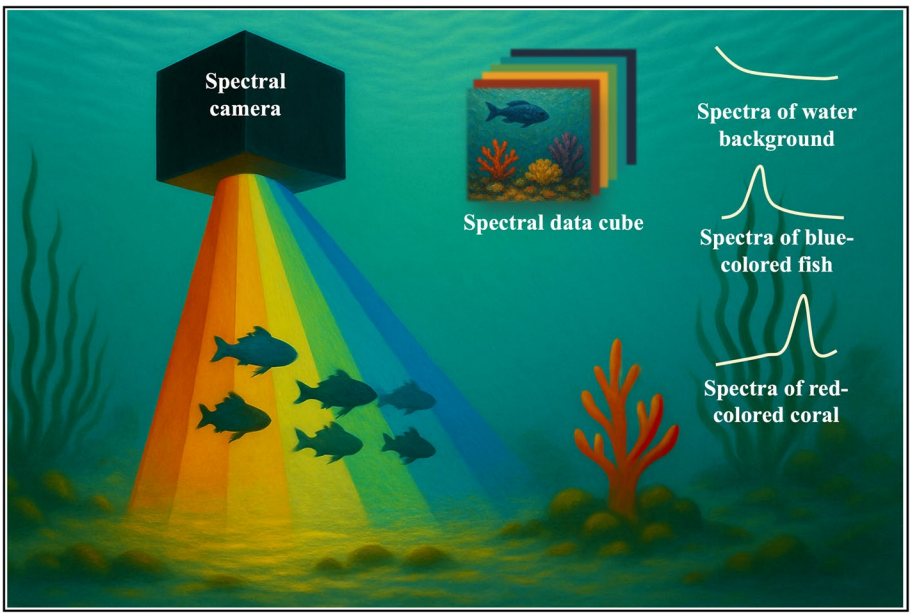

Fig. 20 Schematic diagram of water-related spectral imaging technology

Subsequent analysis exploits the high spectral resolution and contiguous bands to separate materials with similar colors but distinct spectra, yielding quantitative maps of composition and condition that exceed the capabilities of broadband RGB imaging. As illustrated in Fig. 20, the resulting data cubes provide an additional, information-rich dimension of observation, exposing subtle inter-object differences that remain invisible to the naked eye or to conventional RGB sensors.

Recent advances in compact image sensors, miniaturized dispersive optics, and pressure-tolerant housings have markedly reduced the size, weight, and power budget of spectral imagers, accelerating their deployment in the marine environment. At the same time, demand for higher-fidelity visual tools has surged across disciplines such as marine ecology, archaeology, and ocean conservation. Current use cases span coral-reef health assessment, benthic habitat mapping, shipwreck documentation, and the detection of ecological change or deep-sea megafauna [227–232]. Central to these applications is the concept of optical "fingerprinting," whereby each material is distinguished by its unique spectral signature even when shape, color, or texture cues are degraded or ambiguous.

Spectral imaging method

Water-related spectral imaging currently embraces two primary modalities. Multispectral systems acquire a limited set of discrete wavelength bands, selected with optical filters, filter wheels, or bandpass-segmented cameras, yielding compact, cost-effective solutions that are amenable to real-time or resource-constrained missions [233, 234]. Hyperspectral imaging (HSI), in contrast, records tens to hundreds of contiguous narrow bands, producing a 3D (x, y, λ) data cube that supports fine-grained material discrimination, precise water-column correction, and detailed extraction of environmental features [230–235].

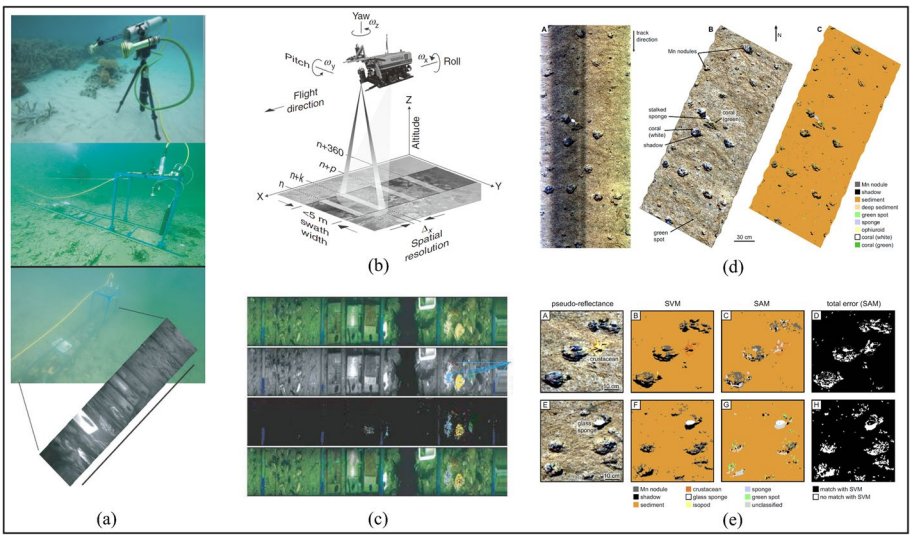

Fig. 21 UHI underwater spectral camera. **a** The prototype of UHI and set up of an UHI prototype seafloor mapping system. **b** UHI deployed on ROV equipped with artificial light sources for illumination. **c** Identification and area coverage of different biogeochemical objects based on specific optical fingerprints. **d**, **e** Pseudo-RGB and classification image of manganese nodules and a stalked sponge

Water-related spectral imaging first emerged in the late twentieth century, but its early adoption was hampered by limited detector sensitivity and poor in-water illumination. Initial efforts therefore concentrated on multispectral approaches. In 2002, Zawada introduced one of the earliest examples, the low-light-level underwater multispectral imager (LUMIS), which recorded four narrow bands centered at approximately 460, 522, 582, and 678 nm without beam splitters, enabling the documentation of natural fluorescence in marine organisms to depths of 20 m [236]. Building on this concept, Gleason et al. [237] developed a six-band multispectral camera (MSCAM) that employed a mechanical filter wheel to acquire sequential exposures; despite the multi-shot acquisition, its staring-mode design furnished high spatial resolution suitable for diver-operated coral-reef surveys. Wu et al. [238] subsequently introduced the Underwater Multispectral Imaging System (UMIS), a dual-filter-wheel apparatus capable of acquiring 31 spectral bands across the 400–700 nm range with approximately 10 nm resolution. Encased in a pressure-tight housing, the system supports deployment via remotely operated vehicle (ROV) or manual operation by divers. Its design enables targeted applications in coastal and archaeological investigations, ensuring robustness in water-related environments. More recently, Liu et al. [239] introduced TuLUMIS, a tunable, LED-based imager that illuminates scenes with 16 LEDs across eight discrete wavelengths, thereby reducing mechanical complexity by modulating the illumination rather than filtering the detected light. Collectively, these systems established the foundational architecture for modern water-related spectral imaging and underscored its superiority over conventional RGB observation.

By the early 2010s, gains in detector quantum efficiency, onboard processing, and storage made hyperspectral imaging (HSI), the capture of tens to hundreds of contiguous narrow bands, feasible underwater. The dominant push-broom architecture disperses slit light spectrally while vehicle motion (ROV/AUV) sweeps

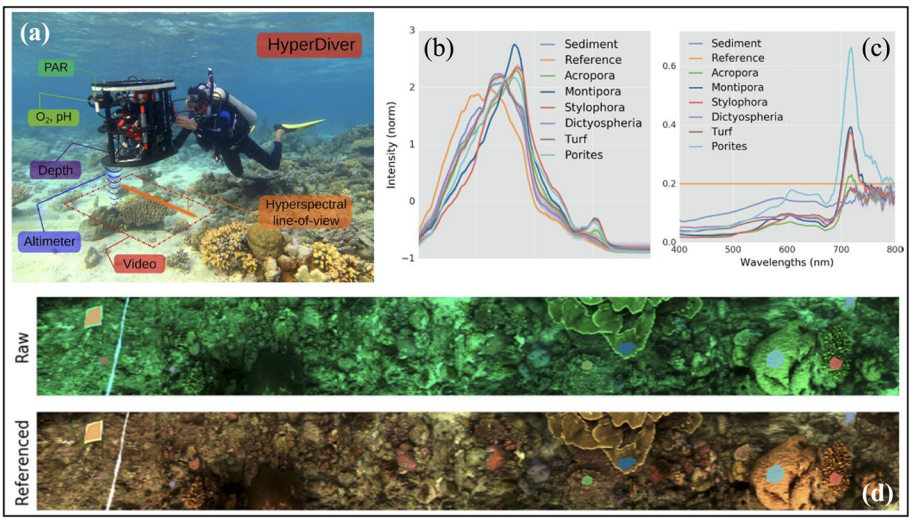

Fig. 22 HyperDiver underwater hyperspectral imager. **a** HyperDiver system operated by a diver to survey a shallow coral reef. **b**, **c** Intensity and reflectance of specific benthic targets. (d) Three-channel color image derived from the hyperspectral data

successive lines to assemble an (x, y, λ) cube. NTNU's 2009 patent established the first operational underwater system [240]. Diver-towed prototypes soon demonstrated shallow-water spectral mapping [241], leading to Ecotone A/S's commercial underwater hyperspectral imager (UHI) [242]. The UHI Ocean Vision (380 to 750 nm, $\approx$ 2.2 nm resolution, 150 to 200 bands, 60° FOV, 6000 m rating) now supports missions from millimeter-scale coral surveys at 80 m to manganese-nodule mapping at 4200 m and hydrothermal-vent or massive-sulfide reconnaissance on landers and AUVs [230]. Operating ~ 2 m above the seabed, it delivers sub-centimeter pixels and reliably discriminates substrates, biota, and geological resources, as shown in Fig. 21.

From the mid-2010s onward, water-related spectral imagers rapidly diversified, spanning miniature scanners, low-cost modular units, and diver-carried rigs. A prime example is HyperDiver, a push-broom hyperspectral system introduced in 2017 by Chennu et al. [243], as shown in Fig. 22. Centered on a Resonon Pika II camera and augmented with attitude, illumination, and water-quality sensors, HyperDiver logs hyperspectral cubes alongside RGB, depth, irradiance, and GPS data, allowing automated 3D benthic mapping while surveying roughly 15 to 30 m^2/min on shallow reefs.

Parallel efforts in cost-reduction have demonstrated that hyperspectral sensing can be both effective and affordable. Nevala et al. [244] constructed a low-cost system using off-the-shelf components, a rotating-mirror scanner, miniature spectrometer, and consumer-grade sensor, which successfully produced credible water-related spectral maps. Simultaneously, "internal-scan" architectures, wherein lenses or mirrors move within a sealed housing, eliminated the need for external motion, making them ideal for AUVs or stationary observatories with strict navigational constraints. Snapshot hyperspectral cameras have expanded into water-related applications, capturing full (x, y, λ) data cubes in a single exposure via optical multiplexing. For example, Cubert's FireflEYE V185 encodes 50×50 spectral images

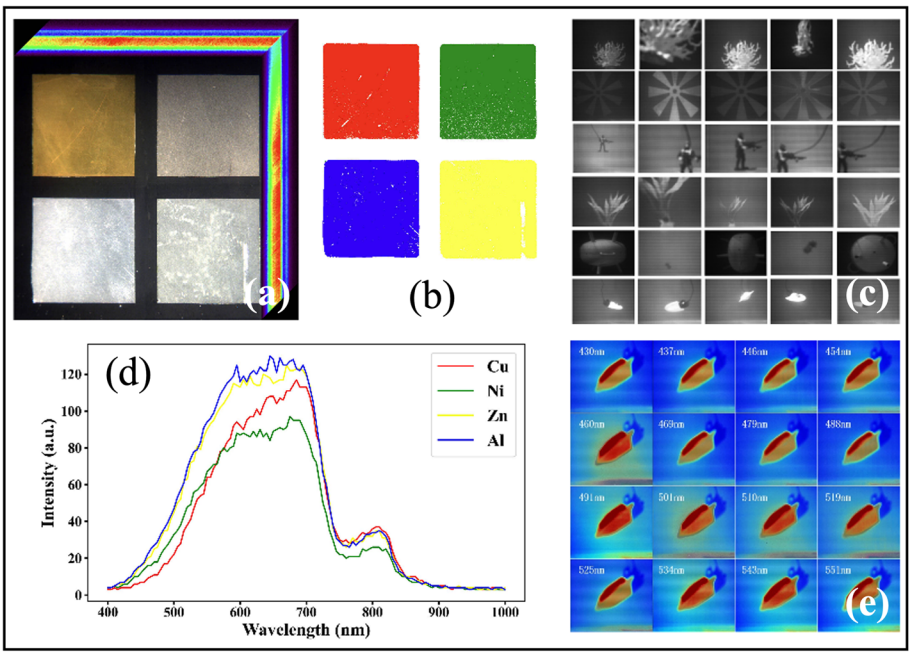

Fig. 23 Representative data obtained using the USIS-1 and USIS-2 systems (**a**) Three-channel composite image reconstructed from hyperspectral data acquired by USIS-1. **b** Spectral curves of selected objects captured by USIS-1. **c** Classification results of USIS-1 (**d**) Single-band image of the moving targets captured by USIS-2. **e** Sixteen feature maps of different bands derived from USIS-2multispectral data

into a 1000 × 1000 panchromatic frame at up to 15 cubes per second. Rated to 60 m depth, it suits diver and shallow ROV use, though it sacrifices spatial resolution and optical throughput. The 2020 s have seen a trend toward more compact, intelligent, and versatile instruments. Bai et al. introduced a dual-mode scanner with an internally actuated objective lens, enabling both fixed and mobile operation with high-fidelity classification [245]. Xue et al. [246] developed a compact prism-grating-prism system that combines high spectral resolution with mechanical robustness. Song et al. [247] proposed a six-channel staring camera using k-nearest-neighbor spectral reconstruction, offering a balance between optical simplicity and spectral fidelity. Most recently, the XIOPM unveiled the underwater spectral imaging system (USIS). USIS-1 is a push-broom hyperspectral sensor (360 to 1000 nm, 128 bands, 5 nm interval) featuring internal mechanical scanning to decouple acquisition from vehicle motion, facilitating deployment on AUVs and fixed platforms. USIS-2, a snapshot multispectral variant (32 bands), captures data cubes instantaneously, mitigating motion blur and excelling at transient event capture, such as fast-moving fauna or dynamic plumes. Both systems eliminate external moving parts, enhancing reliability in turbid or high-flow environments. Representative results are shown in Fig. 23.

Table 5 summarizes the key parameters of the water-related spectral imaging systems discussed in this section. Water-related spectral imaging is coalescing around two complementary design lines, high-fidelity push-broom hyperspectral scanners and agile snapshot spectral imagers, each tuned to the constraints of underwater light transport and mobile platforms. Push-broom systems such as UHI Ocean Vision

Table 5 Representative water-related spectral imaging systems [236–245]

System	Institution	Imaging mode	Spectral range	Bands	Spectral resolution
LUMIS	University of California San Diego	Multispectral snapshot	460, 522, 582, 678 nm	4	/
MSCAM	University of Miami	Multispectral Staring	400–700 nm	6	/
UMSI	Zhejiang University	Multispectral Staring	400–700 nm	31	10 nm
TuLUMIS	Zhejiang University	Multispectral	400–700 nm	8	/
UHI Ocean Vision	Norwegian University of Science and Technology	Hyperspectral push-broom	380–750 nm	150–200	2.2–5.5 nm
HyperDiver	Max Planck Institute for Marine Microbiology	Hyperspectral push-broom	400–900 nm	480	1.5 nm
Cubert UHD	Cubert GmbH	Hyperspectral snapshot	450–950 nm	125	8 nm
USIS-1	XIOPM	Hyperspectral push-broom	360–1000 nm	128	5 nm
USIS-2		Multispectral snapshot	360–1000 nm	32	/

and USIS-1 maximize spectral resolving power and band count for detailed material discrimination, but require controlled platform motion and stable illumination. At the extreme of spectral granularity, HyperDiver exemplifies laboratory/field mapping with fine chemotaxonomic sensitivity, trading scan logistics and data volume for accuracy. In contrast, snapshot architectures prioritize scene dynamics and platform agility, while USIS-2, LUMIS, MSCAM, UMSI, and TuLUMIS illustrate multispectral designs that reduce size–weight–power and ease real-time deployment on AUV/ROV. Overall trends favor broader spectral envelopes with emphasis on the blue-green window for penetration, on-board calibration for radiometric/spectral drift, and tight coupling to navigation and learning-based analytics for adaptive surveys.

Collectively, these next-generation systems support agile, high-resolution hyperspectral mapping for mobile AUVs and intelligent robotic platforms. The ongoing shift toward mobility, real-time processing, and adaptive mission execution reflects a broader trend in underwater sensing. With continued progress in sensor miniaturization, energy efficiency, and pressure-resistant design, future hyperspectral systems are poised to operate deeper, longer, and with increasing autonomy.

FOD imaging

Deep-sea submersibles

a. Overview of the deep-sea submersibles

Deep-sea technology is widely recognized as a hallmark of a nation's comprehensive strength. Achieving independent mastery of deep-sea submersible technology significantly enhances a country's capabilities in resource exploration, maintenance of water-related military infrastructure, and maritime rescue operations. As early as the twentieth century, countries such as the United States, Russia, and

France had already developed manned deep-diving technologies capable of reaching depths between 4,500 and 6,500 m [248]. The successful development of the Jiaolong manned submersible in the early twenty-first century marked a major milestone in China's advancement in deep-sea exploration [249]. Ocean exploration plays a vital role in expanding humanity's understanding of the Earth, and submersibles, being the cornerstone of marine research, are not only indispensable tools for addressing resource challenges and conducting scientific investigations, but also a strategic asset in strengthening national maritime capabilities.

Submersibles, or underwater vehicles (UVs), can be classified based on various criteria, including manning method, power source, and operational mode. Different types of submersibles are suited to distinct applications such as deep-sea exploration, resource extraction, and military reconnaissance. Based on the manning method, submersibles are generally categorized into manned submersibles, also known as human-occupied vehicles (HOVs), and unmanned submersibles, or unmanned underwater vehicles (UUVs) [250]. This section provides a detailed review of submersibles following this classification. Based on their power systems, submersibles can be classified into electric, hydraulic, and nuclear-powered types [251]. Electric submersibles typically use lithium or silver-zinc batteries, offering clean and low-noise operation. However, their limited energy capacity restricts them to short-duration scientific missions [252]. Hydraulic submersibles, powered by hydraulic systems, provide greater power output, making them well-suited for tasks involving robotic arms on ROVs and for deep-sea engineering maintenance [253]. Nuclear-powered submersibles, which are still under development [254], rely on compact nuclear reactors and offer exceptionally long operational endurance, potentially lasting several years. Despite their promise for long-term monitoring and military applications, they also pose significant safety and regulatory challenges. Based on operating depth, submersibles can be categorized into three types: shallow-water (less than 300 m), medium-deep (300 to 6,000 m), and FOD (deeper than 6,000 m). Shallow-water submersibles, such as commercial ROVs, are typically used in offshore engineering, recreational diving, and other nearshore applications [255]. Medium-depth submersibles, such as Alvin [256], are widely employed in marine scientific research. FOD submersibles, such as the Struggler [51], are designed for abyssal exploration, deep-sea resource surveys, and other extreme environments. Surface and shallow-water submersibles generally involve lower technical complexity and prioritize cost-effectiveness and operational practicality. In contrast, medium-deep and FOD submersibles require advanced high-strength materials and intelligent technologies, serving as key indicators of a nation's comprehensive scientific and technological capabilities. Although FOD operations have now become technically feasible, challenges remain in enhancing the endurance and real-time control of unmanned submersibles operating below 6,000 m.

b. HOV

Based on operational depth, manned submersibles can be classified into three categories, including shallow-water, deep-sea, and FOD types. Shallow-water submersibles (operating at depths of less than 1,000 m) typically feature a relatively

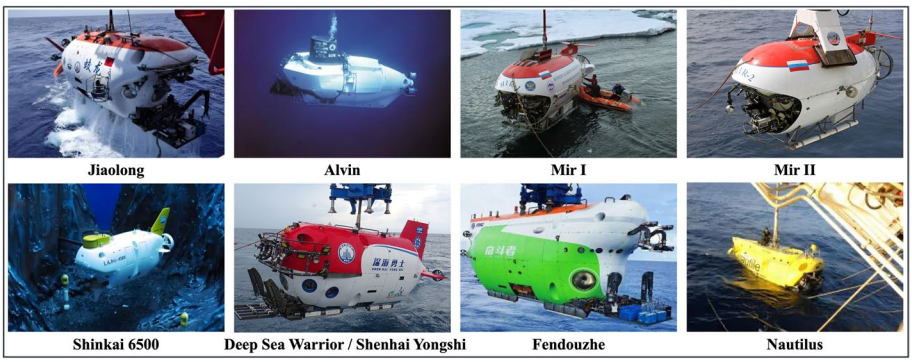

Fig. 24 Representative deep-sea HOVs

Table 6 Comparison of structure parameters and equipment performance of HOVs [257–262]

Submersible	Max depth (m)	Crew capacity	Dive duration (h)	Key features
Trieste I (Italy/US)	10,916	2	/	Record-breaking depth
Alvin (US)	6500	3	8–10	High-res imaging and sonar
Shinkai 6500 (Japan)	6527	3	8	High operability; > 1300 dives
MIR-1/2 (Russia)	6000	3	17–20	High endurance; high operability
Nautile (France)	6000	3	8–10	Lightweight; multi-dimensional tasks
Jiaolong (China)	7062	3	10–12	Deep-sea research in multiple trenches
Shenhai Yongshi (China)	4500	3	6–8	Indigenous deep-sea tech; reduced cost
Fendouzhe (China)	10,909	3	10–12	96.5% localization

simple structural design with lower pressure-resistance requirements and high maneuverability. They are well-suited for short-duration missions such as early-stage test dives, tourism, basic scientific research, and rescue training. Representative examples include early prototypes of China's Jiaolong, as well as sightseeing submersibles operating in the Maldives and Hawaii [257]. Deep-sea submersibles (operating at depths between 1,000 and 6,000 m) require robust pressure-resistant structures and are typically equipped with high-precision sensors and robotic manipulators to support extended underwater operations. Notable examples include China's Jiaolong (maximum depth: 7,062 m) [258], the United States' Alvin (maximum depth: 6,500 m) [259], and Japan's Shinkai 6500 (maximum depth: 6,527 m) [260]. These vehicles are widely used for deep-sea biological surveys, geological investigations, and resource exploration. FOD submersibles (operating beyond 6,000 m) are engineered with advanced pressure-resistant technologies, often including titanium-alloy spherical cabins, and equipped with high-definition imaging systems and high-speed communication capabilities. Prominent examples include China's Fendouzhe (maximum depth: 10,909 m) [261] and the U.S. Trieste, which famously completed the first crewed dive to the bottom of the Mariana Trench (10,916 m) [262]. Fendouzhe represents a milestone in Chinese submersible

Fig. 25 Representative deep-sea ROVs

Table 7 Comparison of structure parameters and equipment performance of ROVs [269–276]

Type	Max depth (m)	Dive duration (h)	Key features	Representative applications
MROV	< 100	1–3	Lightweight (< 15 kg), fully electric, easy to deploy	Tank inspection, aquaculture monitoring
EROV	< 300	2–6	Onboard camera and lighting, basic maneuverability	Diver support, hazardous inspection
IROV	Up to 1,000	4–8	Cost-effective, modular, increasingly electric powered	Offshore wind, infrastructure monitoring, environmental surveys
ROTV	Varies (Towed)	Continuous (towed)	High-resolution sonar, towed operation	Cable/pipeline survey, military detection
WROV	3,000–6,000	8–12	Dual hydraulic manipulators, high lifting capacity	Oil/gas intervention, salvage, construction
TROV	1,000–4,000	6–24	Crawler-based mobility, seabed contact, long-duration endurance	Deep-sea mining, polar exploration, cable laying
Plough	Up to 6,000	6–12	Integrated trenching systems, large and heavy	Pipeline burial, subsea trenching, environmental mitigation

engineering, reaching 10,909 m and achieving a 96.5% localization rate of core components, integrated with high-resolution imaging, autonomous navigation, and FOD operational capabilities. Figure 24 shows the representative deep-sea HOVs.

Table 6 presents a comparative overview of representative deep-sea HOVs. These submersibles are essential for probing the deepest parts of the ocean and conducting research on extreme marine environments, including deep biospheres and abyssal geology. Looking ahead, international competition in HOV development is expected to concentrate on innovations in energy efficiency, advanced pressure-tolerant materials, and commercial applications, signaling a new era of human presence and activity in the deep-sea.

c. ROV

ROVs are tethered unmanned underwater systems widely employed in deep-sea research, subsea engineering, and defense. Enabled by umbilical cables, ROVs offer real-time control with continuous power and data transmission, allowing for low-latency maneuvering and high-precision task execution. Key features include robust stability under hydrodynamic stress and the capacity to carry modular payloads such as manipulators, sonar systems, and sampling devices. Representative platforms

include Seahorse, Sea Dou, Nereus, and Odyssey [263–267]. Douglas-Westwood further classifies ROVs into seven functional types [268]. Miniature ROVs (MROVs) [269], compact and fully electric, are suited for confined-space inspection. Eyeball ROVs (EROVs) [270] offer basic imaging capabilities for diver support. Inspection ROVs (IROVs) [271] provide mid-range performance for infrastructure monitoring, increasingly shifting from hydraulic to electric propulsion [272]. Remotely Operated Towed Vehicles (ROTVs) [273] conduct wide-area seabed surveys using towed sonar arrays. Work-Class ROVs (WROVs) [274], equipped with hydraulic manipulators, enable intervention tasks at depths up to 6,000 m. Tracked ROVs (TROVs) [275] employ crawler systems for long-duration seabed operations, while Excavation ROVs (Ploughs) [276] integrate trenching tools for pipeline burial and environmental mitigation. Figure 25 shows the representative deep-sea ROVs.

Table 7 presents a comparative overview of representative deep-sea ROVs. This typology reflects the evolving spectrum of ROV applications, from lightweight visual inspection to heavy-duty subsea operations. Current trends emphasize increased autonomy, localization, and intelligent control in work-class systems, while micro and observation-class ROVs are gaining momentum in environmental monitoring and scientific research due to their affordability and deployment flexibility [268].

d. AUV

AUVs are untethered submersible platforms designed to perform complex underwater missions autonomously, without the need for surface-vessel control. Unlike ROVs, AUVs are powered by onboard energy storage systems and utilize pre-programmed or adaptive control algorithms for navigation, sensing, and task execution. Core advantages of AUVs include their fully autonomous operation [277], onboard decision-making capability [278], extended endurance, and adaptability for large-area, long-duration missions [279]. These characteristics make them ideal for applications in oceanography, seabed mapping, infrastructure inspection, and deep-sea exploration.

AUVs are generally classified based on operational depth and propulsion mechanisms. Depth-based categories include shallow-water AUVs, commonly used in nearshore surveys and pipeline monitoring [280, 281]. Deep-water AUVs, such as the Qianlong series, which are used for bathymetric mapping and mineral prospecting [282], and FOD AUVs exemplified by Wukong, developed for missions in the Mariana Trench and other hadal zones [283]. From a propulsion perspective, electric AUVs, such as Bluefin-12, are powered by lithium-ion batteries and represent the most prevalent configuration[284, 285]. Fuel-cell AUVs, including Japan's URASHIMA, leverage hydrogen fuel cells to significantly increase range and endurance [286]. Hybrid AUVs, such as China's Haiyan-X, combine buoyancy-driven gliding and propeller propulsion to optimize energy use and maneuverability across mission profiles [287].

Underwater Gliders (UGs) represent a specialized subclass of AUVs that achieve horizontal propulsion through periodic buoyancy changes and hydrodynamic lift. Distinguished by their exceptional energy efficiency, gliders are designed for long-duration missions across vast ocean regions [288]. Depending on their propulsion method, gliders are categorized into traditional gliders (e.g., Slocum), which use

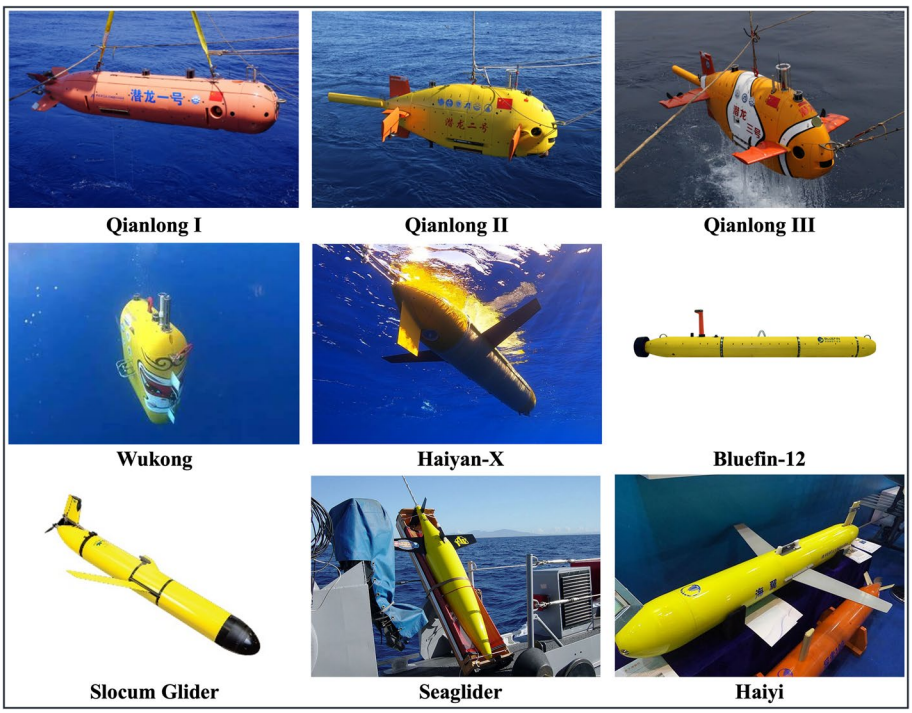

Fig. 26 Representative deep-sea AUVs and UGs

mechanical actuators to adjust volume and buoyancy [289]. Thermal gliders (e.g., Seaglider), which exploit oceanic thermal gradients to generate motion [290]. Hybrid gliders (e.g., Haiyan series), which combine gliding with powered propulsion for enhanced maneuverability. Application-based classification includes environmental monitoring gliders [291], military reconnaissance gliders such as the U.S. Navy's Liberdade [292], and polar observation gliders (e.g., Norway's Alba), tailored for extended deployments in high-latitude, cold-water environments [293]. Figure 26 shows the representative AUVs and UGs.

Table 8 summaries the representative AUV and UG classifications with key performance metrics. Collectively, AUVs and UGs constitute essential tools in modern oceanography, offering complementary capabilities for high-resolution seabed analysis and sustained, large-scale data acquisition.

e. Special-Purpose Submersibles

Special-purpose submersibles, particularly bionic and hybrid platforms, represent significant advancements in underwater robotics by integrating biomimetic principles with multifunctional control architectures. Bionic submersibles draw inspiration from marine organisms in morphology, propulsion, and functional adaptation, enhancing hydrodynamic efficiency, maneuverability, and environmental compatibility [294]. Design strategies include morphological biomimicry, locomotive biomimicry, and functional biomimicry, enabling low-noise, agile operation in complex environments. These platforms offer notable advantages over conventional systems in ecological monitoring, covert operations, and precision infrastructure inspection [295, 296]. Globally, various prototypes exemplify bionic design. Northrop

Table 8 AUV and UG classifications with key performance metrics [282–293]

Type	Max depth (m)	Dive duration (h)	Propulsion type	Key features	Representative models
Shallow-water AUV	< 500	6–24	Electric	Compact, nearshore survey and inspection	/
Deep-water AUV	500–6,000	10–40	Electric/Hybrid	High-resolution seabed mapping, exploration	*Qianlong* series
FOD AUV	> 6,000	12–48	Electric/Hybrid	Abyssal exploration, high-pressure endurance	*Wukong*
Electric AUV	Up to ~ 6,000 (varies)	8–30	Lithium-ion battery	Versatile, common for many mission types	Bluefin-12
Fuel-cell AUV	Up to ~ 6,000	40–60 +	Hydrogen fuel cells	Extended range, energy-dense propulsion	*URASHIMA*
Hybrid AUV	Up to ~ 6,000	30–72	Buoyancy + propeller	Energy-efficient with better navigation control	*Haiyan-X*
Traditional Glider	~ 1,000–2,000	Weeks to Months	Buoyancy-driven (electric)	Minimal energy consumption, large-area observation	Slocum
Thermal Glider	~ 1,000–2,000	Weeks to Months	Thermal gradient-driven	Exploits environmental heat differentials	Seaglider
Hybrid Glider	~ 2,000–4,000	Weeks to Months	Buoyancy + propeller	Combines gliding endurance with improved mobility	*Haiyan* series
Environmental UG	~ 1,000–2,000	Long-duration	Buoyancy-driven	Multi-parameter sensing	/
Military Recon UG	~ 1,000–3,000	Long-duration	Buoyancy-driven	Covert operation, long-range intelligence gathering	*Liberdade*
Polar Observation UG	~ 1,000–2,000	Long-duration	Buoyancy-driven	Cold-resistant design, high-latitude resilience	*Alba*

Grumman's "Manta" UUV replicates ray-like gliding for stealth in turbulent waters [297]. Norway's "Eelume" employs a flexible eel-inspired body for confined-space inspection [298]. Japan's "Medusa" and "OctoBot" integrate cephalopod-inspired designs for high-mobility tasks [299]. China's "RobDact" and "West Valley I" feature biologically driven propulsion and composite structures for agile and deep-sea operations [300, 301]. These developments signal a shift toward swarm-capable, intelligent bionic systems, with China leading efforts in control optimization and material innovation.

Hybrid submersibles combine the advantages of AUVs and ROVs, enabling seamless transitions between autonomous mapping and tethered precision control. The two main classes, Autonomous and Remotely Operated Vehicles (ARVs) and Hybrid Remotely Operated Vehicles (HROVs), support operational flexibility across depth ranges and mission profiles. The U.S. Nereus reached the Mariana Trench as the

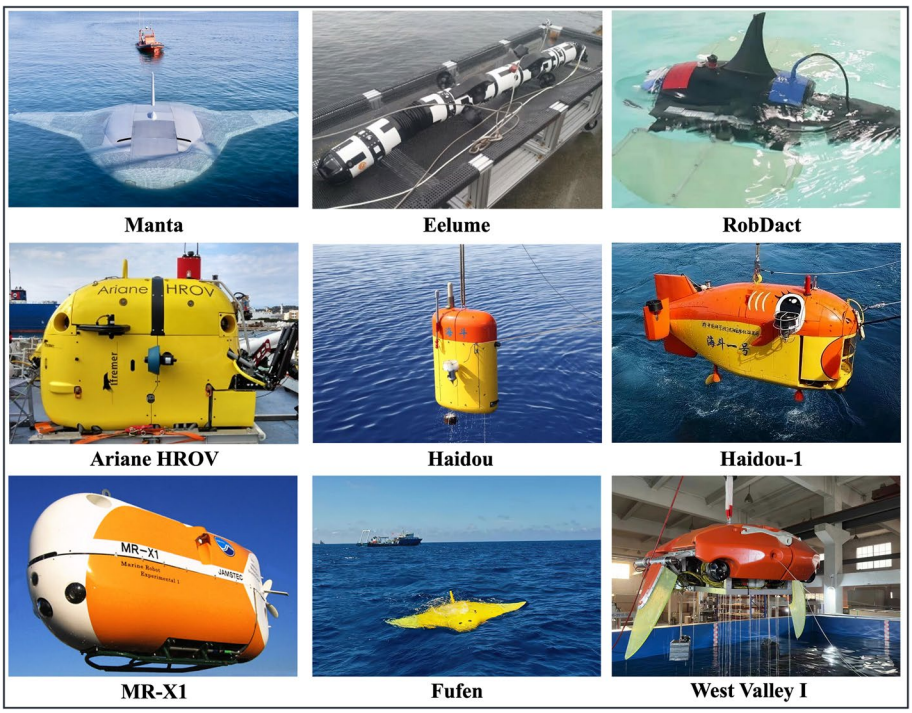

Fig. 27 Representative special-purpose submersibles

Table 9 Representative special-purpose submersibles' performance [297–306]

Platform	Type	Max depth (m)	Dive duration (h)	Key features
Manta UUV (USA)	Bionic	~500–1,000	10–20	Manta ray-inspired gliding, stealth recon, turbulence adaptation
Eelume, (Norway)	Bionic	~500–1,000	Long-endurance	Snake-like body, flexible inspection of pipelines and structures
Medusa/OctoBot (Japan)	Bionic	~500	5–10	Squid/octopus-inspired rapid maneuvering and manipulation
RobDact (China)	Bionic	~100–200	Short-mission	Fish-inspired with pectoral fin oscillation for agile motion
West Valley I (China)	Bionic	2,000	8–12	Rigid-flexible structure, manta ray morphology, pressure-resistant design
Nereus HROV (USA)	HROV	10,902	6–10	FOD, hybrid control, lost in Mariana Trench mission
Ariane HROV (France)	HROV	~2,500–3,000	8–12	Coral reef and canyon exploration, biodiversity assessment
MR-X11 Japan)	HROV	4,200	6–10	Three operational modes, resource exploration, infrastructure inspection
Polar-ARV (China)	ARV	~1,000	6–12	Airborne deployment, under-ice missions, fiber-optic comms
Haidou (China)	ARV	10,767	8–12	Third in world to reach > 10,000 m, Mariana Trench survey
Haidou-1 (China)	ARV	10,907	10–14	China's first FOD ARV, national depth record

first FOD HROV before its loss in 2014 [302]. France's Ariane HROV specializes in complex benthic terrain surveys [303], while Japan's MR-X11 supports three operational modes up to 4,200 m [304]. The Shenyang Institute of Automation pioneered Polar-ARV for polar missions [305], followed by Haidou and Haidou-1, which achieved dives of 10,767 m and 10,907 m respectively, positioning China at the forefront of hybrid deep-sea exploration [306]. Figure 27 shows the representative special-purpose submersibles.

Table 9 summaries the representative special-purpose submersibles with key performance metrics. Future developments are expected to focus on swarm intelligence, advanced materials, and energy autonomy. Intelligent cooperative control, bioinspired actuation, and adaptive autonomy will further extend the functionality and deployment range of these systems. Collectively, these trajectories will accelerate the formation of an intelligent, resilient, and ecologically adaptive underwater robotic infrastructure.

Submersible systems, including HOVs, ROVs, AUVs, UGs, and emerging bionic and hybrid platforms, offer complementary capabilities across diverse underwater missions. HOVs enable real-time human decision-making but are limited by cost and endurance. ROVs support high-power, remote operations yet rely on tethered control. AUVs allow untethered, long-range surveys but face constraints in adaptability and energy. UGs provide ultra-long endurance for environmental monitoring, though with limited speed and payload. Bionic and hybrid systems enhance maneuverability and flexibility but remain technically complex and less mature. Future advancements will integrate AI-driven autonomy, next-generation energy systems, and adaptive materials to improve endurance, resilience, and operational intelligence. These innovations will support the deployment of intelligent, full-depth, and networked submersible fleets, forming the foundation for digital ocean twins and enabling transformative progress in ocean exploration, resource management, and climate sci ence.

Full-depth camera and application

a. The evolution of water-related imaging technology

The development of water-related imaging technologies represents a significant chapter in the history of both photography and oceanic exploration. From rudimentary beginnings to sophisticated FOD imaging systems, this field has progressed through remarkable technological innovations that have expanded our understanding of marine environments.

As shown in Fig. 28, in the mid-nineteenth century, William Thompson pioneered water-related photography by capturing the first images using a camera mounted on a pole. Later, in 1893, French biologist Louis Boutan significantly advanced the field by developing specialized equipment for water-related photography, including an underwater flash and a remote-control mechanism utilizing an electromagnet.

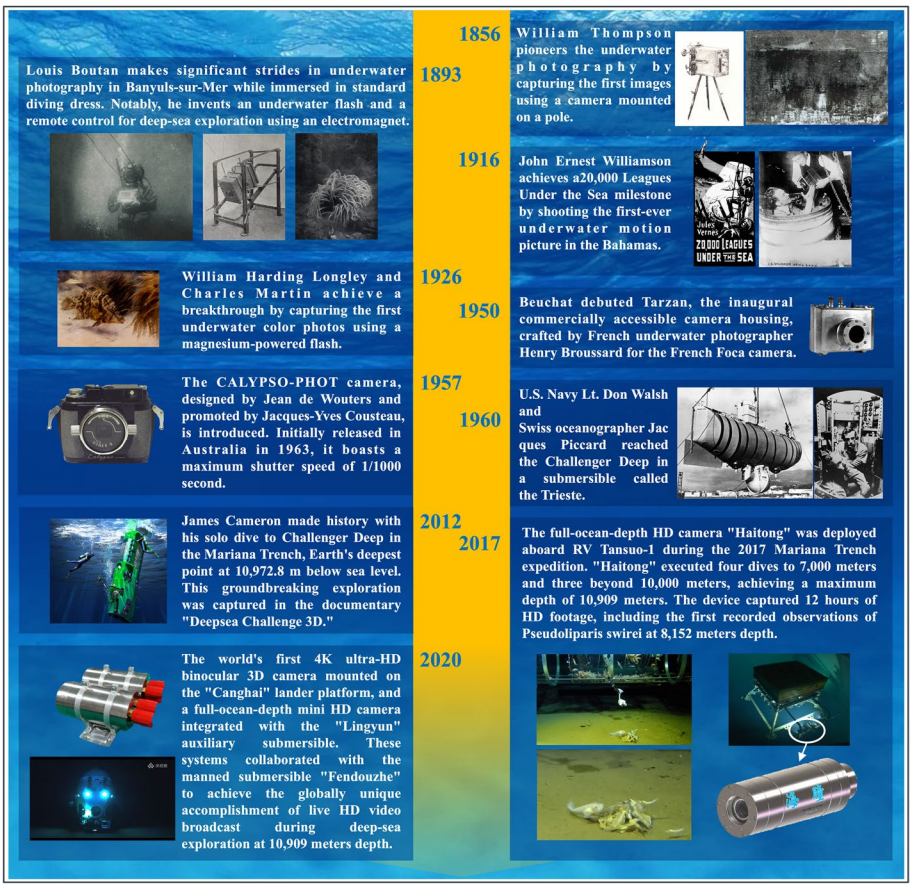

Fig. 28 History of underwater camera

The early twentieth century saw further milestones. In 1914, John Ernest Williamson utilized a device called the “Photosphere” to shoot “Thirty Leagues Under the Sea”, one of the first underwater motion pictures, filmed in the Bahamas. In 1926, William Harding Longley and Charles Martin achieved a breakthrough by capturing the first underwater color photographs using a magnesium-powered flash. Advancements continued with the introduction of specialized equipment. In the 1950s, Beuchat debuted “Tarzan”, the first commercially available underwater camera housing, designed by French photographer Henry Broussard for the Foca camera. Subsequently, the CALYPSO-PHOT camera, conceived by Jean de Wouters and promoted by Jacques-Yves Cousteau, was introduced. Initially released in 1960, it was later marketed by Nikon as the Nikonos in 1963, featuring a maximum shutter speed of 1/1000 s. Deep-sea exploration also marked significant achievements. On January 23, 1960, U.S. Navy Lieutenant Don Walsh and Swiss oceanographer Jacques Piccard reached the Challenger Deep in the Mariana Trench aboard the submersible Trieste, descending to a depth of 10,916 m. In 2012, filmmaker James Cameron made a historic solo dive to the same location in the Deepsea Challenger submersible, reaching a depth of approximately 10,908 m. This expedition was documented in the film “Deepsea Challenge 3D”.

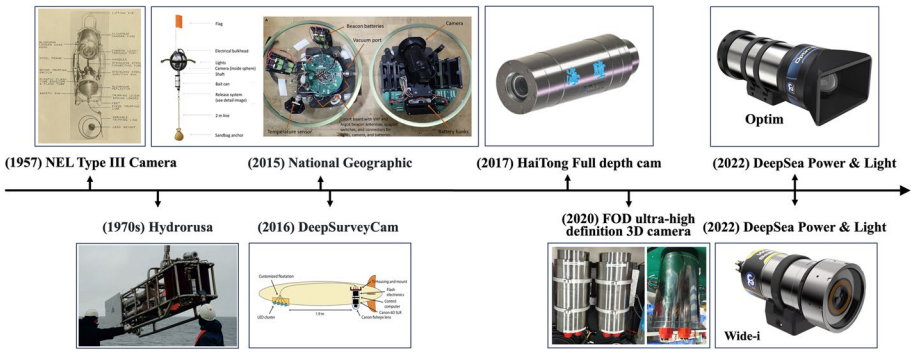

Fig. 29 Landmark research achievements in deep-sea cameras abroad

Recent years have seen remarkable progress in water-related imaging technology. In 2017, the FOD HD camera Haitong was deployed aboard the research vessel Tansuo-1 during a Mariana Trench expedition. Additionally, the Canghai lander platform was equipped with the world's first 4 K ultra-HD binocular 3D camera, and the Lingyun ROV integrated a FOD mini-HD camera. These systems collaborated with the Fendouzhe to achieve the globally unique accomplishment of live HD video broadcast during deep-sea exploration at a depth of 10,909 m.

b. FOD imaging

The FOD imaging system functions as a critical deep-sea periscope and represents a cornerstone strategic technology for China's national oceanographic endeavors. Its development constitutes not merely a declaration of technological capability in conquering the abyssal depths exceeding 10,000 m, but a fundamental requirement for safeguarding national resource security and maritime sovereignty. Detailed exploration of strategic seabed resources, such as methane hydrates (clathrates) and polymetallic nodules, demands millimeter-scale imaging to resolve micro-fractures within ore bodies. Likewise, in-situ observation of extremophiles inhabiting deep-sea hydrothermal vents is essential, yet more than 80% of these organisms cannot survive the pressure changes imposed by traditional sampling. Both endeavors require FOD optical systems that remain stable under hydrostatic pressures exceeding 110 MPa and in ultra-low illumination environments. Concerted co-development efforts between FOD cameras and their carrier platforms will catalyze generational advancements in domestic specialty materials, advanced sealing technologies, and ultra-high-pressure system integration. This synergy is anticipated to establish an autonomous, end-to-end sensing capability spanning from shallow coastal waters to the deepest hadal trenches, ultimately securing a proactive technological position for China within the strategic competition shaping access to and utilization of the deep-ocean frontier.

The development of deep-sea imaging systems traces its origins to the United States in the early 1950 s, with the pioneering NEL Type III deep-sea camera, as shown in Fig. 29. This film-based system, operational at depths of 6,000 m, captured sequential pairs of photographs to document microtopographic features of seabed sediments [307]. A decade later in 1963, the Edgerton deep-tow camera system revolutionized seafloor exploration by enabling systematic bathymetric mapping

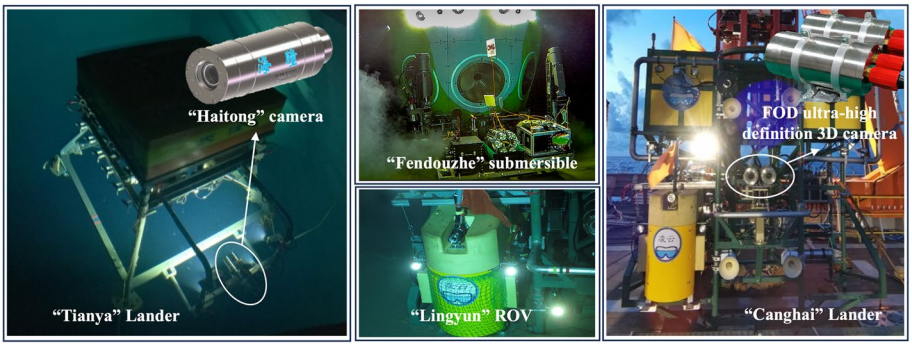

Fig. 30 Haitong camera and FOD ultra-high-definition 3D camera

Table 10 Full depth subsea HD camera systems on the market [316–319]

Manufacturer	Model	Diagonal FOV (○)	Optical zoom	Depth (m)
DeepSea Power & Light	Optim	86	15.5	11,000
DeepSea Power & Light	Super Wide-i	185	Fixed	11,000
DeepSea Power & Light	Vertex	86	10 ×	11,000
SULIS	Z70	93	12 ×	11,000

[308]. The subsequent technological progression saw the Soviet Union's Hydrorusa deep-tow apparatus during the 1970 s, equipped with ultra-low illumination level cameras and wide-angle lenses, which delivered the first documented biological observations from the Mariana Trench [309]. By the late 1990 s, the field underwent a fundamental transition from photographic film to digital imaging. The Woods Hole Oceanographic Institution (WHOI) engineered the electronic still camera, recognized as the first FOD digital imaging system [310]. Further innovations emerged in 2002 with Kevin Hardy's DOV Michelle camera, a 9,000-m-rated system incorporating synchronized strobes to facilitate biological specimen collection for Scripps Institution of Oceanography [311]. Concurrently, the National Geographic Society sponsored a decade-long deep-sea exploration initiative based on its dedicated camera system, culminating in 2015 with autonomous lander deployments featuring real-time 4 K video transmission [312, 313]. Technological maturation continued in 2016 when the GEOMAR Helmholtz Centre for Ocean Research Kiel introduced a modular pressure-tolerant imaging module for AUV [314].

In 2017, China achieved a significant milestone with the successful development of the Haitong camera system, the nation's first domestically engineered FOD high-definition imaging platform. Then, the Haitong camera was deployed aboard the Tianya lander, completing multiple dives exceeding 10,000 m. Its record-setting descent to 10,909 m yielded unprecedented video documentation of the Mariana Trench hadal environment. Haitong executed multiple dives, achieving a maximum depth of 10,909 m and capturing 12 h of HD footage, including the first recorded observations of the species Pseudoliparis swirei at 8,152 m. These visual archives provided essential primary data for multidisciplinary research, including deep-sea biology and physical oceanography, resulting in the acquisition of numerous invaluable observa-

tional datasets that filled critical knowledge gaps in marine science. Further advancing deep-sea exploration capabilities, China developed an ultra-high-definition FOD camera in 2020. Serving as the core technical component for deep-sea livestreaming, this system achieved the world's first real-time video transmission from depths exceeding 10,000 m in Fig. 30. Subsequent iterations, encompassing FOD high-definition cameras and 3D imaging systems, demonstrated exceptional performance in image enhancement, like high spatial resolution with minimal optical distortion and smooth continuous zoom functionality [315].

Currently, the main deep-sea cameras available on the international market are provided by the American company Deepsea. The camera models that meet the requirements for FOD operations are listed in Table 10.

Contemporary FOD imaging has evolved from early film systems through first-generation digital platforms to modular AUV/lander payloads and 4 K binocular rigs capable of live transmission from the hadal zone, reflecting a steady consolidation of pressure-tolerant optomechanics, low-illumination photometrics, and platform integration. The evolutionary trajectory of water-related imaging technology is fundamentally driven by the tripartite imperative of achieving enhanced clarity, extended range, and comprehensive panoramic coverage. Across today's landscape, research-grade systems emphasize millimeter-scale fidelity, endurance, and miniaturization, while commercial offerings deliver 11,000 m ratings with differentiated field-of-view/zoom trade-offs that balance situational awareness against resolution and light throughput. Future research directions will concentrate on paradigm-shifting innovations: Embedded optical designs that eliminate conventional protective windows and enable direct lens-water contact promise to eradicate refractive distortion at the fundamental physical level, establishing the optical foundation requisite for high-definition imaging. Concurrently, DL-based dehazing algorithms, rigorously grounded in the Jaffe-McGlamery radiative transfer model, offer transformative potential to overcome limitations imposed by water column scattering. These intelligent computational frameworks would empower imaging systems with unprecedented interpretative capabilities in turbid, low-illumination environments. The integration of multi-dimensional sensing modalities is advancing rapidly. In particular, the synergistic fusion of laser-line scanning with multibeam-sonar measurements enables high-fidelity 3D reconstruction of the seafloor. This progress marks a decisive shift from stand-alone optical imaging to an integrated, intelligence-driven sensing paradigm that unites acoustic, optical, and electronic resources. These synergistic advancements collectively converge toward a next-generation water-related observatory framework. This emergent paradigm seamlessly integrates the precision inherent in windowless optical architectures, the adaptive intelligence of AI-enhanced image processing, and the comprehensive contextual awareness enabled by heterogeneous data fusion. The ultimate manifestation of this integrated capability will be the transformation of the enigmatic deep-sea realm. Its intricate structures, intrinsic spectral signatures, and immersive 3D panoramas will be rendered with unparalleled fidelity and accessibility within the operational and cognitive domains of human endeavor. This paradigm

Fig. 31 Overview of representative image restoration and enhancement methods, include image denoising [321–325], color correction [326–330], image deblurring [331–334], and image dehazing [335–341]

shift promises to fundamentally expand the informational dimensions accessible for marine exploration, ushering in a new era of discovery.

AI-driven water-related optical imaging technology

Brief introduction

Image restoration and enhancement comprise a family of inverse problems that seek to recover perceptually and physically faithful imagery from data degraded by noise, blur, downsampling, compression artifacts, and, in aquatic settings, wavelength-dependent absorption, scattering, and backscatter. Restoration aims to reconstruct the latent scene by explicitly modeling image formation and solving a regularized inverse problem, whereas enhancement improves visual utility without requiring a full physical inversion. Classical methods combine degradation specific forward models with priors or constraints, solved via variational optimization or plug-and-play proximal algorithms. Learning-based approaches include supervised CNN/Transformer restorers trained on paired data, self/unsupervised schemes when ground truth is unavailable, and physics-guided unrolling that embeds the forward model within the network [320]. The Overview of representative image restoration and enhancement methods are shown in Fig. 31.

Image restoration

As the water-related environments described above pose significant challenges to imaging, such as low visibility, scattering, and spectral distortion, the acquired images are often severely degraded and cannot be used directly [342]. Consequently, image restoration is essential to recover high-quality visual information and enable accurate perception, analysis, and decision-making in such conditions [343].

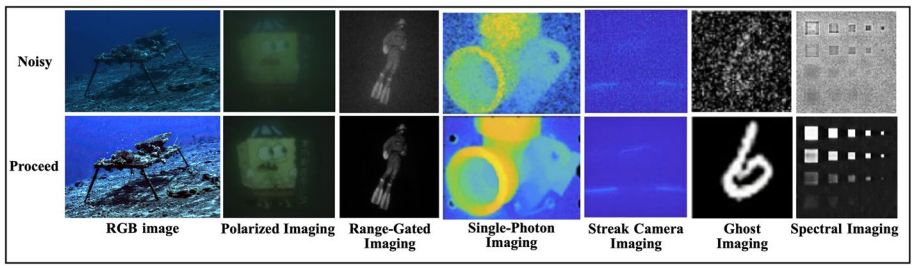

Fig. 32 Comparison of raw (noisy) and restored (proceed) outputs across various water-related imaging modalities, including RGB, polarized, range-gated, single-photon, streak camera, ghost, and hyperspectral imaging

In standard scenarios, restoration techniques are typically applied to RGB images corrupted by noise, blur, compression artifacts, or exposure issues, often assuming relatively stable environmental conditions [344]. In contrast, water-related optical imaging faces unique challenges due to the complex light propagation in water-related environments, including wavelength-dependent absorption [345], scattering [346], and backscatter [347]. Therefore, although image restoration has achieved remarkable progress in addressing generic degradations, such as Gaussian noise, motion blur, and low resolution, extending these advancements to water-related environments introduces significant challenges. Moreover, images captured in deep-sea or extremely water-related conditions frequently extend beyond standard RGB formats, incorporating specialized optical modalities such as hyperspectral, polarimetric, or single-photon imaging. These modalities are characterized by unique degradation patterns and high-dimensional data structures, necessitating restoration strategies that are tailored to both the physical imaging process and the modality-specific noise [348]. As a result, water-related image restoration must not only pursue the objectives of conventional enhancement but also account for the complex physics of light propagation in water-related environments and the distinctive features of advanced optical sensing systems [349].

Task-level taxonomy and comparisons

Generally, RGB-only image restoration tasks, such as deblurring, denoising, dehazing, and super-resolution, target distinct forms of degradation in terrestrial settings [344]. Each task addresses a specific aspect of visual quality degradation under the assumption of relatively stable imaging conditions with different image quality assessment (IQA) considerations. However, when these tasks are applied to water-related domains, their applicability must be re-evaluated in light of the unique characteristics of image data acquired under extremely water-related conditions.

a. Characteristic sensitive restoration considerations

Water-related optical imaging spans a wide range of depths and environmental conditions, from the epipelagic zone to the hadal trenches, where image reconstruction is severely affected by light propagation, combining exponential, distance and wavelength-dependent attenuation with forward scatter and backscatter. These char-

Table 11 Imaging types and restoration considerations

Imaging type	Description	Restoration	Related works
RGB image	Standard 3-channel optical image	Denoising, color correction, contrast enhancement, dehazing	WaterGAN [319], WaterMono [350], HCMPE-Net [351]
Polarized imaging	Captures light polarization states	Depolarization correction, reflection suppression	UCRNet [352], CPDCNN [353], Schechner [354]
Range-gated imaging	Time-gated optical capture	Gated signal refinement, low SNR compensation, motion deblurring	U-Net [355], Multi-PSF [356], Reconstruction [357]
Single-photon imaging	Photon-counting under ultra-low illumination	Poisson-distributed noise handling, sparse signal recovery, denoising	Physics-informed DL [358], Reconstruction [359], PICK-3D [360]
Streak camera imaging	Captures time–space slices of light intensity	Spatiotemporal interpolation, motion deblurring, slice reconstruction	N-CUP [361], 2D reconstruction from streak camera [362], Data decomposition [363]
GI	Reconstruction using intensity correlations	Denoising	Lightweight-CNN[364], CGAN [365], FUIGN [366]
Spectral imaging	Captures reflectance across many spectral bands	Band-wise denoising, spectral misalignment correction	NSCT-based fusion [367], JURTD [368], Hyperspectral 3D mapping [369]

Table 12 Imaging modalities vs. restoration tasks

Imaging modality	Deblurring	Denoising	Dehazing	Resolution	IQA considerations
RGB image	Common	Common	Common	Common	PSNR, SSIM, LPIPS
Polarized imaging	Rarely needed	Polarization noise	Backscatter removal	Uncommon	Polarization aware metrics
Range-gated imaging	Ultra-low illumination motion blur	Gate-specific noise	Residual haze remains	Temporal fusion possible	SNR, gating accuracy
Single-photon Imaging	Photon spread blur	Poisson/sparse noise	Not typical	Limited due to sparsity	Photon efficiency, edge clarity
Streak camera imaging	Temporal blur	Slice noise	Not applicable	Possible post reconstruction	Time consistency, motion IQA
GI	Indirect blur	Structured noise	Not applicable	Achievable via inversion	Fidelity to correlation
Spectral imaging	Spectral misalignment	Band-specific noise	Wavelength sensitive haze	Spatial + spectral SR	SAM, PSNR per band

acteristics significantly degrade image quality and challenge standard, linear restoration models. To address these limitations, researchers have developed a range of specialized imaging modalities tailored to water-related environments. As outlined in the previous section, these include polarized imaging for surface reflection analysis, hyperspectral systems for recovering spectral signatures, and single-photon imaging for ultra-low illumination conditions, among others. Examples of different modality proceed data is shown in Fig. 32.

Each imaging modality introduces unique data structures and degradation patterns. Restoration techniques that succeed in standard RGB domains may fail or underperform when applied directly to these high-dimensional, low-SNR, or

physics-constrained modalities. For example, range-gated imaging suppresses backscatter physically but may still require temporal deblurring, while hyperspectral imaging introduces challenges such as spectral band misalignment and wavelength-dependent noise. Addressing these issues requires restoration methods that are not only data-driven but also sensitive to the physical characteristics of each imaging process. Table 11 summarizes these modalities along with their distinctive restoration considerations.

b. Task Mapping Across Modalities
To further illustrate how traditional image restoration tasks map onto these modalities, Table 12 provides a concise taxonomy of the applicability of deblurring, denoising, dehazing, super-resolution, and image quality assessment (IQA) across different imaging types.

Network architecture evolution

The evolution of water-related image restoration architectures has closely followed advancements in computer vision, progressing from physically inspired heuristics to DL-based frameworks capable of learning complex degradations directly from data. In this section, we trace this progression through three phases: foundational models, learning strategies, and cutting-edge architectures.

a. Baseline models

Early water-related restoration efforts were driven by physically inspired priors such as the dark channel prior (DCP) [370], red channel enhancement [371], and wavelength compensation [372]. While these techniques provided interpretable outcomes, they were often brittle under varying water types, lighting conditions, or scene content. The release of benchmark datasets like underwater image enhancement enchmark (UIEB) [45] enabled the development of learning-based baselines, where convolutional networks significantly outperformed traditional methods by optimizing end-to-end restoration mappings on paired training data.

b. Learning strategies
To enhance the robustness and generalization of underwater image restoration systems under limited supervision, researchers have adopted a range of learning paradigms that reduce dependence on large-scale paired datasets and account for the unique challenges of underwater environments. Supervised learning remains foundational when paired ground truth is available. Models such as UWCNN [373] and Water-Net [374], trained on curated datasets like UIEB [45], EUVP [375] using pixel-wise and perceptual loss functions, achieve strong quantitative and qualitative restoration performance. In scenarios where clean references are difficult to obtain, unsupervised and self-supervised approaches, including CycleGAN [376] and Noise2Void [377], enable training on unpaired or noisy data, offering practical advantages for real-world underwater applications. Domain adaptation methods further mitigate the synthetic-to-real domain gap through adversarial learning, feature alignment, and style transfer, allowing models trained on synthetic datasets such as those gen-

erated by WaterGAN [319] to generalize to in situ conditions. Additionally, physics-informed and model-based learning integrates underwater imaging models (e.g., light attenuation and scattering) into network architectures or loss functions, as seen in model-unfolding approaches [378] and hybrid frameworks incorporating physical priors [379], thereby improving interpretability, robustness, and physical consistency in restoration outcomes.

c. State-of-the-art models

The latest generation of architectures leverages powerful attention mechanisms and scalable model designs. Transformer-based models such as SwinIR [380], Restormer [381] and Uformer [382] offer long-range spatial reasoning, making them ideal for heterogeneous degradations and multi-modal underwater data (e.g., hyperspectral or polarized imaging). Their modularity allows for domain-specific adaptations, such as spectral or polarization-aware attention blocks. However, despite those advancements, a central challenge remains: achieving generalization across diverse underwater modalities while maintaining inference efficiency on resource-constrained platforms such as AUVs or submersible payloads.

d. Restoration meets semantics: generative and prompt-based AI

Beyond architectural sophistication, recent advances emphasize the role of semantic guidance and generative priors. Generative models like GANs and diffusion-based approaches enhance perceptual quality by learning to produce visually plausible textures and colors [383]. These methods are especially helpful in low-SNR modalities such as ghost or single-photon imaging, where conventional pixel-based training is not feasible. More recently, prompt-based AI has emerged as a promising direction for controllable and adaptive restoration. Models such as PromptIR [384], MiOIR [385], and DPPD [386] introduce the concept of conditioning restoration on degradation type, scene content, or user input, enabling task-specific behavior. While still underexplored in water-related settings, these methods hold strong potential for complex imaging systems like hyperspectral or range-gated cameras, where degradation patterns vary dynamically with environment and depth. Prompt-driven frameworks could enable multi-modal, interpretable, and mission-aware restoration pipelines for water-related applications.

Water-related image restoration has progressed from physics-inspired priors to learning-based and physics-guided frameworks, driven by degradations unique to aquatic light transport and by modality diversity beyond RGB. Supervised CNN baselines trained on UIEB/EUVP-style datasets outperform classical priors but suffer from label scarcity and domain shift, motivating unsupervised/self-supervised and domain-adaptation strategies as well as model-unfolding that embeds radiative-transfer physics for interpretability and robustness. State-of-the-art transformer architectures extend receptive fields for heterogeneous degradations and can be specialized with spectral/polarization attention, while generative and prompt-based methods enable task-conditioned, mission-aware restoration. Persisting challenges include generalization across water types and depths, modality-specific IQA, and efficient onboard inference for AUV/ROV deployment.

Next-generation water-related image restoration must move beyond RGB enhancement toward unified, robust, and interpretable frameworks that adapt across imag-

ing modalities and environmental conditions. These systems should handle diverse sensor outputs, such as hyperspectral, polarized, and low-photon time-resolved data. This shift calls for hybrid methods that combine physical priors (e.g., light transport, attenuation) with data-driven learning. Approaches like deep unfolding, physics-guided layers, and plug-and-play optimization show promise. Recent prompt-based models (e.g., DPPD [386], MiOIR [385]) further enable adaptive restoration based on degradation type, semantic cues, or mission context, key for dynamic water-related scenarios.

Robustness must extend to real-world deployment, with models generalizing across depths, water types, and camera setups without retraining. Lightweight architectures are crucial for onboard processing in AUV/ROV. Integrating multimodal sensing and feedback-driven adaptation can enhance both perceptual quality and operational reliability. Ultimately, achieving unified restoration requires modular, interpretable, and adaptive frameworks, rooted in physics and enhanced by semantic AI, to balance scientific accuracy with practical deployment.

Image enhancement

Water-related image enhancement plays a vital role in improving target detection and recognition in low-visibility water-related environments by reducing noise, correcting color distortions, and restoring image details. These enhancements provide essential support for the automatic identification and classification of potential threats, thereby elevating the performance and intelligence of underwater situational awareness systems. With the rapid advancement of computer vision and AI, water-related image enhancement techniques have evolved into a more systematic framework. Existing approaches are typically classified into three categories, the first of which comprises traditional color- and contrast-enhancement methods operating in the spatial or frequency domains, exemplified by histogram equalization, Retinex-based algorithms, and white-balance correction. Model-based approaches that restore image quality by simulating physical degradation mechanisms such as light attenuation and scattering. DL-based approaches, which leverage the representational power of neural networks to achieve notable improvements in color fidelity and fine-detail reconstruction.

Traditional image enhancement methods

Traditional image enhancement methods mainly include histogram adjustment, color correction, sharpening enhancement, and Retinex-based approaches. Histogram adjustment methods [387–389] are among the earliest techniques applied to image enhancement, with the basic idea of improving image contrast and visual effect by modifying the grayscale distribution. Histogram equalization enhances the contrast of water-related images by computing the cumulative distribution function (CDF) of grayscale values and remapping the original pixel intensities to achieve a uniform distribution across the grayscale range. Color correction methods [390, 391] analyze the distribution characteristics of image color channels and use color priors or physical models to perform gain adjustments or color space mapping on each channel, correcting color shifts caused by lighting conditions and water attenuation, and restoring the natural tone of the image.

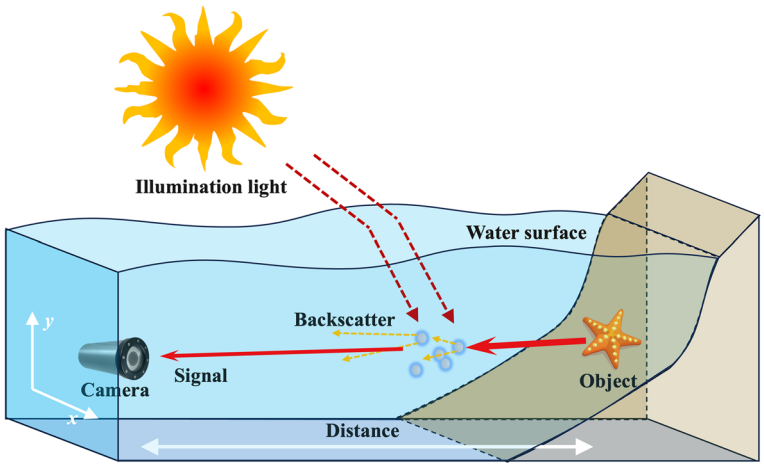

Fig. 33 Water-related imaging model diagrams

Sharpening enhancement [392] enhances image clarity and visual contrast by extracting and emphasizing high-frequency components such as edges and textures, typically using gradient or Laplacian operators. The Retinex theory [393] models an image as the product of illumination and reflectance, and by estimating or suppressing the illumination component, it highlights reflectance information to achieve color correction and enhancement under non-uniform lighting conditions. However, most of these methods do not deeply consider the physical mechanisms of water-related optical propagation, and the enhancement results are heavily dependent on the image content, lacking generalization ability. As a result, they struggle to achieve consistent enhancement in diverse and dynamically changing water-related environments. Therefore, recent research has gradually shifted toward approaches that integrate underwater imaging models with learning strategies, achieving significant performance improvements driven by DL and generative models.

Model-based methods grounded in water-related imaging models

Water-related imaging models can accurately simulate the degradation process of images caused by environmental factors such as water depth, water type, and the concentration of suspended particles, and estimate relevant physical parameters. By applying the inverse process of the image degradation model, these methods restore images to recover clear and realistic water-related visual information. The Jaffe-McGlamery model [394], a representative water-related imaging model, simulates the absorption and scattering effects during water-related light transmission and models the water-related imaging process as a physical degradation composed of three components: direct radiance, forward scattering, and backscattering. This model first establishes the image degradation equation and estimates key parameters required for light propagation, such as the medium attenuation coefficient, background light intensity, and transmittance. Then, it uses these parameters to reverse-calculate the true radiance of the target object. Finally, it applies image processing techniques such as white balance and contrast enhancement to further optimize image quality, thus achieving physically consistent restoration and enhancement of images affected by turbid water, as illustrated in Fig. 33.

Based on this theory, many physically modeled image restoration algorithms have been proposed [395], such as the DCP [396] and its various variants [397–399]. Model-based image restoration methods have solid theoretical foundations and practical feasibility in the field of water-related image enhancement, especially when imaging parameters are known or can be estimated, enabling effective recovery of intrinsic image information. However, due to the high complexity of real ocean environments and the difficulty of accurately acquiring imaging parameters, these methods still face limitations in practical applications, including poor robustness and strong dependence on parameter estimation.

DL-based methods

With the development of DL technology, its powerful feature extraction and nonlinear modeling capabilities enable automatic learning of characteristics such as color shifts, detail blurring, and degradation patterns in water-related images. As a result, DL has been widely applied to water-related image enhancement tasks to achieve more natural color restoration and clearer image reconstruction. DL methods are mainly divided into two categories, including CNN-based approaches and GAN-based approaches. Additionally, some studies have introduced contrastive learning strategies to improve unsupervised restoration performance.

a. CNN

   Li et al. [400] proposed a lightweight convolutional network called Underwater CNN (UWCNN), which integrates water-related scene prior information and achieves efficient enhancement of water-related images and videos by learning the mapping between degraded and clear images. Li et al. [401] further designed a multi-branch network called WaterNet with a gated fusion structure that integrates feature responses from multiple enhancement branches, effectively improving color representation and detail restoration. They also constructed the UIBE dataset, promoting the widespread application of DL in this field. Additionally, Li et al. [402] proposed the Ucolor network, which is based on medium transmission map-guided multi-color space embedding, effectively correcting color shifts and contrast deficiencies in water-related images. Wang et al. [403] fuses RGB and HSV color spaces to enhance the network's robustness to color distortion. Fu et al. [404] are the first to formulate water-related image enhancement as a problem of probabilistic distribution learning and consistency optimization, proposing a probabilistic model-based network architecture to address challenges caused by blurred reference images in real scenarios.

b. GAN

   GAN dues to their lower dependence on paired training samples, have been widely applied in water-related image enhancement. Li et al. [342] innovatively proposed WaterGAN, which combines deep depth estimation and color restoration subnetworks to achieve water-related image synthesis and enhancement, significantly improving image realism and clarity. Guo et al. [405] developed a multi-scale dense GAN module with residual connections, markedly enhancing the restoration of structural details and textures. Hambarde et al. [406] introduced an end-to-end

UW-GAN framework that employs a coarse-to-fine joint network to substantially improve water-related single-image depth estimation and enhancement. Liu et al. [407] proposed WSDS-GAN, a weakly-strongly supervised enhancement method based on CycleGAN, which alleviates the dependency on paired data while significantly boosting detail recovery and perceptual quality of water-related images. Current DL methods extract local features through convolutional kernels but struggle to capture long-range dependencies or global structural information within images, which severely limits their practical effectiveness in handling complex water-related images across diverse water-related environments.

c. Transformer

With the continuous advancement of Transformer technology, its superior global modeling capability enables it to effectively capture long-range pixel dependencies in images through the self-attention mechanism, thereby overcoming the limitations of traditional CNN, which are constrained by local receptive fields. This advantage allows multimodal large models to demonstrate stronger feature extraction and representation capabilities in water-related image enhancement tasks, particularly excelling in handling complex lighting variations and restoring distant targets.

Alexey et al. [408] were the first to demonstrate the effectiveness of the Vision Transformer (ViT) in image classification tasks, showing that excellent performance can be achieved without convolutional structures, solely by modeling sequences of image patches, challenging the long-standing dominance of CNNs in visual tasks. Subsequently, Liu et al. [409] proposed the Swin Transformer, which introduces sliding windows and cross-window connections, significantly improving computational efficiency while maintaining strong modeling capabilities, making it more suitable for high-resolution image tasks. In the field of image restoration, Zamir et al. [410] proposed Restormer, which optimizes the multi-head attention and feedforward network structures to retain long-range dependency modeling while enhancing adaptability to large-scale images. Peng et al. [411] designed the U-shape Transformer, which integrates a channel multi-scale feature fusion module and a spatial global feature modeling module, significantly improving the handling of uneven color attenuation and local detail restoration.

A representative fusion-based approach is the learning-physics framework of Liu et al. [412]. It combines an explicit scattering imaging model with a trainable neural prior. The forward process is encoded as differentiable constraints or unrolled steps. A deep network provides data-driven regularization to restore color, contrast, and fine detail. Temporal coherence stabilizes video under changing scatterers. This fusion outperforms model-only pipelines that break under parameter mismatch and data-only methods that generalize poorly across water types and motion. It achieves higher SNR and SSIM with fewer measurements. The result is greater physical fidelity, better sample and compute efficiency, and improved robustness. Remaining challenges include adequate training coverage and careful calibration of model terms. Even so, hybrid unrolling and plug-and-play designs offer a practical path to mission-grade enhancement in dynamic scattering.

Beyond visual quality, the downstream utility of enhanced imagery is now routinely benchmarked. For example, after feeding the restored range-gated frames into

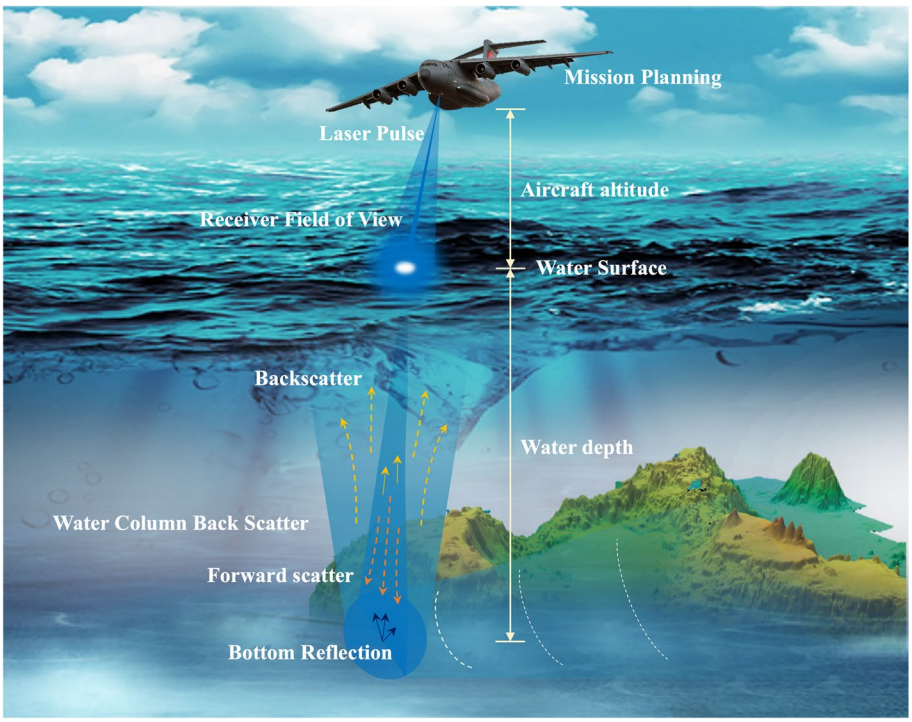

Fig. 34 Principle of ALB

YOLO-v3, the model achieves 83.5% mAP in object detection. In contrast, when using the original, unprocessed images as input, the targets are barely detectable, demonstrating the critical importance of image restoration for reliable perception [355]. This addition highlights the practical benefits of underwater image enhancement beyond visual quality, directly supporting more reliable perception in subsequent tasks.

Overall, transformers for water-related image enhancement are shifting to physics-aware, domain-specific designs. They capture long-range dependencies and cross-channel cues, including spectral and polarization signals. Pruning, quantization, and distillation enable deployment on AUV/ROV edge hardware. This yields adaptive, mission-aware processing under changing water types and illumination. Progress requires efficient, uncertainty-aware models that run in real time. Evaluation must be modality-aware and go beyond RGB, adding spectral fidelity and task-level metrics. Close sensor-algorithm co-design and standardized calibration are essential. Such physically grounded, semantics-informed, and resource-efficient pipelines deliver robust performance across diverse modalities and conditions.

Application

Advances in airborne lidar bathymetry (ALB) systems

ALB employs blue/green wavelength laser pulses transmitted from a nadir-pointing scanner aboard a fixed-wing aircraft or rotary-UAV to simultaneously sense the water surface and the seafloor. By measuring the differential time-of-flight between the

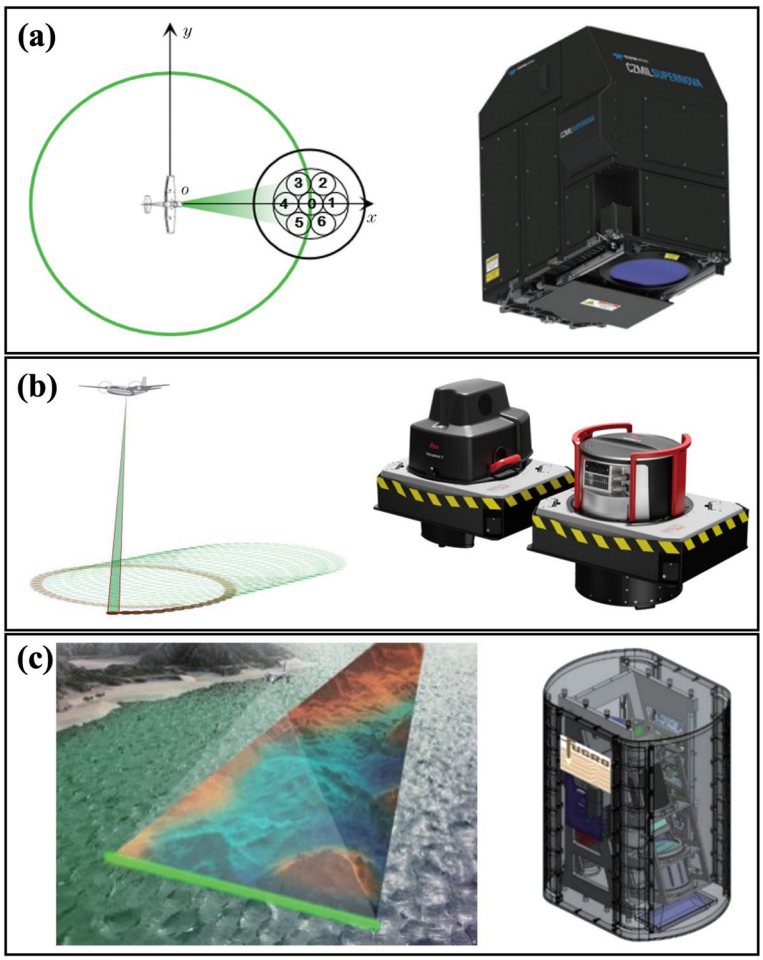

Fig. 35 Schematic diagram of ALB systems. **a** Scanning receiving field of view and photo of CZMIL SuperNova. **b** Scan pattern diagram and photo of HawkEye-5. **c** Detection pattern and model diagram of RAMMS

first surface return and subsequent bottom return, ALB yields depth estimates with decimeter-level vertical accuracy and sub-meter horizontal resolution, while seamlessly merging with topographic LiDAR to generate continuous "topo-bathy" digital elevation models across the land-sea interface. Contemporary ALB systems integrate narrow laser beam divergences, high pulse repetition frequencies, and waveform-digitizing receivers that capture the full backscatter signal, enabling sophisticated deconvolution and radiometric corrections that mitigate turbidity-induced pulse broadening and water-column attenuation. These advances have expanded the effective sounding depth from ~10 m in turbid estuaries to > 50 m in optically clear shelf waters, supporting nautical charting, coastal vulnerability assessments, benthic habitat classification, and sediment-transport studies. The principle of ALB is shown in Fig. 34.

Advances in international ALB systems

In 1969, Hickman and Hogg [413] first demonstrated laser bathymetry, confirming the feasibility of using blue–green laser pulses to detect submerged targets. Through the

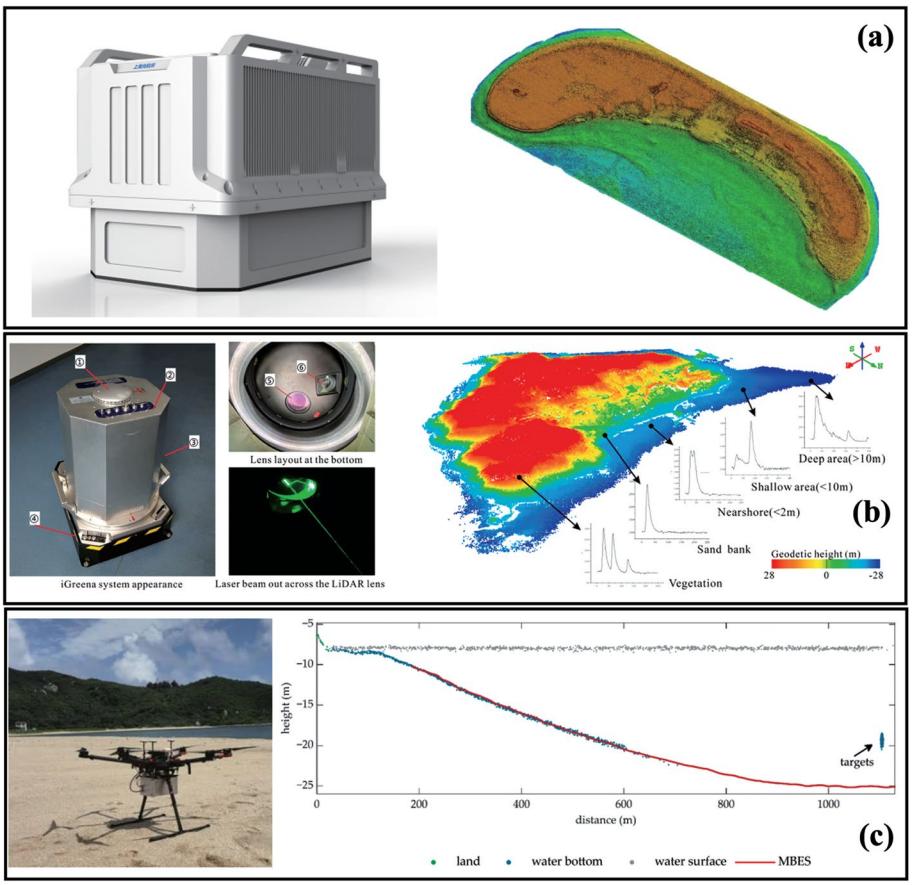

Fig. 36 Diagram of ALB systems of China. **a** Mapper5000 model and sea-land topographic elevation model of Chilianyu island. **b** iGreena photo and echo signals of different targets in coastal zone. **c** Mapper4000U mounted on drone and profile of measured cross-section of 3D point clouds

1980 s, ALB prototypes such as AOL [414], LARSEN 500 [415], WRELADS [416], and FLASH [417] validated airborne LiDAR's potential for hydrographic mapping, as shown in Fig. 35. By the late 1990 s, operational systems like SHOALS [418], HAWKEYE [419], and LADS [420] adopted core technologies, including dual-wavelength lasers, high-speed scanners, full-waveform recorders, and GPS/IMU integration, meeting IHO standards for routine coastal surveying. Post-2010, second-generation ALB systems, including CZMIL [421], HAWKEYE-Ⅲ, LADS HD, and VQ-880-G, introduced major advances: higher pulse repetition (3 to 5 ×), multi-channel receivers with GHz waveform digitizers, and automated post-processing, enabling seamless topo-bathymetric integration and improved IHO S-44 compliance. Enhancements in adaptive signal processing, co-mounted imagers, and real-time quality control extended depth range (~3 × Secchi depth) and cut manual effort by up to 60%. Since 2018, leading ALB platforms have further evolved. CZMIL SuperNova partitions its FOV into multiple shallow/deep channels for denser nearshore returns and stabilized scanning via a wedge-mirror spinner. Leica's HawkEye-5 adopts a dual-module design with elliptical scanning for mission flexibility. Fugro's RAMMS replaces mechanical scanning with lightweight streak-tube imaging, offering ± 25° swath coverage suitable for UAV deployment and simplifying calibration [422]. Driven by rapid progress in uncrewed

Table 13 Comparison of ALB imaging system parameters

System	Platform	Laser	Measurement rate	Max depth rule	Depth range	Scan/FOV
CZMIL SuperNova	Manned airborne	532 nm + 1064 nm	30 kHz	Shallow: $2.9/K_d$ ($\geq$ 15%); Deep: $4.4/K_d$	/	Circular scan; laser ± 20° from vertical
HawkEye-5	Manned airborne	515 nm + 1064 nm	40 kHz	Shallow: $3.2/K_d$ ($\geq$ 15%); Deep: $4/K_d$	/	Elliptical scan; ± 14° (fore/aft), ± 20° (left/right)
RAMMS (Fugro)	Airborne and UAS-capable	532 nm	25 kHz	$4/K_d$	/	Multibeam push-broom
Mapper5000 (SIOM)	Manned airborne	532 nm + 1064 nm	10 kHz	/	Field test: 25.97 m ≈ 3 × Secchi	Elliptical scan (dual-wavelength)
Mapper4000U (SIOM)	UAV-borne	532 nm + 1064 nm	4 kHz	/	Field test: 0–16 m ≈ 1.7–1.9 × Secchi	Rotating scan; ~ ± 15° along-track, ~ ± 12° cross-track
iGreena (Shenzhen Univ.)	Manned airborne	532 nm	50–700 kHz	/	Reported max ≈16 m in field	Circular scan; half-angle 20°; swath ≈ 70% of AGL

aircraft technology, several dedicated UAV-borne ALB instruments have appeared, including Litewave's Edge, Amuse Oneself's TDOT3, and RIEGL's VQ-840-G [423]. These systems typically achieve depth penetration up to twice the Secchi-disk depth, deliver point densities exceeding 100 pts/m^2, and operate at substantially lower cost than manned-aircraft solutions, thereby expanding ALB coverage to smaller-scale or budget-constrained coastal survey projects.

Advances in ALB systems of China

Systematic research on ALB in China began in the late 1980 s, led by institutions such as Huazhong University of Science and Technology [424], Ocean University of China [425], SIOM [426], and the Naval Institute of Hydrographic Surveying and Charting [427], later joined by others including the Information Engineering University [428] and the First and Second Institutes of Oceanography [429, 430]. A broader academic-industrial network was subsequently established [431–434]. In 1998, SIOM and the Naval Institute developed LADM-I/II systems using dual-wavelength lasers (1064 nm/532 nm), achieving $4/K_d$ depth penetration and 0.30 m vertical accuracy, meeting IHO Order 1a standards for $\leq$ 30 m depths. China's third-generation ALB system, Mapper5000 [435] in Fig. 36, launched in 2017, features a 5 kHz Nd:YAG laser and partitioned FOV receivers, having mapped over 1,200 km^2 across over 40 missions. Recent advancements include iGreena [430], a 532 nm, high-pulse-rate (50 to 700 kHz) system achieving 15.9 m depth and 0.202 m RMSE in clear waters, and the 4.4 kg UAV-compatible Mapper4000U, which demonstrated 16 m penetration and 0.1268 m seabed RMSE in field trials [433]. To meet growing resolution demands, SIOM introduced Mapper-10 K and Mapper-20kU,

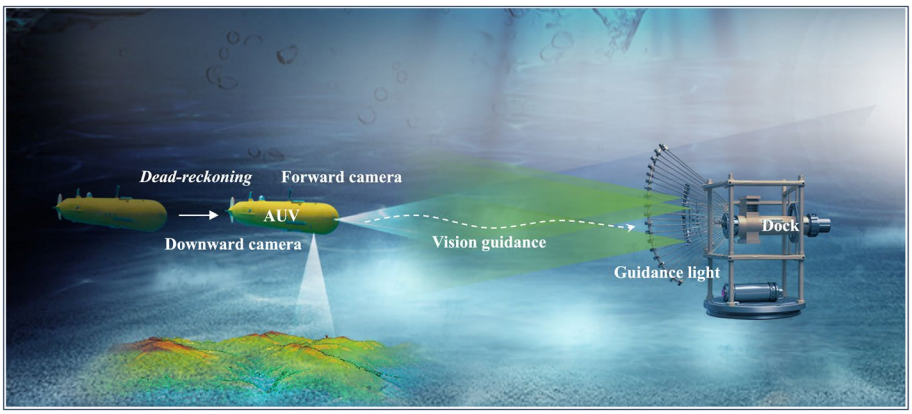

Fig. 37 Principle of AUV optical guidance

offering 2 × and 5 × point density improvements over previous models, supporting fine-scale coastal monitoring, habitat mapping, and rapid disaster response [434–436].

Table 12 compares typical ALB imaging system parameters. Dual-wavelength platforms, CZMIL SuperNova and HawkEye-5, combine a green bathymetric channel and a 1064 nm topo channel to enable seamless land–water transitions and robust bottom detection. Both implement split-rate operation with depth performance expressed by K_d-based rules, and employ stabilized, wide-angle scan patterns to balance swath and point density at survey altitudes typical of manned aircraft. RAMMS adopts a compact, green-only architecture optimized for "full water-column" waveform capture with a deep channel around tens of kHz. Its low SWaP allows deployment from both manned platforms and small UAS while maintaining useful Secchi-scaled penetration. Mapper5000 demonstrates practical tens-of-meters bathymetry at conventional altitudes with moderate point densities, whereas Mapper4000U is a UAV-borne, dual-channel system tuned for low-altitude operations, yielding high along-track densities and narrow swaths. iGreena is a single-wavelength airborne system with a wide PRF envelope and fast ADCs, prioritizing compact hardware and high sampling rates for shallow-water mapping at modest depths. In Table 13, K_d is the diffuse attenuation coefficient of water (higher $K_d \rightarrow$ more turbid). " × Secchi" expresses depth as a multiple of Secchi disk depth used in practice by some vendors.

AUV optical guidance

Localization and guidance are one of the key components that enables the autonomy of AUV, which leverages the long-term, on-station vehicle launch and recovery for the water-related missions. The guidance workflow for AUV docking is conventionally divided into two phases, mid- to long-range guidance and short-range terminal guidance, implemented through acoustic, electromagnetic, or optical modalities, either individually or in hybrid form. Mid- to long-range guidance is generally accomplished via acoustic positioning, often augmented with inertial navigation, Doppler velocity logs (DVL), and other sensors in a multi-sensor fusion scheme that steers the AUV toward the docking station. Acoustic systems afford detection ranges on the order of 10 km, but they suffer from low spatial resolution, slow data refresh rates, and susceptibility to

multipath reflections from the seafloor or target structures. Moreover, their accuracy degrades markedly at close quarters, making precise localization difficult near the docking interface. Short-range guidance governs the final approach as the AUV enters the vicinity of the dock, directly determining recovery success. This phase demands much higher positioning accuracy and therefore typically relies on electromagnetic or optical techniques. Electromagnetic signals, however, attenuate rapidly in water, exhibit limited universality, and operate over restricted ranges. In contrast, optical guidance employs photodetectors to sense and identify visual fiducials on the underwater docking station, enabling high-precision relative pose estimation while offering inherent stealth [437, 438]. A schematic of the optical guidance during AUV docking is shown in Fig. 37.

To improve the reliability of terminal AUV docking, specialized optical guidance strategies must be developed to address the unique constraints of underwater operations. Image-sensor based systems estimate the AUV's relative pose by capturing visual data of active or passive fiducials mounted at the docking entrance, extracting their features, and solving a perspective-geometry problem [439]. However, underwater optical guidance using image sensors faces significant challenges. Degradation of the underwater light field and attenuation of beacon saliency hinder reliable visual detection. Spatially varying absorption and scattering introduce geometric distortion, contrast loss, and limited effective range. Additionally, the low-texture characteristics of beacons and refractive disturbances reduce the robustness of key point extraction and matching. Environmental variability, including changes in salinity and turbidity, further alters refractive indices, leading to nonlinear pose-estimation errors and limiting the generalizability of conventional pose-solving algorithms in diverse underwater conditions. Recent DL-driven advances in underwater image enhancement have markedly improved visual detection, enabling robust key point extraction and accurate pose estimation by modeling complex data distributions. Autonomous, resilient AUV docking demands optical guidance that unites lightweight deep-learning models for real-time accuracy, hybrid optical links for sub-meter, high-speed localization, and low-latency fusion of INS, DVL, USBL, and optical data through federated filters and graph neural networks. These innovations collectively underpin next-generation intelligent electro-optical platforms for deep-sea exploration and underwater security.

Conclusion

This paper has comprehensively introduced the principles, challenges, and technological advancements of optical imaging in water-related environments, with a particular focus on deep-sea exploration. We traced the physical constraints imposed by wavelength-dependent absorption, scattering by suspended particulates, and extreme hydrostatic pressure, factors that collectively limit photon availability and degrade image quality in the mesopelagic and hadal zones. To address these barriers, the paper surveyed a range of advanced optical imaging modalities, including polarimetric imaging, range-gated imaging, single-photon imaging, streak tube imaging, GI, spectral imaging, FOD camera imaging and AI-driven algorithms. Each of these methods offers specific advantages in improving resolution, penetration depth, and operational robustness under turbid and ultra-low illumination conditions. The integration of AI further marks a critical inflection point, enabling advanced image reconstruction, denoising, and real-time

interpretation capabilities. These innovations not only improve the fidelity of deep-sea optical observations but also reduce system complexity and enhance autonomous adaptability, which is vital for long-duration missions.

Polarization imaging reduces scattering and glare. Range-gated imaging suppresses near-field backscatter and isolates depth slices. Single-photon imaging provides photon-efficient millimeter- to centimeter-scale depth in low light. Streak-camera imaging offers wide-swath, picosecond timing for high-fidelity bathymetry. GI leverages structured patterns and correlation to remain functional in heavy scatter. Spectral (hyperspectral) imaging enables material and biogeochemical discrimination. FOD camera imaging delivers reliable documentation under hadal pressures. AI-driven restoration and enhancement recover color, contrast, and fine detail while fusing multi-modal cues for robust perception.

Specifically, polarimetric imaging enhances contrast, edge saliency, and material discrimination by exploiting scattering- and reflection-dependent polarization, enabling reliable target detection in shallow, relatively clear water. Polarimetric imaging with active linear or circular illumination it can deliver centimeter-scale detail over several ALs. Its main limitations are daylight dependence for passive operation, progressive depolarization under strong turbidity and multiple scattering, and sensitivity to calibration and division-of-focal-plane crosstalk, which constrain penetration and quantitative accuracy relative to time-resolved LiDAR. In practice, polarimetry is a complement to range-gated or single-photon techniques rather than a replacement in highly turbid or long-range scenarios. Range-gated imaging isolates returns from a chosen depth slice and suppresses out-of-slice backscatter, yielding high contrast, centimeter-scale axial resolution, and millimeter-centimeter lateral detail at standoffs of tens of meters. Polarization-assisted gating and multi-gate fusion further enhance contrast and enable volumetric 3D reconstruction. Its limitations include residual in-gate multiple scattering in very turbid water, sensitivity to laser-detector synchronization and timing jitter/walk-off, motion blur during scanning or platform motion, and eye-safety/energy constraints that impose SNR and duty-cycle trade-offs. In practice, range-gated imaging is well suited to mid-range infrastructure inspection, target detection or 3D mapping from AUV/ROV and surface platforms. Underwater single-photon imaging, time-correlated SPAD or Geiger-mode APD lidar, delivers millimeter- to centimeter-scale depth accuracy at extremely low photon counts. Fielded systems reach tens of meters, and laboratory studies approach 8 to 10 ALs (or beyond), with SPAD arrays enabling real-time 3D at short standoff. Its principal advantages are very high sensitivity and statistically principled, histogram-based depth inference that remains effective in photon-starved, scattering-limited regimes, often with eye-safe, compact laser sources. Key limitations include susceptibility to ambient background and bioluminescence. Pile-up and after pulsing distort the time histograms. Pixel-to-pixel nonuniformity and pressure- or temperature-induced timing drift, multipath from boundaries, and synchronization jitter further degrade accuracy. STIL delivers wide-swath mapping over tens of meters with 1 cm range accuracy and millimeter-centimeter lateral detail, leveraging picosecond timing that maps time-of-flight into a spatial coordinate for dense, few-photon 3D profiles. Its main constraints are stringent timing and sweep-linearity calibration, cross-slit radiometric/timing consistency, and sensitivity to platform motion, together with

high-voltage requirements that limit miniaturization. In practice, STIL is best suited for high-fidelity bathymetry and geomorphology. GI uses structured illumination and bucket detection to reconstructed object through scatter, offering strong robustness to turbidity, compatibility with flexible hardware configurations. Its principal limitations are the sampling burden and acquisition latency, exacerbated by calibration demands on SLM/DMD modulators and model mismatch. Thus, practical systems benefit from compressive sensing, optimized illumination patterns, and physics-guided deep networks to reduce measurements and stabilize inversion. Recent DL and large-model approaches have improved fidelity and sampling efficiency, with demonstrations approaching on the order of 10 ALs. Spectral imaging delivers material discrimination from UV to NIR through narrowband analytics and spectral unmixing, enabling quantitative benthic classification, characterization, and identification under controlled illumination and calibration. Its effectiveness is depth-limited by per-band SNR, scattering-induced crosstalk, and radiometric drift, and the acquisition/processing load scales with band count, making it most suitable for short-range surveys on well-lit, well-calibrated platforms. FOD cameras provide operational simplicity and survivability to hadal pressures with application-dependent spatial resolution. They are challenged by ultra-low illumination and window-induced aberrations, best for persistent observation, documentation, and situational awareness on landers and ROVs. AI-driven algorithms act as a cross-cutting layer that enhances all modalities through physics-aware restoration, fusion, and autonomy. The advantages include improved robustness, denoising, and real-time interpretation, whereas risks involve domain shift, calibration sensitivity, and onboard compute budgets, most effective when co-designed with sensors (e.g., polarization-assisted gating, SPAD histogram deconvolution, STIL motion compensation, GI pattern optimization) to meet mission-specific range, resolution, and throughput targets.

Notely, while multimodal imaging can substantially enhance underwater perception, it also introduces several practical challenges. Spatial alignment between heterogeneous sensors is often imperfect, and even minor calibration errors may propagate through the processing pipeline, reducing the reliability of fused representations. Temporal synchronization presents an additional difficulty in dynamic underwater scenes, where platform motion and rapidly varying illumination require precise timing across modalities. Moreover, multimodal fusion typically increases computational complexity, which can constrain real-time performance on resource-limited AUV and ROV platforms. Addressing these issues calls for lightweight alignment techniques, adaptive synchronization strategies, and efficient fusion architectures, directions that warrant further investigation in future research.

Looking forward, future research should prioritize ultra-compact, energy-efficient imaging systems with multi-modal sensing that tolerate FOD pressures while delivering spectrally and temporally rich datasets, and should tightly couple optics with AI and robotics to enable adaptive decision-making, habitat classification, and event-triggered sampling. One of the key thrusts is complementary fusion across modalities. The polarimetric and spectral channels can provide material and surface-reflection cues that enhancing range-gated or single-photon acquisition for backscatter suppression and photon-efficient depth recovery. The streak-tube timing can anchor wide-swath bathymetry and provide ground-truth calibration.

GI compensates for the lack of light-field control in conventional imaging method by imposing known structured illumination and correlation decoding, thereby enhancing robustness to scattering. FOD cameras can host these active modules as swappable payloads for persistent hadal deployments. Realizing this fusion requires shared geometry, synchronized timing, and radiometric/spectral-Stokes calibration, together with physics constrained AI that performs joint inversion and uncertainty-aware data fusion. For submersible, future research is expected to advance real-time enhancement pipelines optimized for less than 30 ms inference on embedded GPUs, develop adaptive generalization frameworks that sustain detection accuracy across unseen water types, and design lightweight, multimodal models tailored for AUV/ROV deployment. Together, these trends will enable reliable, mission-ready underwater vision systems capable of operating robustly in diverse and challenging marine environments. With these ingredients, multi-modal, AI-enabled systems can advance deep-sea biodiversity and biogeochemistry studies and support sustainable resource assessment, ushering in high-resolution, intelligent, and exploration across the full ocean column.

Acknowledgements
Not applicable.

Authors' contributions
Zhe Sun was responsible for manuscript writing, framework design, and visual illustration creation. Tong Tian conceived the idea, performed manuscript revision, and authored the GI section. Haofeng Hu contributed to conceptual development and drafted the Polarimetric imaging section. Yan He authored the Advances in ALB systems section. Mingjia Shangguan completed the Single-photon imaging section. Tao Yu authored the Spectral imaging section. Qingsong Yang and Ye Qian jointly completed the Deep-sea submersibles section. Mingliang Chen and Yifan Chen independently contributed the GI section. Xinwei Wang contributed the Range-gated imaging section. Kanzhong Yao, Yifan Chen, and Mingyu Dou collaboratively completed the AI-driven water-related optical imaging technology section. Ye Zheng is responsible for the organizational structure design of the manuscript. Guojun Wu and Jinghan Xu completed the FOD imaging and Pressure-tolerant sealing section. Qiang Li provided technical expertise on Light source section. Xuelong Li supervised project, conceived the idea and conducted comprehensive manuscript review.

Funding
This work was supported by the National Key Research and Development Program of China (Grant No.2022YFC2808000).

Data availability
Not applicable.

Declarations

Competing interests
The authors declare that they have no competing interests.

Author details
[1]School of Artificial Intelligence, OPtics and ElectroNics (iOPEN), Northwestern Polytechnical University, Xi'an 710072, People's Republic of China. [2]Institute of Artificial Intelligence (TeleAI), China Telecom, Shanghai 200232, People's Republic of China. [3]Institute of Optics and Quantum Electronics, Abbe Center of Photonics, Friedrich Schiller University, Max Wien Platz 1, 07743 Jena, Germany. [4]Helmholtz Institute Jena, Fröbelstieg 3, 07743 Jena, Germany. [5]School of Marine Science and Technology, Tianjin University, Tianjin 300072, China. [6]Aerospace Laser Technology and System Department, Shanghai Institute of Optics and Fine Mechanics, Chinese Academy of Sciences, Shanghai 201800, China. [7]State Key Laboratory of Marine Environmental Science, College of Ocean and Earth Sciences, Xiamen University, Xiamen 361102, China. [8]Key Laboratory of Underwater Acoustic Communication and Marine Information Technology of the Ministry of Education, Xiamen University, Xiamen 361005, China. [9]Xi'an Institute of Optics and Precision Mechanics, Chinese Academy of Sciences, Xi'an 710119, China. [10]Taihu Laboratory of Deepsea Technological Science, Wuxi 214000, People's Republic of China. [11]State Key Laboratory of Deepsea Manned Vehicle, China Ship Scientific Research Center, Wuxi 214000, People's Republic of China. [12]Optoelectronic System Laboratory, Institute of Semiconductors, Chinese Academy of Sciences, Beijing 100083, China. [13]Institute of Physics and Optoelectronic Engineering, Beijing University of Technology, Beijing 100124, China. [14]Laoshan National Laboratory, Qingdao 266237, China.

Received: 15 July 2025 Revised: 3 November 2025 Accepted: 24 November 2025
Published online: 13 January 2026

References

1. Schmitt RW. The ocean component of the global water cycle. Rev Geophys. 1995;33(S2):1395–409.
2. Charette MA, Smith WH. The volume of earth's ocean. Oceanography. 2010;23(2):112–4.
3. Smith RC, Baker KS. Optical properties of the clearest natural waters (200–800 nm). Appl Opt. 1981;20(2):177–84.
4. Gardner JV, Armstrong AA, Calder BR, et al. So, how deep is the Mariana Trench? Mar Geod. 2014;37(1):1–13.
5. Haren H, Berndt C, Klaucke I. Ocean mixing in deep-sea trenches: New insights from the Challenger Deep, Mariana Trench. Deep Sea Res Part I Oceanogr Res Pap. 2017;129:1–9.
6. Bell KL, Johannes KN, Kennedy BR, et al. How little we've seen: A visual coverage estimate of the deep seafloor. Sci Adv. 2025;11(19):8602.
7. Yao W, Tian C, Teng Y, et al. Development of deep-sea mining and its environmental impacts: a review. Front Mar Sci. 2025;12:1598584.
8. Marinyuk VV, Rogozkin DB, Sheberstov SV. Optical beam spread in seawater. Opt Commun. 2025;574:131098.
9. Li X. Water-related optics. Sci China Technol Sci. 2024;54(2):227.
10. Li X. Water-related vision. Acta Electron Sin. 2024;52(4):1041–82.
11. Sun Z, Li X. Water-related optical imaging: from algorithm to hardware. Sci China Technol Sci. 2025;68(1):1100401.
12. Sun Z, Li X. Preface: water-related vision. Sci China Technol Sci. 2025;68(1):1100400.
13. Al-Zhrani S, Bedaiwi NM, El-Ramli IF, et al. Underwater optical communications: A brief overview and recent developments. Engineered Science. 2021;16(27):146–86.
14. Ke X, Li G. Characterization of blue-green light non-line-of-sight transmission in seawater. Opt Photonics J. 2022;12(11):234–52.
15. Liu B, Liu Z, Men S, et al. Underwater hyperspectral imaging technology and its applications for detecting and mapping the seafloor: a review. Sensors (Basel). 2020;20(17):4962.
16. Wu L, Zhang X, Chang J, et al. Underwater polarization image de-scattering utilizing a physics-driven deep learning method. Opt Express. 2024;32(17):30670–86.
17. Tan C, Seet G, Sluzek A, et al. A novel application of range-gated underwater laser imaging system (ULIS) in near-target turbid medium. Opt Lasers Eng. 2025;43(9):995–1009.
18. Wang J, Hao W, Chen S, et al. Underwater single photon 3d imaging with millimeter depth accuracy and reduced blind range. Opt Express. 2023;31(19):30588–603.
19. Le M, Wang G, Zheng H, et al. Underwater computational ghost imaging. Opt Express. 2017;25(19):22859–68.
20. Oren M, Nayar SK. Generalization of the Lambertian model and implications for machine vision. Int J Comput Vis. 1995;14:227–51.
21. Szafarczyk A, Toś C. The use of green laser in lidar bathymetry: state of the art and recent advancements. Sensors. 2022;23(1):292.
22. Mobley CD. Optical properties of water. Handbook of optics. 2010;4:1–1.
23. Pope RM, Fry ES. Absorption spectrum (380–700 nm) of pure water. II. Integrating cavity measurements. Appl Opt. 1997;36(33):8710–23.
24. Asano Y, Zheng Y, Nishino K, et al. Depth sensing by near-infrared light absorption in water. IEEE Trans Pattern Anal Mach Intell. 2020;43(8):2611–22.
25. Jonasz M, Fournier GR. Light scattering by particles in water: theoretical and experimental foundations. Amsterdam: Academic Press; 2007.
26. Haltrin V I. Absorption and scattering of light in natural waters. Kokhanovsky, A. A. (eds) Light Scattering Reviews. Springer Praxis Books. Springer, Berlin, Heidelberg (2006).
27. Young AT. Rayleigh scattering. Appl Opt. 1981;20(4):533–5.
28. Drake R, Gordon J. Mie scattering. Am J Phys. 1985;53(10):955–62.
29. Caimi F M. Technical challenges and recent developments in underwater imaging. Proceeding of SPIE, Micro-Optics/Micromechanics and Laser Scanning and Shaping, 2383 (1995).
30. Du H. Mie-scattering calculation. Appl Opt. 2004;43(9):1951–6.
31. Tyo JS, Goldstein DL, Chenault DB, et al. Review of passive imaging polarimetry for remote sensing applications. Appl Opt. 2006;45(22):5453–69.
32. Li X, Han Y, Wang H, et al. Polarimetric imaging through scattering media: a review. Front Phys. 2022;10:815296.
33. Nape I, Singh K, Klug A, et al. Revealing the invariance of vectorial structured light in complex media. Nat Photon. 2022;16:538.
34. Zhu Y, He Q, Fu Q, et al. Detection of underwater targets using polarization laser assisted echo detection technique. Appl Sci. 2023;13:3222.
35. Song Q, Sun X, Liu X, et al. Study on vector radiative transmission characteristics of polarization optics in underwater bubble environment. Acta Optica Sinica. 2022;42:10001.
36. Bogucki DJ, Domaradzki JA, Stramski D, et al. Comparison of near-forward light scattering on oceanic turbulence and particles. Appl Opt. 1998;37(21):4669–77.
37. Katz J, Donaghay P, Zhang J, et al. Submersible holocamera for detection of particle characteristics and motions in the ocean. Deep Sea Res Part I Oceanogr Res Pap. 1999;46:1455–81.
38. Elmabruk K, Bayraktar M. Propagation of hollow higher-order cosh-Gaussian beam in oceanic turbulence. Phys Scr. 2023;98:035519.
39. Bartlett JS, Voss KJ, Sathyendranath S, et al. Raman scattering by pure water and seawater. Appl Opt. 1998;37(15):3324–32.
40. Zhang X, Hu L. Scattering by pure seawater at high salinity. Opt Express. 2009;17(15):12685–91.
41. Zhang X, Stramski D, Reynolds RA, et al. Light scattering by pure water and seawater: the depolarization ratio and its variation with salinity. Appl Opt. 2019;58(4):991–1004.
42. Chen L, Huang Y, Dong J, et al. Underwater optical object detection in the era of artificial intelligence: current, challenge, and future. Association for Computing Machinery, New York, NY, USA, 0360–0300, (2025).
43. Jaffe JS. Computer modeling and the design of optimal underwater imaging systems. IEEE J Ocean Eng. 1990;15(2):101–11.

44. Li CY, Guo JC, Cong RM, et al. Underwater image enhancement by dehazing with minimum information loss and histogram distribution prior. IEEE Trans Image Process. 2016;25(12):5664–77.
45. Li C, Guo C, Ren W, et al. An underwater image enhancement benchmark dataset and beyond. IEEE Trans Image Process. 2020;29:4376–89.
46. Yang M, Sowmya A. An underwater color image quality evaluation metric. IEEE Trans Image Process. 2015;24(12):6062–71.
47. Panetta K, Gao C, Agaian S. Human-visual-system-inspired underwater image quality measures. IEEE J Ocean Eng. 2016;41(3):541–51.
48. Williams DP. Auv-enabled adaptive underwater surveying for optimal data collection. Intell Serv Robot. 2012;5:33–54.
49. Jordt-Sedlazeck A, Koch R, Refractive structure-from-motion on underwater images. Proceedings of the IEEE International Conference on Computer Vision (ICCV), 57–64 (2013).
50. Manov DV, Chang GC, Dickey TD. Methods for reducing biofouling of moored optical sensors. J Atmos Ocean Technol. 2004;21(6):958–68.
51. Yang B, Liu Y, Liao J. Manned submersibles—deep-sea scientific research and exploitation of marine resources. Bull Chin Acad Sci. 2021;36(5):622–31.
52. Zeng Y, Yu C, Yang S. Creep behavior research of deep-sea pressure hull: a review. J Mar Sci Eng. 2025;13(4):749.
53. Harris D C. Frontiers in infrared window and dome materials. Proc. SPIE 2552, Infrared Technology XXI, (1995).
54. Guan Z, Wu D, Cheng Q, et al. Friction and wear characteristics of CF/PEEK against 431 stainless steel under high hydrostatic pressure water lubrication. Mater Des. 2020;196:109057.
55. Song W, Cui W, Wang Z. Study of pressure-balanced oil-filled (PBOF) technology. Ocean Eng. 2023;256:110621.
56. Yang S, Shen Y, Lu B, et al. Research on oil-filled connectors for deep-sea applications. International Conference on Coastal and Ocean Engineering, 414–421 (2024).
57. Duncan DD, Baldwin KC, Blodgett DW, et al. Experimental and theoretical assessment of mechanical and optical effects in nonuniformly heated IR windows. J Hopkins APL Tech Dig. 2001;22:394–408.
58. Li X, Wang L, Li F. Study on fracture failure behaviour of sapphire transparent window under ultra-high hydrostatic pressure. Ships Offshore Struct. 2024;20(2):260–73.
59. Marouchos A, Sherlock M, Cordell J. Challenges in underwater image capture. OCEANS 2018 MTS/IEEE Charleston, Charleston, SC, USA, 1–5 (2018).
60. Duntley SQ. Light in the sea. J Opt Soc Am. 1963;53(2):214–33.
61. Smith RC, Baker KS. Optical classification of natural waters. Limnol Oceanogr. 1978;23(2):260–7.
62. Jerlov N G. Marine Optics. Elsevier Oceanography Series 14 (1976).
63. Solonenko MG, Mobley CD. Inherent optical properties of Jerlov water types. Appl Opt. 2015;54(17):5392–401.
64. Pavithra D, Varsha P. A review on underwater communication with an aerial platform. Asian J Appl Sci Technol. 2017;1(5):25–7.
65. Jamet C, Ibrahim A, Ahmad Z, et al. Going beyond standard ocean color observations: lidar and polarimetry. Front Mar Sci. 2019;6:251.
66. Sun Z, Cheng Q, Hui Y, et al. Enhancing extinction ratio of polarization and pulse stability simultaneously from passively Q-switched [100]-Nd:YAG /[110]-Cr^{4+}:YAG laser. Opt Commun. 2015;335:245–9.
67. Sun Z, Li Q, Lei H, et al. Controllable polarization for passively Q-switched Nd:YAG/Cr^{4+}:YAG laser. Opt Laser Technol. 2014;56:269–72.
68. Sun Z, Li Q, Chen X, et al. Stable polarized diode pumped passively Q-switched [100]-cut Nd:YAG laser with Cr^{4+}:YAG crystal. Opt Laser Technol. 2014;60:56–60.
69. Pavel N, Saikawa J, Taira T. Diode end-pumped passively Q-switched Nd:YAG laser intra-cavity frequency doubled by LBO crystal. Opt Commun. 2001;195(1–4):233–40.
70. Okhapkin M, Skvortsov M, Belkin A, et al. Tunable single-frequency diode-pumped Nd:YAG ring laser at 1064/532 nm for optical frequency standard applications. Opt Commun. 2002;203(3–6):359–62.
71. Lin HY, Liu H, Chen Q, et al. Passively Q-switched Nd:GSGG laser at 936.3 nm. Optik. 2020;211:164642.
72. Zhang J, Ma J, Lu T, et al. Compact wavelength tunable output around 440 nm pulsed laser for oceanic lidar application. Opt Commun. 2021;485:126706.
73. Li B, Sun B, Mu H. High-efficiency generation of 355 nm radiation by a diode-end-pumped passively Q-switched Nd:YAG/Nd:YVO_4 laser. Appl Opt. 2016;55(10):2474–7.
74. Xu B, Hou Z, Xia M, et al. High average power third harmonic generation at 355 nm with $K_3B_6O_{10}BR$ crystal. Opt Express. 2016;24(10):10345–51.
75. Wu S, Song X, Liu B. Fraunhofer lidar prototype in the green spectral region for atmospheric boundary layer observations. Remote Sens. 2013;5(11):6079–95.
76. Li X, Bai Y, Ding X, et al. High efficiency, low threshold, high repetition rate h-β fraunhofer line light at 486.1 nm generation by an intracavity frequency-doubled optical parametric oscillator. Chin Opt Lett. 2023;21(9):091403.
77. Luo Q, Ma J, Huang Z, et al. Single longitudinal mode 486.1 nm wavelength laser generation from BBO-optical parametric amplifier system for ocean detection. Applied Physics B 131(4), 1–7(2025).
78. Kitzler O, Taylor C, Li Z, et al. Photon counting marine lidar using blue laser diode excitation. Opt Express. 2024;32(26):45969–77.
79. Van Leeuwen R, Chen T, Watkins L, et al. 1W frequency-doubled VCSEL-pumped blue laser with high pulse energy. Solid State Lasers XXIV: Technology and Devices. 2015;9342:149–55.
80. Chen X, Kong W, Chen T, et al. High-repetition-rate, sub-nanosecond and narrow-bandwidth fiber-laser-pumped green laser for photon-counting shallow-water bathymetric lidar. Results Phys. 2020;19:103563.
81. He J, Wang H, Pan S, et al. Laser performance of Nd:YAG at 946 nm and frequency doubling with periodically poled litao. J Cryst Growth. 2006;292(2):337–40.
82. Deyra L, Martial I, Didierjean J, et al. 3 W, 300 μJ, 25 ns pulsed 473 nm blue laser based on actively Q-switched Nd:YAG single-crystal fiber oscillator at 946 nm. Opt Lett. 2013;38(16):3013–6.

83. Zhang H, Chen L, Wu H, et al. Hyperspectral LiDAR for subsea exploration: system design and performance evaluation. Electronics. 2025;14:1539.
84. Wang M L, Zhang W L, Wang K, et al. Laser-damage threshold of optical components based on lithium triborate (LBO) overview. Fifteenth International Conference on Information Optics and Photonics (CIOP 2024). Proc. SPIE 13418, 134182F (2024).
85. Schechner YY, Karpel N. Recovery of underwater visibility and structure by polarization analysis. IEEE J Ocean Eng. 2005;30(3):570–87.
86. Li X, Hu H, Zhao L, et al. Polarimetric image recovery method combining histogram stretching for underwater imaging. Sci Rep. 2018;8(1):12430.
87. Li X, Xu J, Zhang L, et al. Underwater image restoration via stokes decomposition. Opt Lett. 2022;47(11):2854–7.
88. Li X, Hu H, Zhao L, et al. Pseudo polarimetric method for dense haze removal. IEEE Photon J. 2019;11(1):1–11.
89. Liu T, Guan Z, Li X, et al. Polarimetric underwater image recovery for color image with crosstalk compensation. Opt Laser Eng. 2020;124:105833.
90. Hu H, Qi P, Li X, et al. Underwater imaging enhancement based on a polarization filter and histogram attenuation prior. J Phys D Appl Phys. 2021;54(17):175102.
91. Guan J, Zhu J. Target detection in turbid medium using polarization-based range-gated technology. Opt Express. 2013;21(12):14152–8.
92. Shen L, Zhang L, Qi P, et al. Polarimetric binocular three-dimensional imaging in turbid water with multi-feature self-supervised learning. PhotoniX. 2025;6:24.
93. Treibitz T, Schechner YY. Active polarization descattering. IEEE Trans Pattern Anal Mach Intell. 2008;31(3):385–99.
94. Hu H, Zhao L, Li X, et al. Polarimetric image recovery in turbid media employing circularly polarized light. Opt Express. 2018;26(19):25047–59.
95. Wei Y, Han P, Liu F, et al. Enhancement of underwater vision by fully exploiting the polarization information from the stokes vector. Opt Express. 2021;29(14):22275–87.
96. Wang H, Li J, Hu H, et al. Underwater imaging by suppressing the backscattered light based on Mueller matrix. IEEE Photon J. 2021;13(4):1–6.
97. Guan J, Ma M, Sun P. Optimization of rotating orthogonal polarization imaging in turbid media via the Mueller matrix. Opt Lasers Eng. 2019;121:104–11.
98. Liu F, Zhang S, Han P, et al. Depolarization index from Mueller matrix descatters imaging in turbid water. Chin Opt Lett. 2022;20(2):022601.
99. Huang B, Liu T, Hu H, et al. Underwater image recovery considering polarization effects of objects. Opt Express. 2016;24(9):9826–38.
100. Liu F, Han P, Wei Y, et al. Deeply seeing through highly turbid water by active polarization imaging. Opt Lett. 2018;43(20):4903–6.
101. Hu H, Zhang Y, Li X, et al. Polarimetric underwater image recovery via deep learning. Opt Lasers Eng. 2020;133:106152.
102. Hu H, Han Y, Li X, et al. Physics-informed neural network for polarimetric underwater imaging. Opt Express. 2022;30(13):22512–22.
103. Yang S, Qu B, Liu G, et al. Unsupervised learning polarimetric underwater image recovery under nonuniform optical fields. Appl Opt. 2021;60(26):8198–205.
104. Zhu Y, Zeng T, Liu K, et al. Full scene underwater imaging with polarization and an untrained network. Opt Express. 2021;29(25):41865–81.
105. Yang K, Liu F, Liang S, et al. Data-driven polarimetric imaging: a review. Opto-Electron Sci. 2024;3(2):230042.
106. Shen L, Reda M, Zhang X, et al. Polarization-driven solution for mitigating scattering and uneven illumination in underwater imagery. IEEE Trans Geosci Remote Sens. 2024;62:1–15.
107. Wu X, Chen J, Li P, et al. Deep learning-based polarization 3D imaging method for underwater targets. Opt Express. 2025;33(2):2068–81.
108. Li X, Hu H, Zhao L, et al. Polarimetric image recovery method combining histogram stretching for underwater imaging. Sci Rep. 2018;8(1):12430.
109. Wang H, Hu H, Jiang J, et al. Automatic underwater polarization imaging without background region or any prior. Opt Express. 2021;29(20):31283–95.
110. Cai C, Qiang F, Bao FC, et al. Joint polarization detection and degradation mechanisms for underwater image enhancement. Appl Opt. 2023;62(24):6389–400.
111. Ding X, Wang Y, Fu X. Multi-polarization fusion generative adversarial networks for clear underwater imaging. Opt Lasers Eng. 2022;152:106971.
112. Chen S, Liu P, He W, et al. Polarization-enhanced underwater laser range-gated imaging for subaquatic applications. Sensors. 2024;24(20):6681.
113. Fu Q, Dong C, Wang K, et al. Underwater target laser polarization suppression scattering detection technology and verification. PLoS ONE. 2024;19(6):0305929.
114. Liu Y, Yang J, Wei A-M, et al. Design of circular polarization imaging system for underwater laser gating. Sixth Conference on Frontiers in Optical Imaging and Technology: Novel Imaging Systems. 2024;13155:163–75.
115. Wang M, Wang X, Sun L, et al. Underwater 3D deblurringgated range-intensity correlation imaging. Opt Lett. 2020;45(6):1455–8.
116. Imaging U. Strand M P. Imaging model for underwater range-gated imaging systems. In. Photography, and Visibility. 1991;1537:151–60.
117. Gillespie LF. Apparent illuminance as a function of range in gated, laser night viewing systems. J Opt Soc Am. 1966;56(7):883–7.
118. Fournier GR, Bonnier D, Forand JL, et al. Lucie ROV mounted laser imaging system. Ocean Optics XI. 1992;1750:443–52.
119. Weidemann A, Fournier GR, Forand L, et al. In harbor underwater threat detection/identification using active imaging. Photonics for Port and Harbor Security. 2005;5780:59–70.

120. Church P, Hou W, Fournier G, et al. Overview of a hybrid underwater camera system. Ocean Sensing and Monitoring VI. 2014;9111:160–6.
121. Busck J, Heiselberg H. Gated viewing and high-accuracy three-dimensional laser radar. Appl Opt. 2004;43(24):4705–10.
122. Laurenzis M, Christnacher F, Monnin D. Long-range three-dimensional active imaging with superresolution depth mapping. Opt Lett. 2007;32(21):3146–8.
123. Xinwei W, Youfu L, Yan Z. Triangular-range-intensity profile spatial correlation method for 3D super-resolution range-gated imaging. Appl Opt. 2013;52(30):7399–406.
124. McLean E, Burris H Jr, Strand M. Short-pulse range-gated optical imaging in turbid water. Appl Opt. 1995;34(21):4343–51.
125. Obzerv. Active range-gated night vision cameras [EB/OL]. (2021–01–01) [2024–03–12]. http://www.obzerv.com/en/
126. Sinotech Sensing, Gated laser surveillance [EB/OL]. (2022–09–07) [2025–06–09]. http://www.stsensing.cn
127. Molebny V, McManamon P, Steinvall O, et al. Laser radar: historical prospective—from the east to the west. Opt Eng. 2017;56(3):031220–031220.
128. Massot-Campos M, Oliver-Codina G. Optical sensors and methods for underwater 3d reconstruction. Sensors (Basel). 2015;15(12):31525–57.
129. Bright Way Vision. Driving clarity [EB/OL]. (2021–01–01) [2024–03–12]. http://www.brightwayvision.com/
130. Fengmei C, Weiqi J, Youwei H. Review of underwater opto-electrical imaging technology and equipment (I)-underwater laser range-gated imaging technology. Infrared Technology. 2011;33(2):63–9.
131. Chen Y, Shen WG, Li ZM, et al. Underwater transmission of high-dimensional twisted photons over 55 meters. PhotoniX. 2020;1:5.
132. Vision-Systems Design. Obzerv wins defense contract [EB/OL]. (2007–03–08) [2025–06–09]. https://www.vision-systems.com/cameras-accessories/article/16749781/obzerv-wins-defense-contract
133. Mariani P, Quincoces I, Haugholt KH, et al. Range-gated imaging system for underwater monitoring in ocean environment. Sustainability. 2018;11(1):162.
134. Xinwei W, Liang S, Yue Z, et al. Advances of laser range-gated three-dimensional imaging. Infrared and Laser Engineering. 2024;53(4):20240122.
135. Grönwall C, Schwering PB, Rantakokko J, et al. Future electro-optical sensors and processing in urban operations. Proc SPIE. 2013;8897:889702.
136. Shangguan M, Xia H, Wang C, et al. All-fiber upconversion high spectral resolution wind lidar using a Fabry-Perot interferometer. Opt Express. 2016;24(17):19322–36.
137. Shangguan M, Xia H, Wang C, et al. Dual-frequency doppler lidar for wind detection with a superconducting nanowire single-photon detector. Opt Lett. 2017;42(18):3541–4.
138. Halimi A, Maccarone A, McCarthy A, et al. Object depth profile and reflectivity restoration from sparse single-photon data acquired in underwater environments. IEEE Trans Comput Imaging. 2017;3(3):472–84.
139. Halimi A, Maccarone A, Lamb RA, et al. Robust and guided Bayesian reconstruction of single-photon 3D lidar data: application to multispectral and underwater imaging. IEEE Trans Comput Imaging. 2021;7:961–74.
140. Shangguan M, Yang Z, Lin Z, et al. Compact long range single-photon underwater lidar with high spatial–temporal resolution. IEEE Geosci Remote Sens Lett. 2023;20:1–5.
141. Shangguan M, Yang Z, Shangguan M, et al. Remote sensing oil in water with an all-fiber underwater single-photon Raman lidar. Appl Opt. 2023;62(19):5301–5.
142. Shangguan M, Yang Z, Lin Z, et al. Full-day profiling of a beam attenuation coefficient using a single-photon underwater lidar with a large dynamic measurement range. Opt Lett. 2024;49(3):626–9.
143. Maccarone A, Drummond K, McCarthy A, et al. Submerged single-photon lidar imaging sensor used for real-time 3D scene reconstruction in scattering underwater environments. Opt Express. 2023;31(10):16690–708.
144. Shangguan M, Li Y, Mo Y, et al. Compact underwater single-photon imaging lidar. Opt Lett. 2025;50(6):1957–60.
145. Li Z, Wu E, Pang C, et al. Multi-beam single-photon-counting three-dimensional imaging lidar. Opt Express. 2017;25(9):10189–95.
146. Shangguan M, Liang Y, Li Y, et al. Time-multiplexing single-photon imaging lidar with single-pixel detector. Appl Phys Lett. 2024;124:051104.
147. Zheng T, Shen G, Li Z, et al. Frequency-multiplexing photon-counting multi-beam LiDAR. Photonics Res. 2019;7(12):1381–5.
148. Zang Z, Li Z, Luo Y, et al. Ultrafast parallel single-pixel lidar with all-optical spectro-temporal encoding. APL Photon. 2022;7:046102.
149. Wright CW, Kranenburg C, Battista TA, et al. Depth calibration and validation of the experimental advanced airborne research lidar. EAARL-B Journal of Coastal Research. 2016;76(10076):4–17.
150. Shangguan M, Weng Z, Lin Z, et al. Day and night continuous high-resolution shallow-water depth detection with single-photon underwater lidar. Opt Express. 2023;31(26):43950–62.
151. Maccarone A, McCarthy A, Ren X, et al. Underwater depth imaging using time-correlated single-photon counting. Opt Express. 2015;23(26):33911–26.
152. Castillón M, Palomer A, Forest J, et al. State of the art of underwater active optical 3D scanners. Sensors (Basel). 2019;19(23):5161.
153. Zou K, Hao Z, Feng Y, et al. Fractal superconducting nanowire single-photon detectors working in dual bands and their applications in free-space and underwater hybrid lidar. Opt Lett. 2023;48(2):415–8.
154. Wiedwald J, Lerche R. Streak camera dynamic range optimization. High Speed Photography, Videography, and Photonics V. 1988;832:275–82.
155. Shiraga H. Review of concepts and applications of image sampling on highspeed streak cameras. Selected Papers from the 31st International Congress on High-Speed Imaging and Photonics 10328, 146–152 (2017).
156. Allgaier M, Ansari V, Eigner C, et al. Streak camera imaging of single photons at telecom wavelength. Appl Phys Lett. 2018;112:031110.

157. Williamson S. Millimeter depth resolution streak camera-based lidar. Conference on Lasers and Electro-Optics, D. Pinnow and P. Moulton, eds., Vol. 7 of OSA Technical Digest TUW3 (1988).
158. Knight F, Klick D, Ryan-Howard D, et al. Three-dimensional imaging using a single laser pulse. Proc SPIE. 1989;1103:174–89.
159. Knight FK, Klick DI, Ryan-Howard DP, et al. Visible laser radar: range tomography and angle-angle-range detection. Opt Eng. 1991;30(1):55–65.
160. Gelbart A, Redman BC, Light RS, et al. Flash lidar based on multiple-slit streak tube imaging lidar. SPIE Proc. 2002;4723:9–18.
161. Gelbart A, Weber C, Bybee-Driscoll S, et al. Flash lidar data collections in terrestrial and ocean environments. SPIE Proc. 2003;5086:27–38.
162. Gleckler AD. Multiple-slit streak tube imaging lidar (MS-STIL) applications. Laser Radar Technology and Applications V. 2000;035:266–78.
163. McLean JW. High-resolution 3D underwater imaging. Airborne and In-Water Underwater Imaging. 1999;3761:10–9.
164. Redman B, Griffis A, Schibley E. Streak tube imaging lidar (STIL) for 3-D imaging of terrestrial targets. Proc. of 2000 Meeting of the MSS Specialty Group on Active EO Systems 11–13 (2000).
165. Imaki M, Ochimizu H, Tsuji H, et al. Underwater three-dimensional imaging laser sensor with 120-deg wide-scanning angle using the combination of a dome lens and coaxial optics. Opt Eng. 2016;56(3):031212.
166. Zhao BS, Chen M. The application of MS-streak tube in three-dimensional LiDAR system. Acta Photon Sin. 2004;33(12):1425.
167. Wei J, Wang Q, Sun J, et al. High-resolution imaging of a long-distance target with a single-slit streak-tube lidar. J Russ Laser Res. 2010;31:307–12.
168. Yang H, Wu L, Wang X, et al. Signal-to-noise performance analysis of streak tube imaging lidar systems. I. Cascaded model. Appl Opt. 2012;51(36):8825–35.
169. Gao J, Sun J, Wang Q. Experiments of Ocean surface waves and underwater target detection imaging using a slit streak tube imaging lidar. Optik. 2014;125(18):5199–201.
170. Ye G, Fan R, Chen Z, et al. Range accuracy analysis of streak tube imaging lidar systems. Opt Commun. 2016;360:7–14.
171. Chen Z, Fan R, Ye G, et al. Depth resolution improvement of streak tube imaging lidar system using three laser beams. Chin Opt Lett. 2018;16(4):041101.
172. Luo T, Fan R, Chen Z, et al. Deblurring streak image of streak tube imaging lidar using wiener deconvolution filter. Opt Express. 2019;27(26):37541–51.
173. Li G, Zhou Q, Xu G, et al. Lidar-radar for underwater target detection using a modulated sub-nanosecond Q-switched laser. Opt Laser Technol. 2021;142:107234.
174. Guo S, Li W, Lai Z, et al. Differential optical-path approach to improving the performance of Multiple-Slit Streak-Tube Imaging LiDAR. Measurement. 2021;172:108947.
175. Li W, Guo S, Zhai Y, et al. Target classification of multislit streak tube imaging lidar based on deep learning. Appl Opt. 2021;60(32):8809–17.
176. Yan Y, Wang H, Dong Z, et al. Extracting suburban residential building zone from airborne streak tube imaging lidar data. Measurement. 2022;199:111488.
177. Yan Y, Wang H, Song B, et al. Airborne streak tube imaging lidar processing system: a single echo fast target extraction implementation. Remote Sens. 2023;15(4):1128.
178. Fang M, Xue Y, Ji C, et al. Development of a large-field streak tube for underwater imaging lidar. Appl Opt. 2022;61(25):7401–8.
179. Fang M, Qiao K, Yin F, et al. Underwater 4D imaging quality enhancement of streak tube imaging lidar at extremely low SNR. Appl Opt. 2025;64(14):3880–9.
180. Feng F, Liu B, Wu G J. A coaxial transceiver underwater synchronous scanning imaging system and method: CN Patent CN115407362B[P]. 2023–02–14.
181. Liu B, Wu G J, Hang D D. Laser scanning synchronous control system and control method based on polyhedral rotating mirror: CN Patent CN115343688B[P]. 2024–04–12.
182. Liu B, Wu G J. Distance selection gating ranging method based on streak tube camera: CN Patent CN115343718B[P]. 2024–04–12.
183. Li X, An H, Li G, et al. Streaknet-arch: an anti-scattering network-based architecture for underwater carrier lidar-radar imaging. IEEE Trans Image Process. 2025;34:4357–70.
184. Cui Z, Tian Z, Zhang Y, et al. Research on the underwater target imaging based on the streak tube laser lidar. Young Scientists Forum. 2018;2017(10710):838–44.
185. Li W, Guo S, Zhai Y, et al. Denoising of the multi-slit streak tube imaging lidar system using a faster non-local mean method. Appl Opt. 2021;60(34):10520–8.
186. Fang M, Qiao K, Yin F, et al. Streak tube imaging lidar with kilohertz laser pulses and few-photons detection capability. Opt Express. 2024;32(11):19042–56.
187. Areté Associates & Fugro. PILLS/RAMMS Bathymetric LiDAR: System Overview [EB/OL]. (2024–04–01) [2025–06–10]. https://arete.com/products/pills/
188. Strekalov D, Sergienko A, Klyshko D, et al. Observation of two-photon "ghost" interference and diffraction. Phys Rev Lett. 1995;74(18):3600.
189. Pittman T, Strekalov D, Klyshko D, et al. Two-photon geometric optics. Phys Rev A. 1996;53(4):2804.
190. Gatti A, Brambilla E, Bache M, et al. Correlated imaging, quantum and classical. Phys Rev A. 2004;70(1):013802.
191. Katkovnik V, Astola J. Compressive sensing computational ghost imaging. J Opt Soc Am A Opt Image Sci Vis. 2012;29(8):1556–67.
192. Sun Z, Tuitje F, Spielmann C. Toward high contrast and high-resolution microscopic ghost imaging. Opt Express. 2019;27(23):33652–61.
193. Zhang X, Gao J, Gan Y, et al. Different channels to transmit information in scattering media. PhotoniX. 2023;4:10.

194. Park J, Gao L. Cascaded compressed-sensing single-pixel camera for high-dimensional optical imaging. PhotoniX. 2024;5:37.
195. Zeng F, Bian Y, Song K, et al. Photon-level single-pixel wavefront imaging through turbid underwater environment. APL Photonics. 2025;10:060805.
196. Pittman TB, Shih Y, Strekalov D, et al. Optical imaging by means of two-photon quantum entanglement. Phys Rev A. 1995;52(5):3429.
197. Valencia A, Scarcelli G, D'Angelo M, et al. Two-photon imaging with thermal light. Phys Rev Lett. 2005;94(6):063601.
198. Ferri F, Magatti D, Lugiato LA, et al. Differential ghost imaging. Phys Rev Lett. 2010;104:253603.
199. Sun B, Welsh SS, Edgar MP, et al. Normalized ghost imaging. Opt Express. 2012;20(15):16892–901.
200. Donoho DL. Compressed sensing. IEEE Trans Inf Theory. 2006;52(4):1289–306.
201. Li C, An Efficient augmented Lagrangian method with applications to total variation minimization. Ph.D. dissertation, Rice University. Dissertations & Theses GradWorks, 1486057 (2010).
202. Duarte MF, Davenport MA, Takhar D, et al. Single-pixel imaging via compressive sampling. IEEE Signal Process Mag. 2008;25(2):83–91.
203. Katz O, Bromberg Y, Silberberg Y. Compressive ghost imaging. Appl Phys Lett. 2009;95:131110.
204. Aβmann M, Bayer M. Compressive adaptive computational ghost imaging. Sci Rep. 2013;3(1):1545.
205. Yu W, Li M, Yao X, et al. Adaptive compressive ghost imaging based on wavelet trees and sparse representation. Opt Express. 2014;22(6):7133–44.
206. Horisaki R, Takagi R, Tanida J. Learning-based imaging through scattering media. Opt Express. 2016;24(13):13738–43.
207. Wu G, Nowotny T, Zhang Y, et al. Artificial neural network approaches for fluorescence lifetime imaging techniques. Opt Lett. 2016;41(11):2561–4.
208. Sinha A, Lee J, Li S, et al. Lensless computational imaging through deep learning. Optica. 2017;4(9):1117–25.
209. Lyu M, Wang W, Wang H, et al. Deep learning-based ghost imaging. Sci Rep. 2017;7(1):17865.
210. He Y, Wang G, Dong G, et al. Ghost imaging based on deep learning. Sci Rep. 2018;8(1):6469.
211. Shimobaba T, Endo Y, Nishitsuji T, et al. Computational ghost imaging using deep learning. Opt Commun. 2018;413:147–51.
212. Chen Y, Tian T, Lu X, et al. Attention-enhanced computational ghost imaging. SCIENCE CHINA Inf Sci. 2025;68(6):297–306.
213. Liu S, Meng X, Yin Y, et al. Computational ghost imaging based on an untrained neural network. Opt Lasers Eng. 2021;147:106744.
214. Wang F, Wang C, Deng C, et al. Single-pixel imaging using physics enhanced deep learning. Photonics Res. 2021;10(1):104–10.
215. Wang F, Wang C, Chen M, et al. Far-field super-resolution ghost imaging with a deep neural network constraint. Light Sci Appl. 2022;11(1):1.
216. Zhang X, Deng C, Wang C, et al. VGENNET: variable generative prior enhanced single pixel imaging. ACS Photonics. 2023;10(7):2363–73.
217. Podell D, English Z, Lacey K, et al. SDXL: Improving latent diffusion models for highresolution image synthesis. arXiv preprint arXiv:2307.01952 (2023).
218. Achiam J, Adler S, Agarwal S, et al. GPT-4 technical report. arXiv preprint arXiv:2303.08774 (2023).
219. Chen Y, An H, Sun Z, et al. Large model enhanced computational ghost imaging. Sci China Technol Sci. 2025;68(11):2120403.
220. Gonz´alez-Sabbagh, S. P., Robles-Kelly, A. A survey on underwater computer vision. ACM Computing Surveys 55(13s), 1–39 (2023).
221. Raveendran S, Patil MD, Birajdar GK. Underwater image enhancement: a comprehensive review, recent trends, challenges and applications. Artif Intell Rev. 2021;54:5413–67.
222. Zhou J, Liu Q, Jiang Q, et al. Underwater camera: Improving visual perception via adaptive dark pixel prior and color correction. International Journal of Computer Vision, 1–19 (2023).
223. Kang Y, Jiang Q, Li C, et al. A perception-aware decomposition and fusion framework for underwater image enhancement. IEEE Trans Circuits Syst Video Technol. 2022;33(3):988–1002.
224. Qi Q, Li K, Zheng H, Gao, et al. Sguie-net: Semantic attention guided underwater image enhancement with multi-scale perception. IEEE Transactions on Image Processing 31, 6816–6830 (2022).
225. Liu B, Liu Z, Men S, et al. Underwater hyperspectral imaging technology and its applications for detecting and mapping the seafloor: a review. Sensors. 2020;20(17):4962.
226. Montes-Herrera JC, Cimoli E, Cummings V, et al. Underwater hyperspectral imaging (UHI): a review of systems and applications for proximal seafloor ecosystem studies. Remote Sens. 2021;13(17):3451.
227. Dumke I, Purser A, Marcon Y, et al. Underwater hyperspectral imaging as an in situ taxonomic tool for deep-sea megafauna. Sci Rep. 2018;8(1):12860.
228. Mills MS, Ungermann M, Rigot G, et al. Assessment of the utility of underwater hyperspectral imaging for surveying and monitoring coral reef ecosystems. Sci Rep. 2023;13(1):21103.
229. Dumke I, Ludvigsen M, Ellefmo SL, et al. Underwater hyperspectral imaging using a stationary platform in the transatlantic geotraverse hydrothermal field. IEEE Trans Geosci Remote Sens. 2018;57(5):2947–62.
230. Dumke I, Nornes SM, Purser A, et al. First hyperspectral imaging survey of the deep seafloor: high-resolution mapping of manganese nodules. Remote Sens Environ. 2018;209:19–30.
231. Mogstad AA, Johnsen G, Ludvigsen M. Shallow-water habitat mapping using underwater hyperspectral imaging from an unmanned surface vehicle: a pilot study. Remote Sens. 2019;11(6):685.
232. Ødegård Ø, Mogstad AA, Johnsen G, et al. Underwater hyperspectral imaging: a new tool for marine archaeology. Appl Opt. 2018;57(12):3214–23.
233. Guo Y, Song H, Liu H, et al. Model-based restoration of underwater spectral images captured with narrowband filters. Opt Express. 2016;24(12):13101–20.

234. Song H, Mehdi SR, Wu C, et al. Underwater spectral imaging system based on liquid crystal tunable filter. J Mar Sci Eng. 2021;9(11):1206.
235. Lu F, Gao X, Ma J, et al. Intelligent marine detection based on spectral imaging and neural network modeling. Ocean Eng. 2024;310:118640.
236. Zawada D G. The application of a novel multispectral imaging system to the in vivo study of flourescent compounds in selected marine organisms. PhD Thesis, Citeseer (2002).
237. Gleason A, Reid R, Voss K. Automated classification of underwater multispectral imagery for coral reef monitoring. Oceans. 2007;2007:1–8.
238. Wu C, Shentu Y, Chaofan C, et al. Development of an underwater multispectral imaging system based on narrowband color filters. OCEANS 2018 MTS/IEEE Charleston, 1–6 (2018).
239. Liu H, Sticklus J, Koeser K, et al. Tulumis-a tunable LED-based underwater multispectral imaging system. Opt Express. 2018;26(6):7811–28.
240. Johnsen G. Underwater Hyperspectral Imaging. US8502974B2, August 2013.US patent granted on August 6, 2013. Adjusted expiration: 2029–12–17.
241. Johnsen G, Volent Z, Dierssen H, et al. Underwater hyperspectral imagery to create biogeochemical maps of seafloor properties. Subsea Optics and Imaging. 2013;508–535:536e–40e.
242. Johnsen G, Ludvigsen M, Sørensen A, et al. The use of underwater hyperspectral imaging deployed on remotely operated vehicles-methods and applications. IFAC-PapersOnLine. 2016;49(23):476–81.
243. Chennu A, Färber P, De'ath G, et al. A diver-operated hyperspectral imaging and topographic surveying system for automated mapping of benthic habitats. Sci Rep. 2017;7:7122.
244. Nevala NE, Baden T. A low-cost hyperspectral scanner for natural imaging and the study of animal colour vision above and under water. Sci Rep. 2019;9(1):10799.
245. Bai H, Xue Q, Hao X, et al. Underwater hyperspectral imaging system with dual-scanning mode. Appl Opt. 2022;61(15):4226–37.
246. Xue Q, Tian Z, Yang B, et al. Underwater hyperspectral imaging system using a prism–grating–prism structure. Appl Opt. 2021;60(4):894–900.
247. Song H, Mehdi SR, Wan Q, et al. Compact staring-type underwater spectral imaging system utilizing knearest neighbor-based interpolation for spectral reconstruction. Opt Laser Technol. 2025;181:111880.
248. Kohnen W. Human exploration of the deep seas: fifty years and the inspiration continues. Mar Technol Soc J. 2009;43(5):42–62.
249. Cui W. Development of the Jiaolong deep manned submersible. Mar Technol Soc J. 2013;47(3):37–54.
250. Liu F, Tang H, Qin Y, et al. Review on fault diagnosis of unmanned underwater vehicles. Ocean Eng. 2022;243:110290.
251. Busby R F. Manned Submersibles. Office of the Oceanographer of the Navy (1976).
252. Takacs G. Electrical Submersible Pumps Manual: Design, Operations, and Maintenance. Gulf professional publishing (2017).
253. Su Z, Xiang Y, Li D, et al. SPH-DEM modeling of cablecontrolled rovs: Underwater mobility and path planning. Ocean Eng. 2024;292:116623.
254. Altamimi R, El-Genk MS. Design and analyses of miniature, submersible annular linear induction pump for test loops supporting development of advanced nuclear reactors. Nucl Sci Eng. 2024;198(8):1620–44.
255. Jones G M. The Development of Nuclear Propulsion in the Royal Navy, 1946–1975. Springer (2022).
256. Cornwall W. Alvin, the iconic submersible, plunges deeper than ever. Science (New York, NY). 2024;384(6698):833–4.
257. Wegner E, Tonioli F, Cabral D. Underwater trails: A new possibility of marine tourism. Journal of Coastal Research, 990–993 (2006).
258. Cui W, Liu F, Hu Z, et al. On 7,000 m sea trials of the manned submersible jiaolong. Mar Technol Soc J. 2013;47(1):67–82.
259. Humphris S E. A phased engineering program to build a new 6500-m research submersible for the US scientific community: The new Alvin. NSF Award Number 0433409. Directorate for Geosciences 4(433409), 33409 (2004).
260. Iwai Y, Nakanishi T, Takahashi K. Sea trials and supporting technologies of manned submersible "Shinkai 6500". Intervention Sous-Marine ISM 90, Toulon (France) (1990).
261. Jiang H, Zhang W. "Assistant or replacement?" a socio-technical exploration of robots in underwater archaeology. ACM/IEEE International Conference on Human-Robot Interaction (HRI) 132–141 (2025).
262. Sagalevitch A. From the bathyscaph trieste to the submersibles mir. Mar Technol Soc J. 2009;43(5):79–86.
263. Dalhatu A A, Sa'ad A M, Azevedo R, et al. Remotely operated vehicle taxonomy and emerging methods of inspection, maintenance, and repair operations: An overview and outlook. Journal of Offshore Mechanics and Arctic Engineering 145(2), 020801 (2023).
264. Patel S, Abdellatif F, Alsheikh M, et al. Multi-robot system for inspection of underwater pipelines in shallow waters. Int J Intell Robot Appl. 2024;8(1):14–38.
265. Dalhatu AA, Azevedo RC, Udebhulu OD, et al. Recent developments of remotely operated vehicle in the oil and gas industry. Holos. 2021;3:1–18.
266. Heinrich M, LeHardy P K. Record breaking deep ocean salvage operations. OCEANS 2021: San Diego–Porto 1–6 (2021).
267. Gomez-Ibanez D, Taylor C L, Naklicki V, et al. Pressuretolerant battery and power systems for the nereid under ice hybrid ROV: Design and field experience. OCEANS 2024-Halifax 1–9 (2024).
268. Brainard J. First complete map of fruit fly brain circuitry unveiled. Science. 2024;386(6717):1–2.
269. Fontão RAS. Navegação de um veículo robótico subaquático em ambiente estruturado baseada em visão monocular. Aveiro: Universidade de Aveiro; 2021.
270. Hai H, Tao J, Xinyu B, et al. Object detection and multiple objective optimization manipulation planning for underwater autonomous capture in oceanic natural aquatic farm. J Field Robotics. 2025;42:e22507.

271. Hanssen P. The seahorse concept for automated subsea operations. EAGE Annual Conference & Exhibition. 2022;2022:1–5.
272. Haonan S, Lei W, Dejun L. Analysis of development status and key technologies of deep-sea working type of remotely operated vehicles. Shipbuilding of China. 2024;65(6):130–44.
273. Díez-García IP, Gómez-Ballesteros M, Sánchez-Delgado F, et al. 3D scanning bathymetry applied for assessment and monitoring of protected marine habitats: El Cachucho case study. Madrid: Sede Central, Instituto Español de Oceanografía (IEO); 2020.
274. Wheat CG, Fournier T, Monahan K, et al. Take the plunge: a stem camp centered on seafloor science. Current: The Journal of Marine Education. 2018;31(2):2–8.
275. Inoue T, Shiosawa T, Takagi K. Dynamic motion of crawler-type ROV. IEEE Symposium on Underwater Technology and Workshop on Scientific Use of Submarine Cables and Related Technologies, 1–6 (2011).
276. Hotta S, Mitsui Y, Suka M, et al. Lightweight underwater robot developed for archaeological surveys and excavations. Robomech J. 2023;10(1):2.
277. Leonard J J, Bahr A. Autonomous underwater vehicle navigation. Springer handbook of ocean engineering, 341–358 (2016).
278. Hyakudome T. Design of autonomous underwater vehicle. Int J Adv Robot Syst. 2011;8(1):9.
279. Yang Y, Xiao Y, Li T. A survey of autonomous underwater vehicle formation: performance, formation control, and communication capability. IEEE Commun Surv Tutor. 2021;23(2):815–41.
280. Lin YH, Yu CM, Wu IC, et al. The depth-keeping performance of autonomous underwater vehicle advancing in waves integrating the diving control system with the adaptive fuzzy controller. Ocean Eng. 2023;268:113609.
281. Shome SN, Nandy S, Pal D, et al. Development of modular shallow water AUV: issues & trial results. Journal of The Institution of Engineers (India): Series C. 2012;93:217–28.
282. Xia S, Zhou X, Shi H, et al. A fault diagnosis method based on attention mechanism with application in Qianlong-2 autonomous underwater vehicle. Ocean Eng. 2021;233:109049.
283. Wang Y, Wang Y, Zhang T, et al. Bayesian network-based security decision-making method for the full-ocean-depth "Wukong" AUV. Proceedings of the Institution of Mechanical Engineers, Part M: Journal of Engineering for the Maritime Environment. 2023;237(1):206–14.
284. Zhang B, Xu W, Lu C, et al. Review of low-loss wireless power transfer methods for autonomous underwater vehicles. IET Power Electron. 2022;15(9):775–88.
285. Yang S, Liu P, Lim T H. Iot-based underwater robotics for water quality monitoring in aquaculture: A survey. International Conference on Robot Intelligence Technology and Applications, 32–42 (2023).
286. Yamamoto I, Aoki T, Tsukioka S, et al. Fuel cell system of AUV "Urashima". Oceans' 04 MTS/IEEE Techno-Ocean'04 (IEEE Cat. No.04CH37600) 3, 1732–1737 (2004).
287. Cao Z, Guo J, Liu J, et al. Cooperative operation mode and target recognition technology for unmanned surface vessel and unmanned underwater vehicle. International Conference on Mechatronic Engineering and Artificial Intelligence (MEAI 2024) 13555, 801–806 (2025).
288. Petritoli E, Leccese F. Autonomous underwater glider: a comprehensive review. Drones. 2024;9(1):21.
289. Wang Y, Bulger C, Thanyamanta W, et al. A backseat control architecture for a slocum glider. J Mar Sci Eng. 2021;9(5):532.
290. Bennett JS, Stahr FR, Eriksen CC, et al. Assessing seaglider model-based position accuracy on an acoustic tracking range. J Atmos Ocean Technol. 2021;38(6):1111–23.
291. Yuan S, Li Y, Bao F, et al. Marine environmental monitoring with unmanned vehicle platforms: present applications and future prospects. Sci Total Environ. 2023;858:159741.
292. Constantinoiu LF, Quaresma L, Rusu E. Oceanographic environmental assessment using underwater gliders. JMTE. 2022;2:12–5.
293. Busquets J, Mataix DB, Mataix JVB, et al. Advances in the development of a new medium depth underwater glider. Instrumentation viewpoint. 2024;23:88–9.
294. Low K. Current and future trends of biologically inspired underwater vehicles. Defense Science Research Conference and Expo (DSR) 1–8 (2011).
295. Anand A, Bharath MY, Sundaravadivel P, et al. Ondevice intelligence for AI-enabled bio-inspired autonomous underwater vehicles (AUVs). IEEE Access. 2024;12:51982–94.
296. Costa D, Palmieri G, Palpacelli M C, et al. Design of a bio-inspired underwater vehicle. 12th IEEE/ASME International Conference on Mechatronic and Embedded Systems and Applications (MESA) 1–6 (2016).
297. Nichols R K, Ryan J, Mumm H C, et al. UUV integrated autonomous missions & drone management. Unmanned Vehicle Systems & Operations on Air, Sea, Land (2020).
298. Transeth AA, Leine RI, Glocker C, et al. Snake robot obstacle-aided locomotion: modeling, simulations, and experiments. IEEE Trans Robot. 2008;24(1):88–104.
299. Yangwei W, Zhenlong W, Jian L. Current situation and development of micro underwater biomimetic robot. Small & Special Electrical Machines. 2010;38(12):66–9.
300. Cao Q, Wang R, Zhang T, et al. Hydrodynamic modelling and parameter identification of a bionic underwater vehicle: Robdact. Cyborg and Bionic Systems (2022).
301. Yiming H. Research on hydrodynamic performance of flexible bionic tail fin. Master's thesis, Harbin Institute of Technology (2024).
302. Bowen A D, Yoerger D R, Taylor C, et al. The Nereus hybrid underwater robotic vehicle for global ocean science operations to 11,000 m depth. OCEANS 1–10 (2008).
303. Brignone L, Raugel E, Opderbecke J, et al. First sea trials of HROV the new hybrid vehicle developed by IFREMER. Oceans 2015-genova, 1–7 (2015).
304. Momma H, Watanabe M, Hashimoto K, et al. Loss of the full ocean depth ROV Kaiko-part 1: ROV Kaiko-a review. ISOPE International Ocean and Polar Engineering Conference, (2004).
305. Zeng J, Li S, Tang Y, et al. The application of polar-ARV in the fourth Chinese national arctic expedition. OCEANS'11 MTS/IEEE KONA, 1–5 (2011).

306. Tang Y, Wang J, Lu Y, et al. Parametric design method and experimental research on Haidou full-depth ocean autonomous and remotely-operated vehicle. Robot. 2019;41(6):697–705.
307. The NEL Type III Deep-sea camera. San Diego, CA: U.S. Navy Electronics Laboratory, Research and Developmental Report 768 (1957).
308. Edwards MH, Smith MO, Fornari DJ. CCD digital camera maps the east Pacific Rise. Eos Trans Am Geophys Union. 1992;73(31):329–33.
309. Anisimov I, Rimskii-Korsakov N, Tronza S N. Bottom relief and underwater objects visual deep-water observations technologies development. International Journal of Applied and Fundamental Research, 149–153 (2019).
310. Goldsborough R, Simpson R, Allen B, et al. A high resolution electronic still camera with full ocean depth housing. Oceans' 97. MTS/IEEE Conference Proceedings 1, 528 (1997).
311. Hardy K, Olsson M, Yayanos A A, et al. Deep ocean visualization experimenter (dove): low-cost 10 km camera and instrument platform. OCEANS'02 MTS/IEEE 4, 2390–2394 (2002).
312. Giddens J, Turchik A, Goodell W, et al. The National Geographic Society deep-sea camera system: a low-cost remote video survey instrument to advance biodiversity observation in the deep ocean. Front Mar Sci. 2021;7:601411.
313. Barclay D R. Depth profiling ambient noise in the deep ocean. PhD Thesis, UC San Diego (2011).
314. Kwasnitschka T, Koeser K, Sticklus J, et al. DeepSurveyCam—a deep ocean optical mapping system. Sensors. 2016;16(2):164.
315. Haibin Y, Huadong P, Wengli C, et al. Key technology research and application of deep-sea ultra-compact full-color high-frame HD camera. Technical appraisal, Hangzhou Dianzi University, Zhejiang Dahua Technology Co., Ltd., Hangzhou Hanlu Ocean Technology Co., Ltd. (2023). Appraisal Date: 2023–01–10
316. DEEPSEA POWER & LIGHT: Seacam, Optim. Accessed: 2022–03–28. https://www.deepsea.com/optimseacam/.
317. DEEPSEA POWER & LIGHT: Seacam, Super Wide-i. Accessed:2022–03–28.https://www.deepsea.com/super-widei-seacam/.
318. DEEPSEA POWER & LIGHT: Seacam, Vertex. Accessed: 2022–03–28. https://www.deepsea.com/vertex-seacam/.
319. SULIS SUBSEA: C600. Accessed: 2022–03–28. https://www.sulissubsea.com/sulis-line.
320. Xiao J, Sun Z, An H, et al. Optical image processing and applications empowered by vision-language models. iOptics. 2025;1(1):100003.
321. Erkan U, Thanh DNH, Hieu LM, et al. An iterative mean filter for image denoising. IEEE Access. 2019;7:167847–59.
322. Veni N, Manjula J. Gaussian denoising by time domain and frequency domain filters for MRI brain images. 2022 IEEE IAS Global Conference on Emerging Technologies, Arad, Romania, 817–821 (2022).
323. Li L, Song M, Zhang Q. et al. Hyperspectral denoising via global variation and local structure low-rank model. IEEE Transactions on Geoscience and Remote Sensing 61, 1–13 (2023).
324. Zhang H, Chen H, Yang G, et al. Lr-net: low-rank spatial-spectral network for hyperspectral image denoising. IEEE Trans Image Process. 2021;30:8743–58.
325. Sheng Z, Liu X, Cao SY, et al. Frequency-domain deep guided image denoising. IEEE Trans Multimedia. 2022;25:6767–81.
326. Morovic J, Luo MR. The fundamentals of gamut mapping: a survey. J Imaging Sci Technol. 2001;45(3):283–90.
327. Van De Weijer J, Gevers T, Gijsenij A. Edge-based color constancy. IEEE Trans Image Process. 2007;16(9):2207–14.
328. Hu Y, Wang B, Lin S. Fc4: Fully convolutional color constancy with confidence-weighted pooling. Proceedings of the IEEE conference on computer vision and pattern recognition. (2017).
329. Le, H M, Price B, Cohen S, et al. GamutMLP: a lightweight MLP for color loss recovery. Proceedings of the IEEE/CVF Conference on Computer Vision and Pattern Recognition. 18268–18277 (2023).
330. Zhang W, Li Z, Zhang L, et al. SPnet: semantic preserving network with semantic constraint and non-semantic calibration for color constancy. Neurocomputing. 2024;596:127947.
331. Shan Qi, Jia J, Agarwala A. High-quality motion deblurring from a single image. ACM Trans Graph. 2008;27(3):1–10.
332. Zhang H, Dai Y, Li H, et al. Deep stacked hierarchical multi-patch network for image deblurring. Proceedings of the IEEE/CVF Conference on Computer Vision and Pattern Recognition. 5978–5986 (2019).
333. Mehri A, Ardakani P B, Sappa A D. MPRNet: Multi-path residual network for lightweight image super resolution. Proceedings of the IEEE/CVF Winter Conference on Applications of Computer Vision. 2704–2713 (2021).
334. Zhang K, Luo W, Zhong Y, et al. Deblurring by realistic blurring. 2020 IEEE/CVF Conference on Computer Vision and Pattern Recognition, Seattle, WA, USA, 2734–2743 (2020).
335. He K, Sun J, Tang X. Single image haze removal using dark channel prior. 2009 IEEE Conference on Computer Vision and Pattern Recognition, Miami, FL, USA, 1956–1963 (2009).
336. Cai B, Xu X, Jia K, et al. Dehazenet: an end-to-end system for single image haze removal. IEEE Trans Image Process. 2016;25(11):5187–98.
337. He Z, Patel V M. Densely connected pyramid dehazing network. 2018 IEEE/CVF Conference on Computer Vision and Pattern Recognition, Salt Lake City, UT, USA, 3194–3203 (2018).
338. Ren W, Pan J, Zhang H, et al. Single image dehazing via multi-scale convolutional neural networks. Int J Comput Vision. 2020;128:240–59.
339. Li B, Gou Y, Liu JZ, et al. Zero-shot image dehazing. IEEE Trans Image Process. 2020;29:8457–66.
340. Gandelsman Y, Shocher A, Irani M. "Double-DIP": Unsupervised image decomposition via coupled deep-image-priors. 2019 IEEE/CVF Conference on Computer Vision and Pattern Recognition, Long Beach, CA, USA, 11026–11035 (2019).
341. Yeh CH, Huang CH, Kang LW. Multi-scale deep residual learning-based single image haze removal via image decomposition. IEEE Trans Image Process. 2019;29:3153–67.
342. Li J, Skinner KA, Eustice RM, et al. WaterGAN: unsupervised generative network to enable real-time color correction of monocular underwater images. IEEE Robotics and Automation Letters. 2017;3(1):387–94.
343. Alsakar YM, Sakr NA, El-Sappagh S, et al. Underwater image restoration and enhancement: a comprehensive review of recent trends, challenges, and applications. Vis Comput. 2024;41(6):3735–83.
344. Su J, Xu B, Yin H. A survey of deep learning approaches to image restoration. Neurocomputing. 2022;487:46–65.

345. Howard JM, Palm KJ, Wang Q, et al. Water-induced and wavelength-dependent light absorption and emission dynamics in triple-cation halide perovskites. Advanced Optical Materials. 2021;9(18):2100904.
346. Zhang X, Hu L. Light scattering by pure water and seawater: recent development. J Remote Sens. 2021;2021:1–18.
347. Zhou J, Yang T, Chu W, et al. Underwater image restoration via backscatter pixel prior and color compensation. Eng Appl Artif Intell. 2022;111:104785.
348. Song Y, Nakath D, She M, et al. Optical imaging and image restoration techniques for deep ocean mapping: a comprehensive survey. PFG – Journal of Photogrammetry, Remote Sensing and Geoinformation Science. 2022;90(3):243–67.
349. Zhou J, Wang Y, Li C, et al. Multicolor light attenuation modeling for underwater image restoration. IEEE J Ocean Eng. 2023;48(4):1322–37.
350. Ding Y, Li K, Mei H, et al. Watermono: teacher-guided anomaly masking and enhancement boosting for robust underwater self-supervised monocular depth estimation. IEEE Trans Instrum Meas. 2025;74:1–14.
351. Xiang D, He D, Sun H, et al. HCMPE-Net: an unsupervised network for underwater image restoration with multi-parameter estimation based on homology constraint. Opt Laser Technol. 2025;186:112616.
352. Hu H, Huang Y, Li X, et al. UCRNet: underwater color image restoration via a polarization-guided convolutional neural network. Front Mar Sci. 2022;9:104123.
353. Sun Y, Zhang J, Liang R. Color polarization demosaicking by a convolutional neural network. Opt Lett. 2021;46(17):4338–41.
354. Schechner YY, Narasimhan SG, Nayar SK. Polarization-based vision through haze. Appl Opt. 2003;42(3):511–25.
355. Liu P, Chen S, He W, et al. Enhanced U-net for underwater laser range-gated image restoration: boosting underwater target recognition. J Mar Sci Eng. 2025;13(4):803.
356. Wang C, Sun T, Wang T, et al. Multi-PSF fusion in image restoration of range-gated systems. Opt Laser Technol. 2018;103:219–25.
357. Chua S Y, Chew K W, Guo N, et al. Three-dimensional (3D) reconstruction of range-gated imaging. IEEE 7th International Conference on Photonics (ICP) 1–3 (2018).
358. Bian L, Song H, Peng L, et al. High-resolution single-photon imaging with physics-informed deep learning. Nat Commun. 2023;14(1):5536.
359. Tachella J, Altmann Y, Mellado N, et al. Real-time 3D reconstruction from single-photon lidar data using plug-and-play point cloud denoisers. Nat Commun. 2019;10(1):4980.
360. Chen S, Su X, Zhang Z, et al. Fast and robust restoration of single-photon 3D data using parameterized kernel. IEEE J Sel Top Quantum Electron. 2024;30(1):8200208.
361. Tsumori M, Nagai S, Harakawa R, et al. Restoration of minute light emissions observed by streak camera based on N-cup method. Asia-Pacific Signal and Information Processing Association Annual Summit and Conference (APSIPA ASC) 1380–1384 (2019).
362. Lei X, Shahid H, Wu S. A novel algorithm to improve image reconstruction quality for 2D streak camera. Nucl Instrum Methods Phys Res A. 2021;991:165023.
363. Oguzhan K, Ranc L, Verra L, et al. A decomposition algorithm for streak camera data. J Instrum. 2024;19(4):P04005.
364. Gao Z, Cheng X, Yue J, et al. Extendible ghost imaging with high reconstruction quality in strong scattering medium. Opt Express. 2022;30(25):45759.
365. Zhang L, Bian Z, Ye H, et al. Research on photon-level ghost imaging restoration based on deep learning. Opt Commun. 2022;504:127479.
366. Yang X, Yu Z, Jiang P, et al. Deblurring ghost imaging reconstruction based on underwater dataset generated by few-shot learning. Sensors. 2022;22(16):6161.
367. Qian J, Li J, Wang Y, et al. Underwater image recovery method based on hyperspectral polarization imaging. Opt Commun. 2021;484:126691.
368. Li Q, Li J, Li T, et al. A joint framework for underwater hyperspectral image restoration and target detection with conditional diffusion model. IEEE J Sel Top Appl Earth Observ Remote Sens. 2024;17:17263–77.
369. Ferrera M, Arnaubec A, Istenic K, et al. Hyperspectral 3D mapping of underwater environments. IEEE/CVF International Conference on Computer Vision Workshops (ICCVW) 3696–3705 (2021).
370. Yao B, Xiang J. Underwater image dehazing using modified dark channel prior. Chinese Control and Decision Conference (CCDC) 5792–5797 (2018).
371. Zhang T, Su H, Fan B, et al. Underwater image enhancement based on red channel correction and improved multiscale fusion. IEEE Trans Geosci Remote Sens. 2024;62:1–20.
372. Chiang JY, Chen YC. Underwater image enhancement by wavelength compensation and dehazing. IEEE Trans Image Process. 2012;21(4):1756–69.
373. Chen W, Lei Y, Luo S, et al. UWFormer: underwater image enhancement via a semi-supervised multi-scale transformer. International Joint Conference on Neural Networks (IJCNN) 1–8 (2024).
374. Abin D, Thepade S D, Maitre A R. Improved Water-Net model for underwater image enhancement. 14th International Conference on Materials Processing and Characterization 2023. AIP Publishing, 070002 (2024).
375. Islam MJ, Xia Y, Sattar J. Fast underwater image enhancement for improved visual perception. IEEE Robot Autom Lett. 2020;5(2):3227–34.
376. Yan H, Zhang Z, Xu J, et al. UW-CycleGAN: model-driven CycleGAN for underwater image restoration. IEEE Trans Geosci Remote Sens. 2023;61:1–17.
377. Krull A, Buchholz T-O, Jug F. Noise2Void – learning denoising from single noisy images. IEEE/CVF Conference on Computer Vision and Pattern Recognition (CVPR) 2124–2132 (2019).
378. Lei Y, Yu J, Dong Y, et al. UIE-Unfold: deep unfolding network with color priors and vision transformer for underwater image enhancement. IEEE 11th International Conference on Data Science and Advanced Analytics (DSAA) 1–10 (2024).
379. Guo X, Chen X, Wang S, et al. Underwater image restoration through a prior guided hybrid sense approach and extensive benchmark analysis. IEEE Trans Circuits Syst Video Technol. 2025;35(5):4784–800.

380. Liang J, Cao J, Sun G, et al. SwinIR: Image restoration using Swin Transformer. IEEE/CVF International Conference on Computer Vision Workshops (ICCVW) 1833–1844 (2021).
381. Zamir S W, Arora A, Khan S, et al. Restormer: Efficient transformer for high-resolution image restoration. IEEE/CVF Conference on Computer Vision and Pattern Recognition (CVPR) (2022).
382. Wang Z, Cun X, Bao J, et al. Uformer: A general ushaped transformer for image restoration. Proceedings of the IEEE/CVF Conference on Computer Vision and Pattern Recognition 17683–17693 (2022).
383. Dou M, Qiu S, Hu M, et al. McAmamba: multi-level cross-modal attention-guided state space model for multi-source remote sensing image classification. IEEE Trans Geosci Remote Sens. 2025;63:1–19.
384. Potlapalli V, Zamir S W, Khan S, et al. PromptIR: Prompting for all-in-one blind image restoration. Proceedings of the 37th International Conference on Neural Information Processing Systems (NeurIPS 2023) (2023).
385. Wu G, Jiang J, Jiang K, et al. Harmony in diversity: Improving all-in-one image restoration via multi-task collaboration. Proceedings of the 32nd ACM International Conference on Multimedia (MM 2024) 6015–6023 (2024).
386. Wu G, Jiang J, Jiang K, et al. Learning dynamic prompts for all-in-one image restoration. IEEE Trans Image Process. 2025;34:1–1.
387. Pizer SM, Amburn EP, Austin JD, et al. Adaptive histogram equalization and its variations. Computer vision, Graphics, and Image Processing. 1987;39(3):355–68.
388. Zuiderveld KJ. Contrast limited adaptive histogram equalization. Graphics Gems. 1994;4(1):474–85.
389. Abdullah-Al-Wadud M, Kabir MH, Dewan MAA, et al. A dynamic histogram equalization for image contrast enhancement. IEEE Trans Consum Electron. 2007;53(2):593–600.
390. Foster DH. Color constancy. Vis Res. 2011;51(7):674–700.
391. Hitam M S, Awalludin E A, Yussof W N J H W, et al. Mixture contrast limited adaptive histogram equalization for underwater image enhancement. International Conference on Computer Applications Technology (ICCAT) 1–5 (2013).
392. Zhang S, Wang T, Dong J, et al. Underwater image enhancement via extended multi-scale retinex. Neurocomputing. 2017;245:1–9.
393. Land EH, McCann JJ. Lightness and Retinex theory. J Opt Soc Am. 1971;61(1):1–11.
394. McGlamery B. A computer model for underwater camera systems. Ocean Optics VI. 1980;208:221–31.
395. Trucco E, Olmos-Antillon AT. Self-tuning underwater image restoration. IEEE J Ocean Eng. 2006;31(2):511–9.
396. He K, Sun J, Tang X. Single image haze removal using dark channel prior. IEEE Trans Pattern Anal Mach Intell. 2010;33(12):2341–53.
397. Drews PL, Nascimento ER, Botelho SS, et al. Underwater depth estimation and image restoration based on single images. IEEE Comput Graph Appl. 2016;36(2):24–35.
398. Galdran A, Pardo D, Picón A, et al. Automatic red-channel underwater image restoration. J Vis Commun Image Represent. 2015;26:132–45.
399. Akkaynak D, Treibitz T. A revised underwater image formation model. Proceedings of the IEEE Conference on Computer Vision and Pattern Recognition, 6723–6732 (2018).
400. Li C, Anwar S, Porikli F. Underwater scene prior inspired deep underwater image and video enhancement. Pattern Recognit. 2020;98:107038.
401. Li C, Guo C, Ren W, et al. An underwater image enhancement benchmark dataset and beyond. IEEE Trans Image Process. 2019;29:4376–89.
402. Li C, Anwar S, Hou J, et al. Underwater image enhancement via medium transmission-guided multi-color space embedding. IEEE Trans Image Process. 2021;30:4985–5000.
403. Wang Y, Guo J, Gao H, et al. UIEC^2-net: CNN-based underwater image enhancement using two color space. Signal Process Image Commun. 2021;96:116250.
404. Fu Z, Wang W, Huang Y, et al. Uncertainty inspired underwater image enhancement. European Conference on Computer Vision, 465–482 (2022).
405. Guo Y, Li H, Zhuang P. Underwater image enhancement using a multiscale dense generative adversarial network. IEEE J Ocean Eng. 2020;45(3):862–70.
406. Hambarde P, Murala S, Dhall A. UW-GAN: single-image depth estimation and image enhancement for underwater images. IEEE Trans Instrum Meas. 2021;70:1–12.
407. Liu Q, Zhang Q, Liu W, et al. WSDS-GAN: a weakstrong dual supervised learning method for underwater image enhancement. Pattern Recogn. 2023;143:109774.
408. Vaswani A, Shazeer N, Parmar N, et al. Attention is all you need.Advances in Neural Information Processing Systems 30 (NIPS 2017), Long Beach, CA, USA 6000–6010 (2017).
409. Liu Z, Lin Y, Cao Y, et al. Swin transformer: Hierarchical vision transformer using shifted windows. Proceedings of the IEEE/CVF International Conference on Computer Vision 10012–10022 (2021).
410. Zamir S W, Arora A, Khan S, et al. Restormer: Efficient transformer for high-resolution image restoration. Proceedings of the IEEE/CVF Conference on Computer Vision and Pattern Recognition 5728–5739 (2022).
411. Peng L, Zhu C, Bian L. U-shape transformer for underwater image enhancement. IEEE Trans Image Process. 2023;32:3066–79.
412. Liu H, Wang F, Jin Y, et al. Learning-based real-time imaging through dynamic scattering media. Light Sci Appl. 2024;13:194.
413. Hickman GD, Hogg JE. Application of an airborne pulsed laser for near shore bathymetric measurements. Remote Sens Environ. 1969;1(1):47–58.
414. Hoge F, Swift RN, Frederick EB. Water depth measurement using an airborne pulsed neon laser system. Appl Opt. 1980;19(6):871–83.
415. Banic J, Sizgoric S, O'Neil R. Scanning lidar bathymeter for water depth measurement. Laser Radar Technology and Applications I. 1986;663:187–95.
416. Penny MF, Abbot RH, Phillips D, et al. Airborne laser hydrography in Australia. Appl Opt. 1986;25(13):2046–58.
417. Steinvall O, Klevebrant H, Lexander J, et al. Laser depth sounding in the Baltic Sea. Appl Opt. 1981;20(19):3284–6.

418. Irish JL, Lillycrop WJ. Scanning laser mapping of the coastal zone: the shoals system. ISPRS J Photogramm Remote Sens. 1999;54(2–3):123–9.
419. Steinvall OK, Koppari KR, Karlsson UC. Airborne laser depth sounding: system aspects and performance. Proc SPIE. 1994;2258:392–412.
420. Penny M, Billard B, Abbot R. Lads—the australian laser airborne depth sounder. Int J Remote Sens. 1989;10(9):1463–79.
421. Tuell G, Barbor K, Wozencraft J. Overview of the coastal zone mapping and imaging lidar (CZMIL): a new multisensor airborne mapping system for the US army corps of engineers. Algorithms and Technologies for Multispectral, Hyperspectral, and Ultraspectral Imagery XVI. 2010;7695:226–33.
422. Mazih H, Carme J L, Pronier L, et al. A high resolution, accurate, seamless coastal model of 950+ linear km of the northern coastal of France. FIG Working Week 2024: Your World, Our World — Resilient Environment and Sustainable Resource Management for All, Accra, Ghana. Paper TS03B(12631), 15 (2024).
423. Mandlburger G, Pfennigbauer M, Schwarz R, et al. Concept and performance evaluation of a novel UAV-borne topo-bathymetric lidar sensor. Remote Sens. 2020;12(6):986.
424. Zhu X, Yang K, Li Z. The experiment of airborne laser bathymeter. Chin J Lasers. 1998;25(5):470.
425. Yan H, Dong W. Performance evaluation of airborne ocean lidar for measuring chlorophyll-a, suspended matter and coastal water depth in the east China sea. Period Ocean Univ China. 2004;34(4):649–54.
426. He Y, Hu S, Chen W, et al. Research progress of domestic airborne dual-frequency lidar detection technology. Laser Optoelectron Prog. 2018;55(8):082801.
427. Ouyang YZ, Huang MT, Zhai GJ, et al. On the depth reduction in airborne laser hydrography. Hydrographic Surveying and Charting. 2003;23(1):1–5.
428. Ye XS, Huang MT, Ren LP, et al. Computations of footprints for airborne laser bathymetry. Engineering of Surveying and Mapping. 2010;19(3):31–4.
429. Xu W, Guo K, Liu Y, et al. Refraction error correction of airborne lidar bathymetry data considering sea surface waves. Int J Appl Earth Obs Geoinf. 2021;102:102402.
430. Huang T, Tao B, He Y. Classification of sea and land waveform based on multichannel ocean lidar. Chin J Lasers. 2017;44(6):0610002.
431. Li Y, Qiu Z, He L, et al. Combined bathymetric method of multi-channel waveform datafor dual-frequency lidar. Marine Surveying and Mapping. 2020;40(2):47–51.
432. Guo K, Li Q, Wang C, et al. Development of a single-wavelength airborne bathymetric lidar: system design and data processing. ISPRS J Photogramm Remote Sens. 2022;185:62–84.
433. Yu J, Lu X, Tian M, et al. Effect analysis of positioning model and boresight error analysis of airborne lidar bathymetry system. Infrared and Laser Engineering. 2019;48(6):606005–0606005.
434. Zhou G, Hu H, Xu J, et al. Design of lidar optical machine system for airborne single frequency bathymetry. Infrared and Laser Engineering. 2021;50(4):20200297.
435. Hu S, He Y, Chen W, et al. Design of airborne dualfrequency laser radar system. Infrared and Laser Engineering. 2018;47(9):930001–0930001.
436. Wang D, Xing S, He Y, et al. Evaluation of a new lightweight UAV-borne topo-bathymetric lidar for shallow water bathymetry and object detection. Sensors. 2022;22(4):1379.
437. Li X, Sun Z, Wu G. Optical guidance for AUV underwater docking. Acta Optica Sinica. 2025;45(12):01.
438. Sun Z, Li X. Water-related optical imaging: from algorithm to hardware. Sci China Technol Sci. 2025;68(1):1100401.
439. Zhu R, Li C, Yang M, et al. Multi-branch network optical guidance and positioning method for autonomous underwater vehicles. SCIENTIA SINICA Informationis. 2025;55(1):110–28.

Publisher's Note